

**Growth of epitaxial graphene on SiC (0001) by  
thermal decomposition in argon and its etching  
in oxygen atmosphere**

**Wang Chenxing**

## CONTENTS

<b>Chapter 1</b>	Introduction	1
1.1	Basics of graphene	1
1.1.1	Physical properties of graphene	1
1.1.2	Graphene nanoribbon	3
1.2	Fabrication methods of graphene	6
1.2.1	Graphite exfoliation	6
1.2.2	CVD	7
1.2.3	Thermal decomposition of SiC	8
1.3	Graphene growth on SiC substrates	9
1.4	Objective of this study	19
<b>Chapter 2</b>	Experimental Methods	21
2.1	Preparation of samples	21
2.1.1	SiC substrates	21
2.1.2	Laser lithography and reactive ion etching	22
2.1.3	Annealing	24
2.2	Characterizations	25
2.2.1	Scanning electron microscopy	25
2.2.2	Scanning tunneling microscopy	27
2.2.3	Reflection high-energy electron diffraction	30
2.2.4	Atomic force microscopy	32
2.2.5	Raman spectroscopy	33
2.3	Setup of <i>in situ</i> UHV-SEM/STM system	35
<b>Chapter 3</b>	Graphene Growth on SiC (0001) Under Argon Atmosphere	38
3.1	Introduction	38
3.2	Experimental and results	39
3.2.1	Graphene growth on step-free SiC surfaces	39
3.2.2	Graphene growth at various pressures and temperatures	42
3.2.3	Graphene growth on wide terraces	48
3.2.4	Observation of graphene growth processes on wide terraces	53

3.3	Discussions .....	57
3.3.1	Graphene growth on step-free SiC surfaces .....	57
3.3.2	Dependence of graphene formation on gas pressure and annealing temperature .....	59
3.3.3	Graphene growth on wide terraces .....	60
3.3.4	Graphene growth mechanisms from step bunches .....	63
3.3.5	Starfish-like graphene nucleation on terraces .....	67
3.4	Summary .....	68
<b>Chapter 4</b>	<b>Etching of Epitaxial Graphene with Oxygen .....</b>	<b>70</b>
4.1	Introduction .....	70
4.2	Experimental and results .....	73
4.2.1	Sample preparation and characterizations .....	73
4.2.2	Results of selective oxygen etching .....	74
4.2.3	Etching processes of surface buffer layer .....	80
4.3	Discussions .....	83
4.3.1	Etching of surface buffer layer under oxygen-argon mixture .....	83
4.3.2	Mechanisms of surface buffer layer etching .....	84
4.4	Summary .....	87
<b>Chapter 5</b>	<b>Formation and Oxygen Etching of Graphene Nanoribbon .....</b>	<b>88</b>
5.1	Introduction .....	88
5.2	Experimental and results .....	90
5.3	Discussions .....	94
5.3.1	Formation processes of graphene nanoribbons .....	94
5.3.2	Etching of surface buffer layer .....	96
5.4	Summary .....	96
<b>Chapter 6</b>	<b>Conclusion and Perspective .....</b>	<b>98</b>
6.1	Conclusion .....	98
6.2	Perspective .....	99

# Chapter 1 Introduction

## 1.1 Basics of graphene

In the past of several decades, carbon nanomaterials have attracted an astonishing interest among millions of scientists, due to their diverse structures and unique properties. Fullerene, a spherical molecule of carbon atoms, and carbon nanotube, a cylindrical structure of carbon atoms, being zero-dimensional and one-dimensional nanostructure respectively, brought about a great many of specific physical properties. After the discovery of fullerenes and nanotubes, graphene, being well known as the most ideal two-dimensional material, joined the family of carbon nanomaterial.

### 1.1.1 Physical properties of graphene

Graphene is a one-atom-thick sheet (thickness of  $0.37 \text{ \AA}$  [1]) of carbon atoms in a honeycomb lattice (Figure 1.1(a) [2]), with a lattice constant of  $2.4589 \text{ \AA}$  [2]. Carbon atoms in graphene are bonded trigonally by  $sp^2$  hybridized  $\sigma$  bonds and  $\pi$  bond. The  $\pi$  band has a linear electronic band dispersion (known as the Dirac cone (Figure 1.1(b) [3])) near the Fermi level. Electrons at the Dirac cone behave as massless fermions that cause the extremely high carrier mobility ( $2 \times 10^5 \text{ cm}^2/\text{Vs}$  at room temperature [4]). Beside the extraordinary electrical property, graphene shows a high thermal conductivity ( $5000 \text{ W/mK}$  [5]), an extreme large specific surface area ( $2630 \text{ m}^2/\text{g}$  [6]), high Young's modulus ( $1100 \text{ GPa}$ ) and breaking strength ( $125 \text{ GPa}$  [7]), and high visual transparency ( $97.7\%$  for single layer [8]). All these unique properties (as summarized in Table 1.1) provided an impetus for the researches of graphene, and Nobel Prize in Physics in 2010 was given to A. Geim and K. Novoselov who first isolated and characterized one layer of graphene experimentally [9].

Table 1.1: Unique properties of graphene.

Thickness	0.37 Å [1]
Mobility	$2 \times 10^5$ cm <sup>2</sup> /Vs [4]
Thermal conductivity	5000 W/mK [5]
Specific surface area	2630 m <sup>2</sup> /g [6]
Young's modulus	1100 GPa [7]
Strength	125 GPa [7]
Visual transparency	97.7% [8]

Due to the variety of excellent properties, graphene has been shown to exhibit the potential application in next-generation electronic devices. For instance, field-effect transistors fabricated on graphene by Lin et al. has attained a cutoff frequency of 100 GHz [10]. Graphene is also an ideal alternate of copper (Cu) wiring as on-chip interconnects, which will dramatically improve device performance [11]. Graphene sensors of biomolecule also show excellent performance and likely to be applied on medical devices [12]. Moreover, in energy field, due to the high transparency, graphene is an ideal electrode for solar cells [13]. It is also reported that lithium batteries were improved after using graphene as their anodes [14].

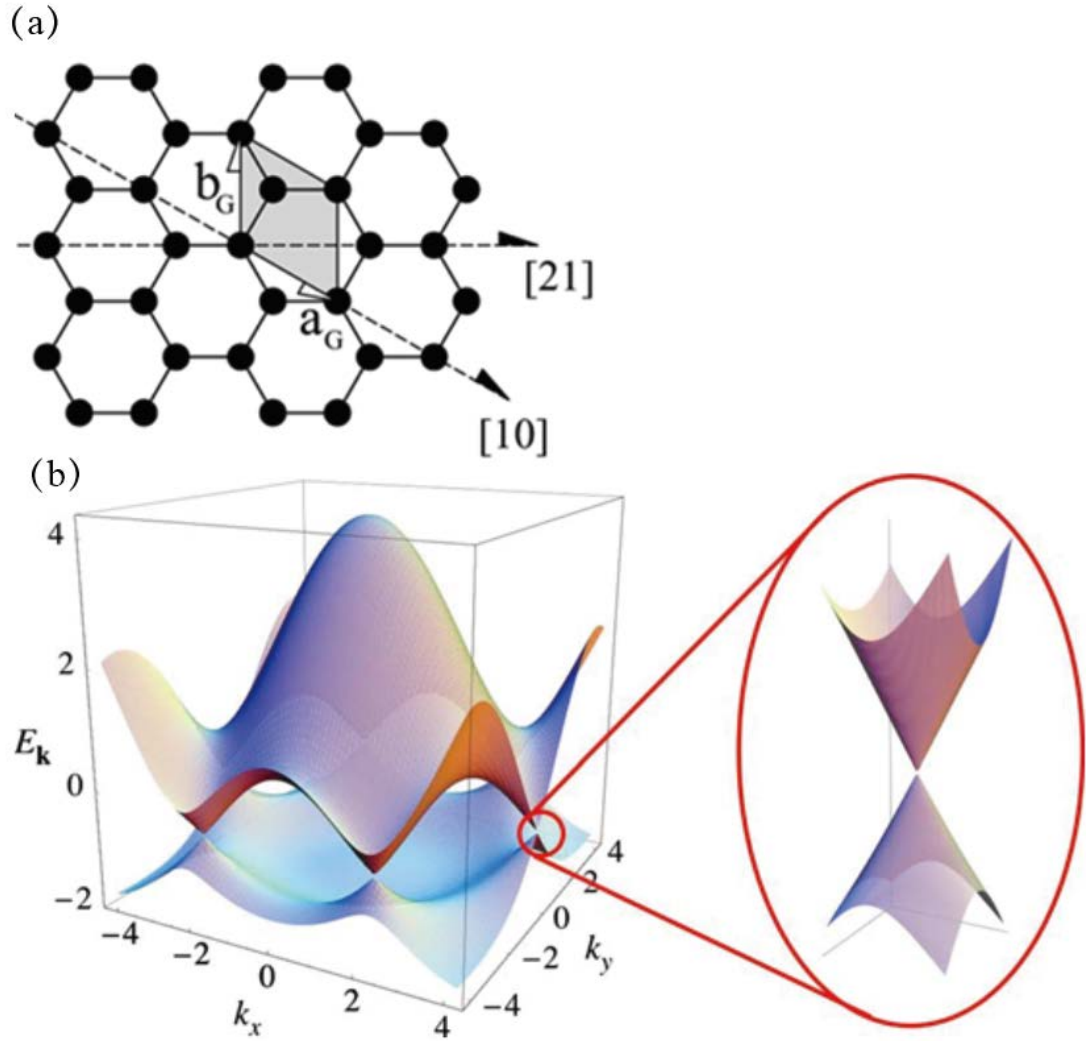


Figure 1.1: (a) Graphene hexagonal structure comprised of  $sp^2$ -carbon. The unit cell (shaded) containing two carbon atoms is shown along with standard unit cell vectors  $\mathbf{a}_G$  and  $\mathbf{b}_G$  [2]. (b) Electronic dispersion in graphene and zoom in of the energy bands close to one of the Dirac points [3].

## 1.1.2 Graphene nanoribbon

When the width of two-dimensional graphene reduces to nanoscale, one-dimensional graphene nanoribbon forms and brings about a remarkable change of the electrical property. A band gap is opened for graphene nanoribbons, which greatly promote the applications of graphene for semiconductor devices [15, 16]. Two different type of ideal graphene nanoribbons is determined by their edge orientations,

i.e. armchair and zigzag graphene nanoribbons. A theoretical calculation by Nakada et al. shows the variation of band structure with the edge types and width of the ribbons, as shown in Figure 1.2 [15]. The calculation shows all the zigzag ribbons are metallic with the metallic states at  $E=0$ . While, band gaps are opened in some of armchair ribbons. Armchair ribbon is semiconducting when the width (carbon atom count  $N$  across the ribbon)  $N=3M$  or  $N=3M-2$ , where  $M$  is an integer. In addition, for the case of zigzag graphene nanoribbons, flat band and high density of states (DOS) with spin-state splitting is represented at the ribbon edges, which also brings about applications for spintronic devices [17, 18]. As shown in Figure 1.3, spin states at the Fermi level can be modified by applying an electric field in the plane of the ribbon.

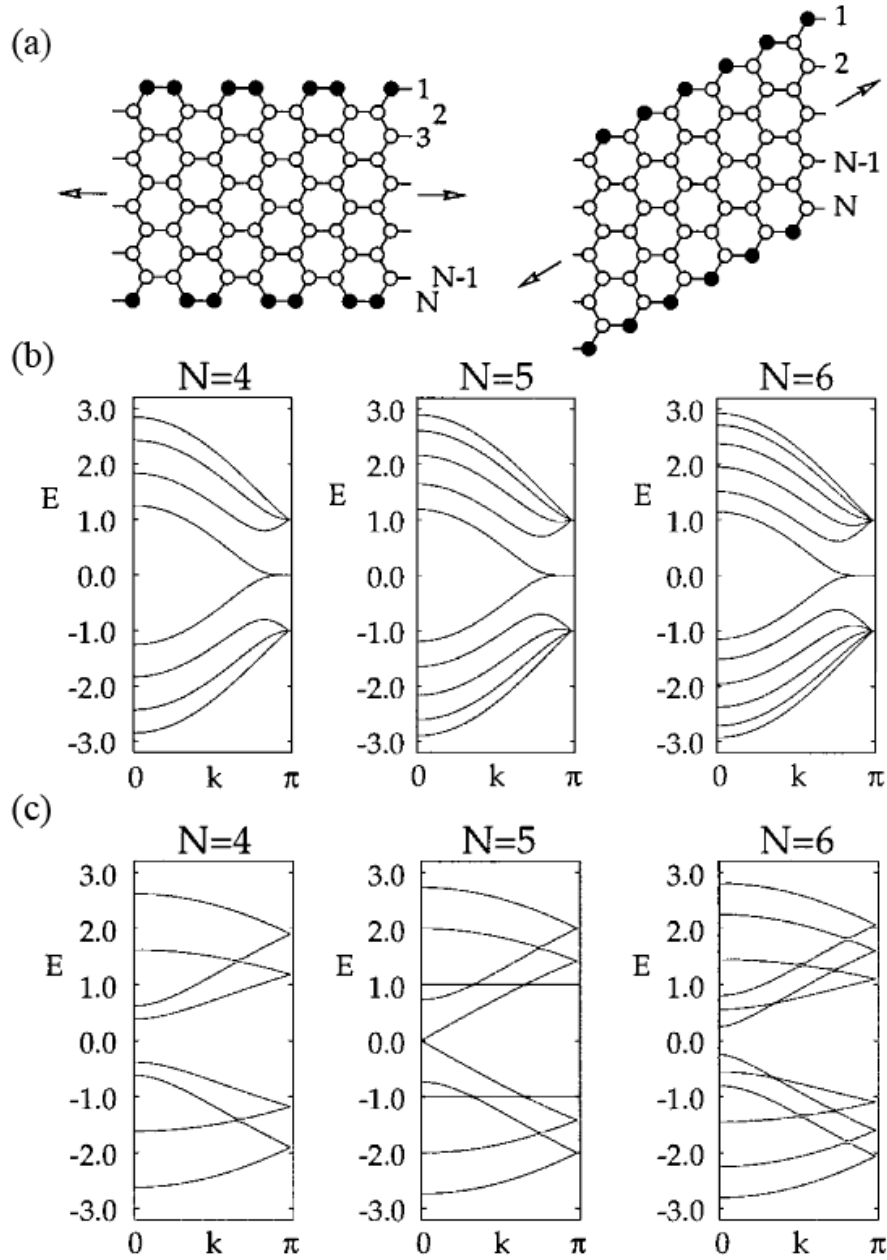


Figure 1.2: (a) Structures of graphene nanoribbons: armchair (left) and zigzag (right). The structure of edge atoms (black spot) is determined by the orientations (arrows) of graphene lattice. (b) and (c) Calculation of electron band structure for (b) zigzag and (c) armchair ribbons with various widths. The widths of ribbon  $N$  are indicated by the count of carbon atoms across the ribbon, as shown in (a) [15].



graphene size and layer number.

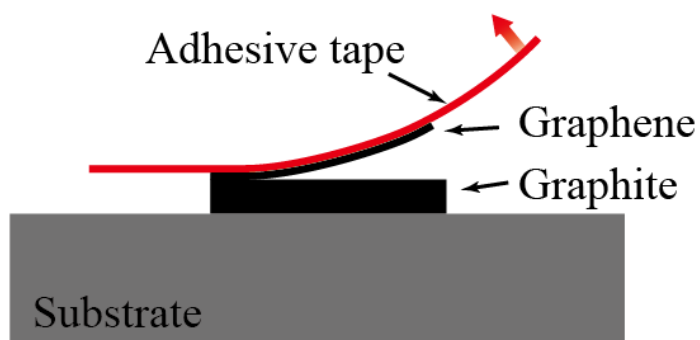


Figure 1.4: Schematic diagram of exfoliation of graphene layers from graphite by an adhesive tape.

## 1.2.2 CVD

CVD is a technology to fabricate film material by depositing a material on the surface of a heated solid substrate, which is also reported to be an efficient method to obtain graphene layers. In CVD processes, carbon atoms from carbon resource gases (normally hydrocarbons such as ethylene and methane) can be deposited on a heated catalyst metal substrate to form graphene layers (Figure 1.5). Several metals such as nickel and copper have been frequently used as substrates during CVD [19]. Then a transfer of graphene layers to an insulating substrate is necessary for its applications. The layer number and domain size of graphene can be easily controlled by altering the CVD conditions, and due to that, CVD has been widely studied to efficiently fabricate graphene [20, 21]. Such method has a potential of graphene applications on display touch panel [22], and solar cells [23] as conducting transparent electrodes. However, for the applications on precise semiconductor devices, the transfer process will introduce significant defects, stress and contamination in graphene layer, which degrades the crystallinity of graphene and thus lower the device performance.

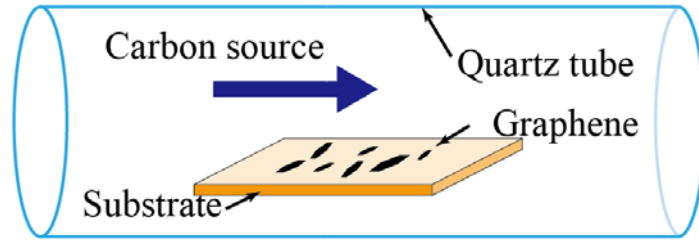


Figure 1.5: Schematic diagram of graphene formation in a quartz tube of CVD system.

### 1.2.3 Thermal decomposition of SiC

Thermal decomposition of SiC is an approach to epitaxially grow high quality graphene layers directly on the insulating SiC substrates. Figure 1.6 shows growth processes of graphene on SiC. Silicon atoms sublime when annealing SiC to a high temperature (above 1100°C), and remained carbon atoms diffuse and nucleate to form epitaxial graphene. As early as 1975, Bommel et al. [24] reported the graphitization on SiC surface after heat-treatment by observations of low-energy electron diffraction (LEED) and Auger electron spectroscopy (AES). Nowadays, epitaxial graphene formed on SiC substrates has been made with an extremely high crystallinity and remarkable transport properties, which can even rival with the exfoliated graphene. Hence, thermal decomposition of SiC proposed the most applicability to graphene electronics, which excites our interest on this method.

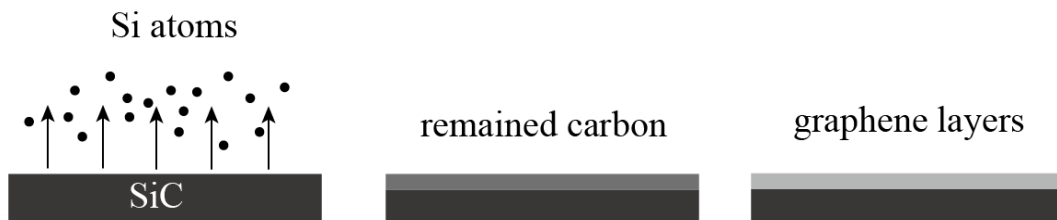


Figure 1.6: Schematic diagram of graphene growth processes by thermal decomposition of SiC.

### 1.3 Graphene growth on SiC substrates

SiC crystal is a compound of silicon and carbon, known as its high hardness which is even comparable to diamonds. There are also many unique electric properties, such as wide bandgap, high thermal conductivity and large critical electric field, as listed in Table 1.2, which let SiC be used as power electronics and devices for astronomy etc.

Table 1.2: Properties of 4H-SiC, 6H-SiC, Si, GaN and diamond.

Properties	4H-SiC	6H-SiC	Si	GaN	Diamond
Energy bandgap (eV)	3.26	2.93	1.1	3.4	5.5
Mobility (cm <sup>2</sup> /Vs)	950	400	1500	1200	1800
Thermal conductivity (W/mK)	490	490	130	150	2090
Dielectric constant	9.7	9.7	11.9	10.4	5.9
Critical electric field (MV/cm)	3.5	3.0	0.3	3.3	4

SiC has three major structures, i.e. 3C-SiC, 4H-SiC and 6H-SiC. The epitaxial graphene formation mainly takes place on the surface of 4H and 6H-SiC. As shown in Figure 1.7, the structures 4H and 6H-SiC are composed of 4 and 6 SiC bilayers in each unit cell with different stacking sequences. The structure parameters are shown in Table 1.3. In one SiC bilayer, Si and C atoms are both hexagonally structured but lying in different levels. Such that two kinds of terminal face, SiC (0001) Si-face and SiC (000 $\bar{1}$ ) C-face, exist in a single crystal of 4H and 6H-SiC, and epitaxial graphene are able to grow on the both faces by decomposition of SiC.

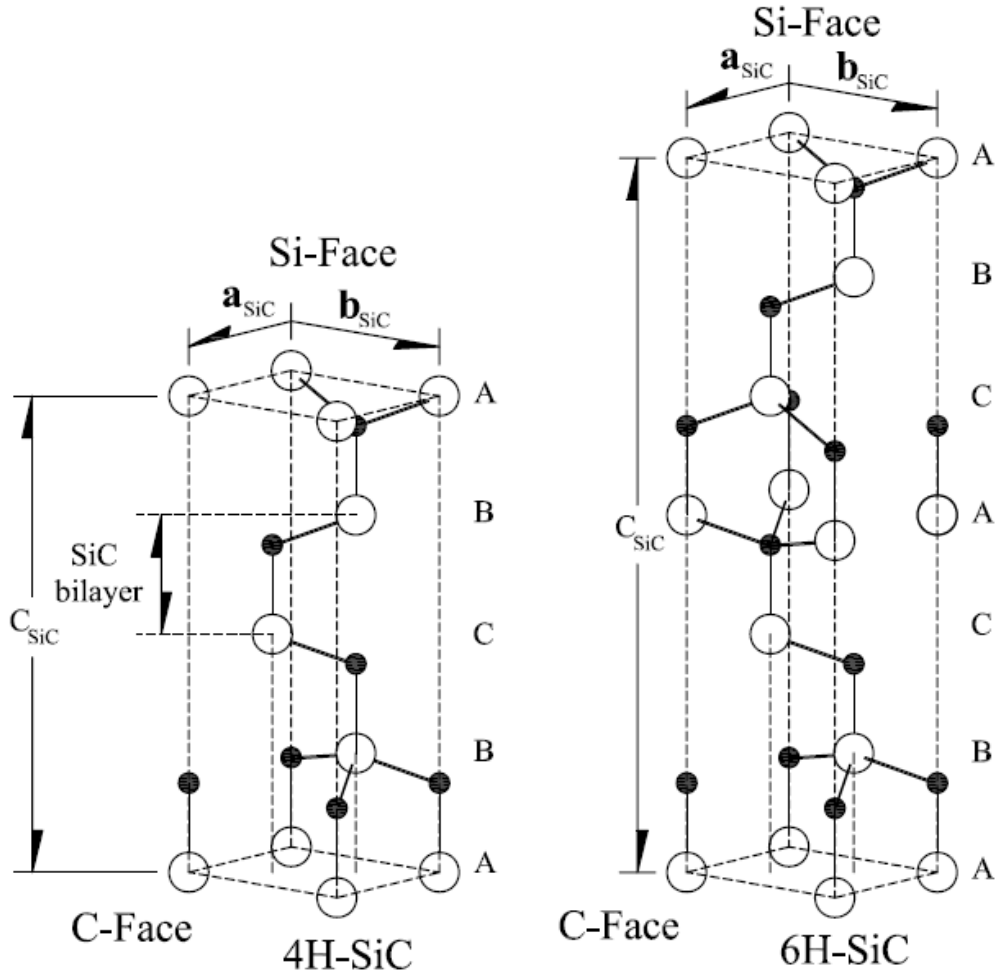


Figure 1.7: Unit cell structure of 4H (left) and 6H-SiC (right), where filled circles are carbon atoms and open circles are silicon atoms [2].

Table 1.3 Structural parameters of 4H and 6H-SiC [2].

SiC polytype	4H-SiC	6H-SiC
$a_{\text{SiC}} (\text{\AA})$	3.0805	3.0813
$c_{\text{SiC}} (\text{\AA})$	10.0848	15.1198

The most remarkable fact is that the graphene formation on the two faces (Si-face and C-face) are totally different, as shown in Figure 1.8 [25]. For the case of the Si-face, the decomposition rate is lower and fewer layer graphene (<10 layers) is usually formed than the C-face. On the other hand, multilayer graphene (>10 layers) is easily formed on the C-face due to a higher decomposition rate of SiC. Graphene

formation on the both sides of SiC were intuitively observed in high-resolution transmission electron microscopy (TEM) images as reported by Norimatsu et al. [25, 26, 27]. In Figure 1.9, a series of section TEM images of SiC (0001) surface after heating at various temperatures shows few layer graphene (the dark line shown by arrows) formed on the substrates with arising flat surfaces in the scale of tens nanometer. They also carried out the growth control of graphene on SiC (000 $\bar{1}$ ) by suppressing the decomposition of SiC under an argon (Ar) pressure. As shown by the TEM and atomic force microscope (AFM) images in Figure 1.10, although only 5 layers of graphene are formed, surface became very rough due to the high decomposition rate of the C-face.

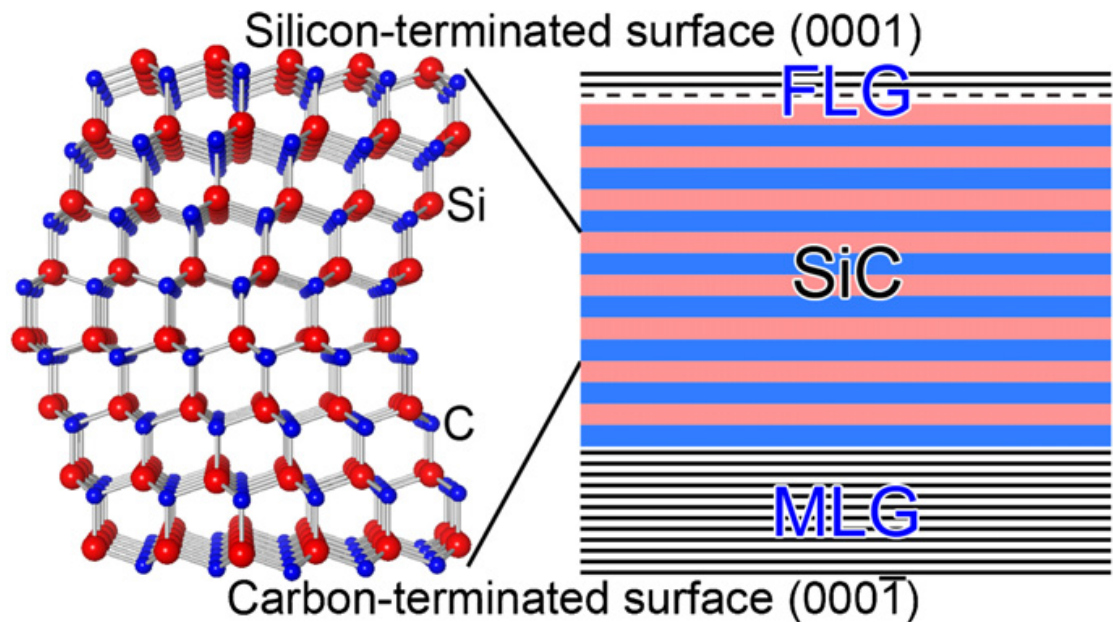


Figure 1.8: Schematic diagram of the dependence between SiC structure (left side) and graphene formations (right side) on Si-face and C-face [25].

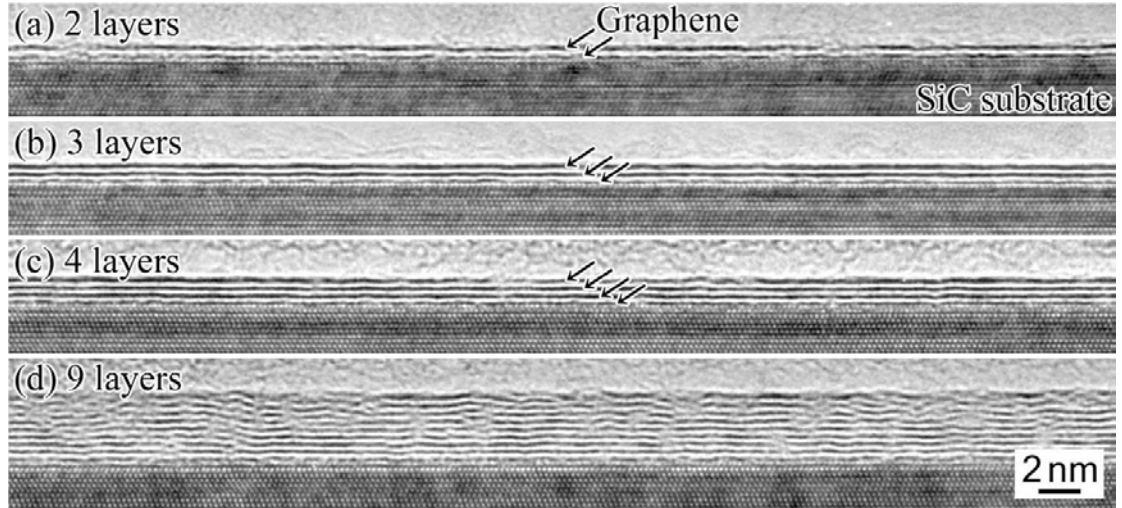


Figure 1.9: Section TEM images of graphene/SiC (0001) surface after annealing at (a) 1350°C for 0.5 h, (b) 1450°C for 0.5 h, (c) 1400°C for 1 h, (d) 1500°C for 0.5 h in high vacuum [26].

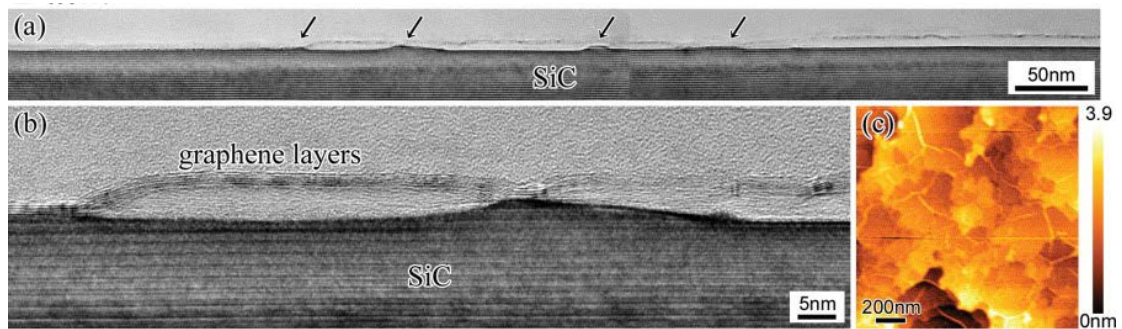


Figure 1.10: (a) (b) Section TEM images and (c) AFM image of graphene/SiC (000 $\bar{1}$ ) after annealing at 1500°C in 1-atm-Ar atmosphere [27].

The stacking of graphene layers is also different between the two faces, as shown the low-energy electron diffraction (LEED) in Figure 1.11 [28]. Comparing with the schematic diagram of reciprocal space for graphene on SiC in Figure 1.11(a), the LEED pattern from graphene/SiC (0001) surface in Figure 1.11(b) represents clear graphene ( $1 \times 1$ ) and SiC ( $1 \times 1$ ) spots, which are rotated  $30^\circ$  each other. Besides, spots of a SiC ( $6\sqrt{3} \times 6\sqrt{3}$ )R $30^\circ$  reconstruction are also arisen. For the case of the LEED pattern from graphene/SiC (000 $\bar{1}$ ) surface (Figure 1.11(c)), weaker graphene spots are aligned on a ring, indicating a random rotation between graphene layers on

the C-face of SiC. In Figure 1.12, a study of angle-resolved photoemission spectroscopy (ARPES) by Ohta et al. [29] shows that band structure of graphene with 1-4 layers on SiC (0001) indicate the ABAB stacking of the graphene layers on Si-face.

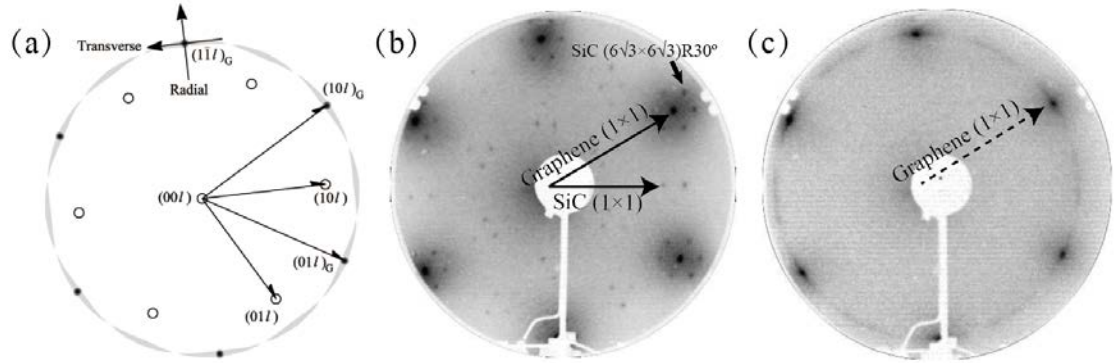


Figure 1.11: (a) Schematic diagram of reciprocal space for graphene on SiC. Black spots and circles indicate graphene and SiC rods respectively. (b) LEED image of 2 graphene layers on SiC (0001). (c) LEED image of 7 graphene layers on SiC (000 $\bar{1}$ ) [28].

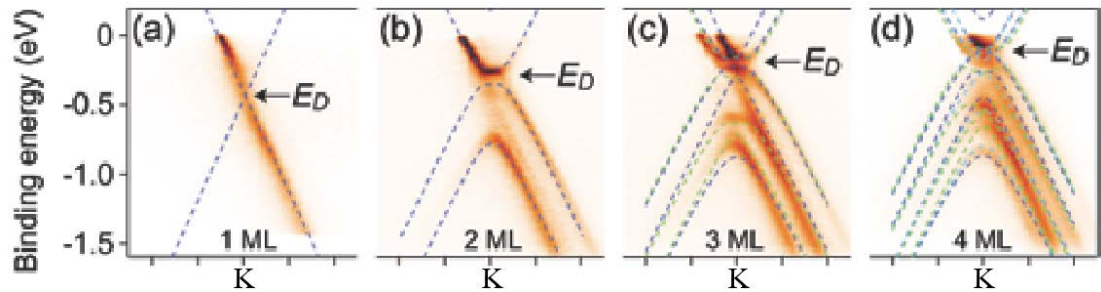


Figure 1.12: ARPES images of  $\pi$  band near the Dirac point from (a-b) 1-4 layers of graphene on SiC (0001). The band structures are fitting well to the tight binding calculations (dashed line) [29].

TEM image in Figure 1.13 [25] also revealed an interlayer between SiC (0001) Si-face and graphene layers, and the presence of so called buffer layer result in the difference from that on the C-face. As illustrated in Figure 1.14, the first formed carbon layer on the Si-face is accurately not a monolayer graphene but a surface buffer layer. The buffer layer has the same structure with graphene, but the C atoms in

the buffer layer are partly bond with Si atoms of the underneath SiC substrate by covalent bonds, which extinguish the graphene properties for the case of buffer layer. By further decomposition of SiC, a new buffer layer grows underneath the previous one, and then the surface buffer layer transforms to a monolayer of graphene. Thus, the bond between the buffer layer and SiC substrate slow down the graphene forming speed on the Si-fcae. In addition, the SiC surface covered with a buffer layer always shows the moiré pattern of SiC  $(6\sqrt{3} \times 6\sqrt{3})R30^\circ$  super-structure, due to the lattice relationship of  $13a_g \approx 6\sqrt{3}a_{SiC}$ . Because of the presence of a buffer layer, the graphene on the Si-face always be exactly the coordinate rotated a degree of  $30^\circ$  to the SiC substrate [29, 30].

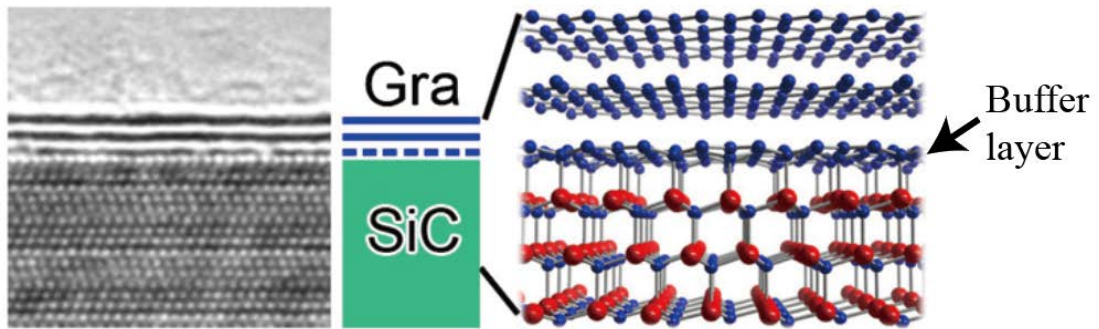


Figure 1.13: Section TEM image (left) and structure schematic diagram (right) of bilayer graphene and buffer layer on SiC (0001) [25].

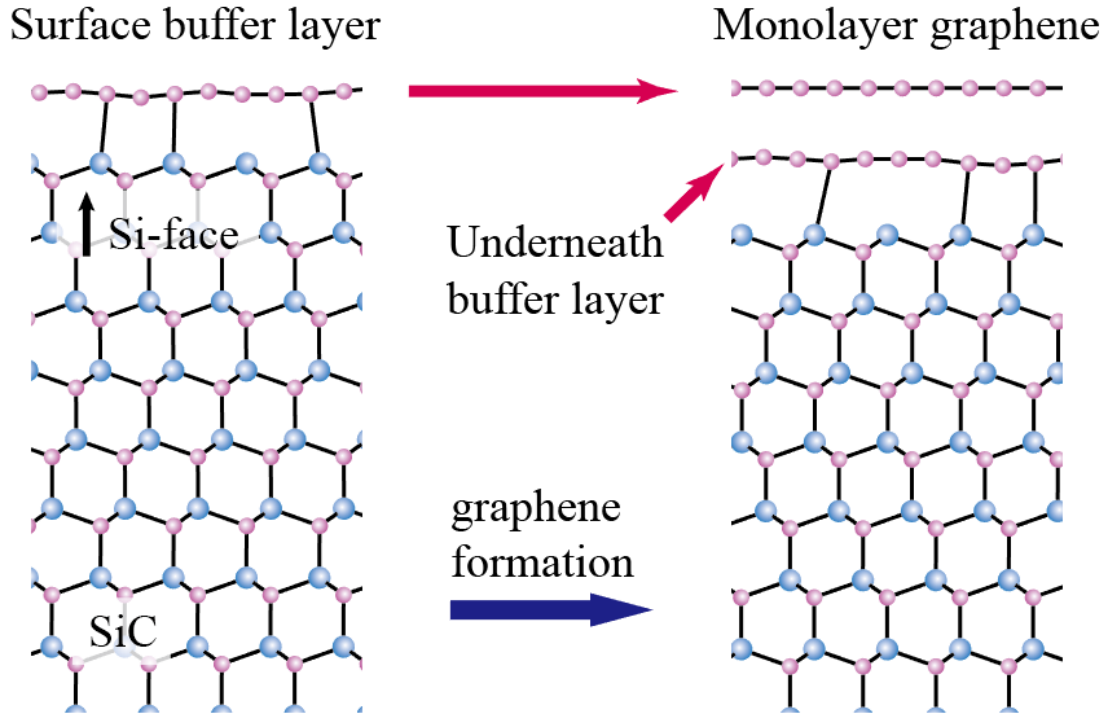


Figure 1.14: Schematic diagram the structure of buffer layer and the formation of the first layer of graphene on the Si-face.

The atomic structure of graphene on SiC is also studied by scanning tunneling microscopy (STM). Huang et al. [31] succeed in distinguishing the monolayer and bilayer graphene regions on SiC (0001) surface by atomic resolution STM images, as shown in Figure 1.15. Differing from the graphene ( $1 \times 1$ ) lattice seen on the monolayer area, it shows a  $(\sqrt{3} \times \sqrt{3})R30^\circ$  super-structure in the region of bilayer graphene. Such phenomenon can be explained by a changing of electron states due the interaction of graphene layers. Besides, layer number of graphene on SiC can also be measured by low-energy electron microscopy (LEEM) [32, 33]. As shown in Figure 1.16, Hibino et al. [32] reported that contrast changes in different graphene areas and electron energy, i.e. the reflectivity of electron energy oscillates as a function of the electron energy and graphene layer number. Some of other measurements has also been developed to investigate the layer number of graphene on SiC, such as X-ray diffraction (XRD) [34] and Raman spectroscopy [35].

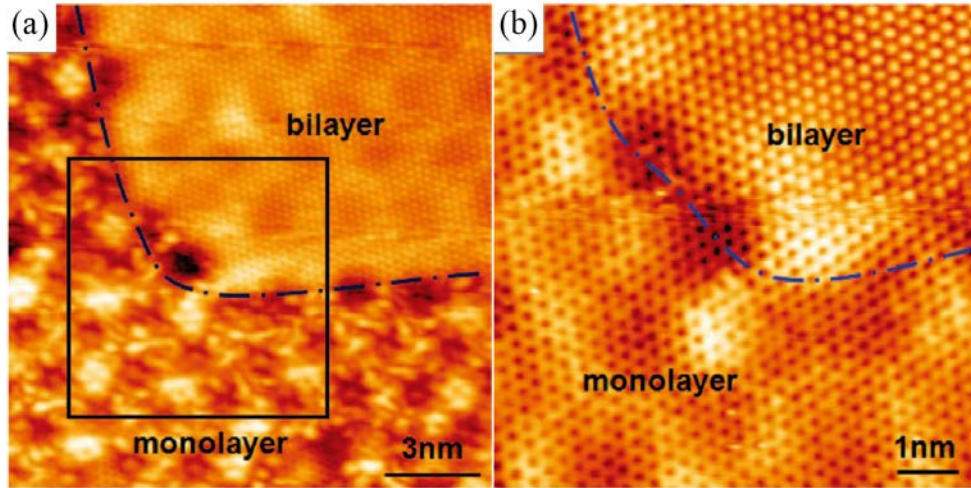


Figure 1.15: STM images of graphene on SiC (0001) in atomic resolution, showing monolayer and bilayer graphene areas ( $V_{\text{bias}}=0.5$  V for (a) and  $V_{\text{bias}}=-0.1$  V for (b)) [31]. (b) scanned in a black framed area in (a).

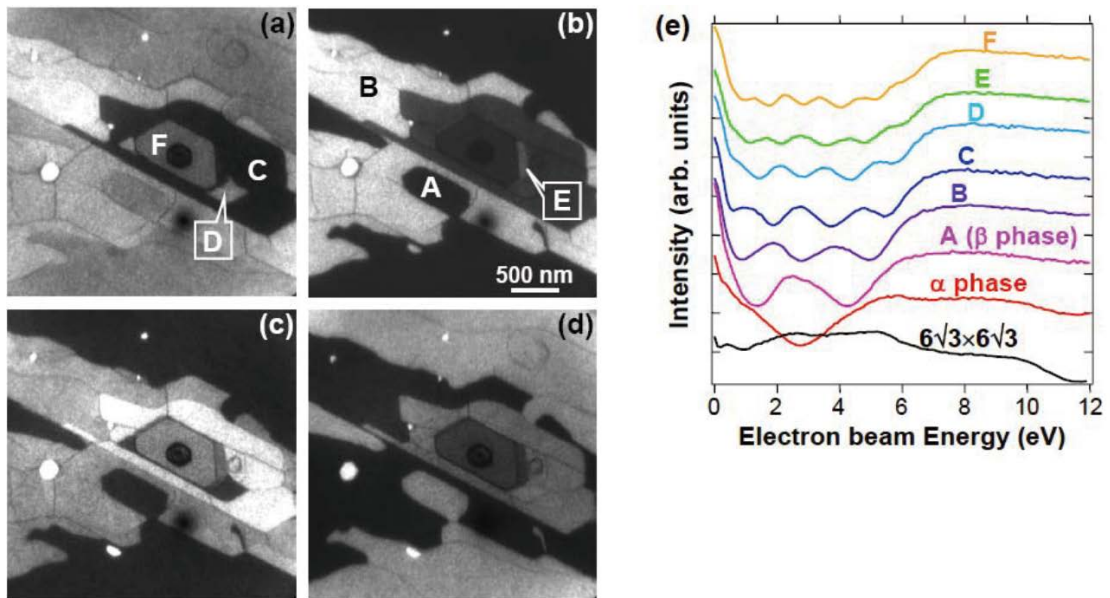


Figure 1.16: (a-d) LEEM images of graphene/SiC (0001) surface, obtained by the electron beam with energies of (a) 3.5 eV, (b) 4.0 eV (b) 4.5 eV and (d) 5.0 eV. (e) electron reflectivity spectra from the area A-E in the LEEM images of (a) and (b) [32].

Being different from the ordinary CVD growth processes, in which the carbon for graphene growth is supplied by an external carbon source, epitaxial growth of graphene on SiC proceeds by carbon left after the decomposition of SiC substrate

underneath. Although the SiC Si-face has lower decomposition rate and graphene forms more uniformly than that on the C-face, an early report has shown that graphene growth by heating SiC (0001) in ultra-high vacuum (UHV) causes rough substrate surfaces and non-uniform graphene growth in scale of micrometer, as shown in Figure 1.17 [36]. Recently, it was found that an annealing of SiC in an Ar atmosphere (Figure 1.18 [37]) and in Si vapor (Figure 1.19 [38]) leaves a flat surface after the graphene formation. Nevertheless, because of the extremely high process temperature (over 1100°C) and gas atmosphere (such as 1 atm Ar), it is quite difficult to investigate the graphene growth processes on SiC directly. Several divergent growth models have been demonstrated by different groups, as shown in Figure 1.20 [25, 39, 40], which are still confused us. Hence, there are still lots of issues, i.e. what are the processes of the graphene growth in a gas atmosphere and how the annealing conditions contribute to it, remained for growing epitaxial graphene on the SiC.

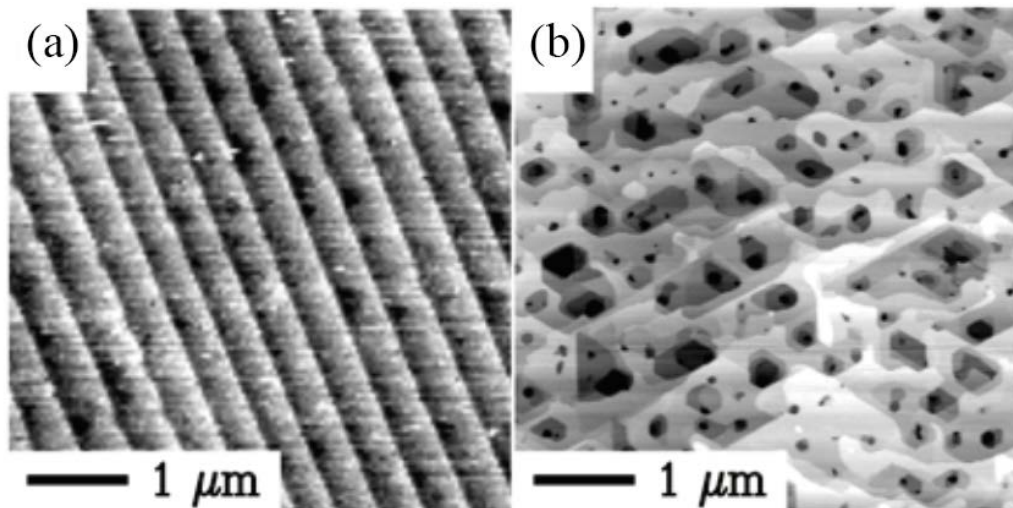


Figure 1.17: (a) AFM image of SiC (0001) before the graphitization with regular steps on the surface. (b) AFM image of surface after graphene formation in UHV. Hundreds of pits formed due to the decomposition, leaving a very rough surface [36].

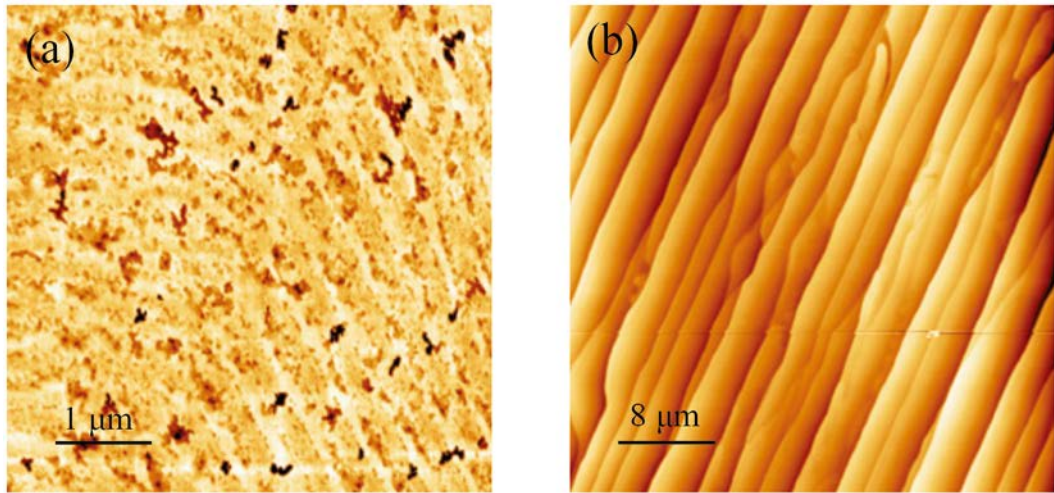


Figure 1.18: (a) AFM image of graphene formed surface after annealing SiC in UHV at 1280°C, in which a large amount of pits are formed. (b) AFM image of graphene surface on SiC by annealing in Ar (900 mbar) at 1650 °C, where terraces and steps are apparent on the surface [37].

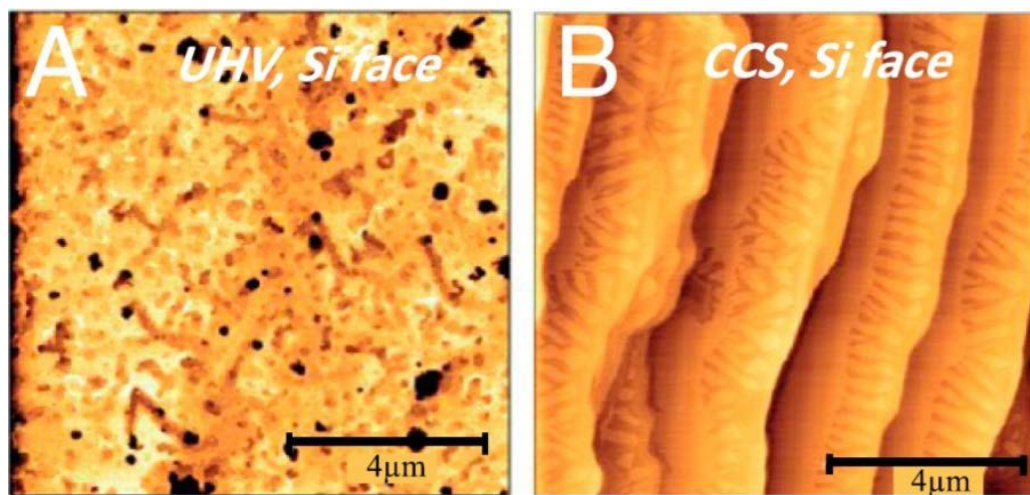


Figure 1.19: AFM images of graphene formed on SiC (0001) in (a) UHV and (b) Si vapor [38].

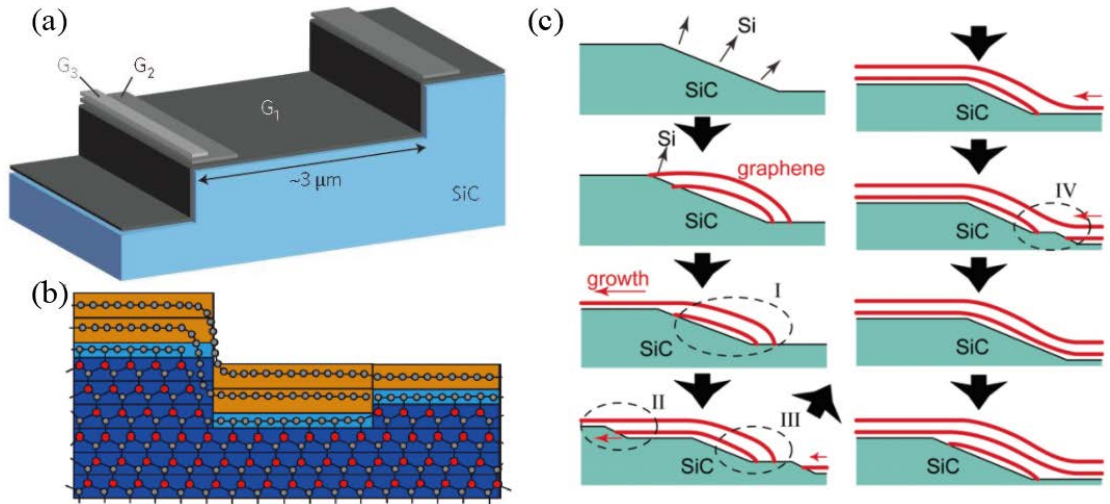


Figure 1.20: Models of graphene growth mechanism. (a) Growth on the top of step edges [39], (b) Growth at the lower side of a step edge [40], (c) Growth on the facet of step edges [25].

## 1.4 Objective of this study

As introduced above, it is obvious that the decomposition of SiC (0001) is the most appropriate synthesis method to grow few layer graphene with controllable coordinate directly on insulating substrates, which provides a potential of graphene/SiC wafer based electronic devices. However, as the nature of graphene formation on SiC, the random decomposition of SiC substrates brings about the rough graphene surfaces with small domain sizes. To approach the applications of graphene on electronic devices, having a reproducible, accurate and controllable graphene growth method for atomic flat surfaces at wafer-scale and large domain sizes (order of 10  $\mu\text{m}$ ) is still a big challenge. Thus, further understandings of graphene growth mechanism and processes are also necessary.

In this research, we investigate the graphene/SiC (0001) substrates mainly by utilizing a UHV-scanning electron microscope/scanning tunneling microscope (UHV-SEM/STM) system. SiC substrates are annealed in various atmospheres, i.e. UHV, Ar, O<sub>2</sub> in this study, and evolution of surface morphology is characterized by

this *in situ* STM and SEM system. Thus, technology and mechanism of graphene fabrication on SiC (0001) for application of electronic devices are studied.

In the following chapters, principles and methods of sample preparation and characterization are introduced firstly in chapter 2. The central equipment in this research, the *in situ* UHV-SEM/STM system, is also explained in the latter part of the chapter.

In Chapter 3, to have a better understanding of graphene growth mechanism on SiC (0001) in argon atmosphere and improve this graphene growth method for wafer scale applications, the influences of SiC surface morphology, gas pressure, and annealing temperature during the growth are investigated. And by observing the surface morphology changes during graphene growth at the same positions on a sample surface, the forming processes of the monolayer graphene are discussed.

In Chapter 4, we found that an annealing of graphene/SiC (0001) substrate in an O<sub>2</sub>-Ar atmosphere can selectively etch the surface buffer layer on SiC terraces and left the monolayer graphene intact, by which monolayer graphene with free edges (open edges) was fabricated. The annealing processes are also observed by the *in situ* UHV-SEM/STM system and the etching mechanisms are discussed.

In Chapter 5, the growth processes of graphene nanoribbon on SiC (0001) are studied by the *in situ* UHV-SEM/STM system and discussed. The selectively etching is also carried out to fabricate graphene nanoribbons with free edges.

In Chapter 6, we will summarize this research and explain my perspective on the growth of epitaxial graphene on SiC (0001) by thermal decomposition and prospect of carbon nanomaterials.

## Chapter 2 Experimental Methods

### 2.1 Preparation of samples

#### 2.1.1 SiC substrates

In this study, two kinds of SiC (0001) substrates, i.e. vicinal and step-free SiC (0001) substrates, are used. The vicinal SiC substrates are commercial n-type 6H-SiC wafers, which are purchased from TANKEBLUE co. ltd. and cut in a size of  $12\times 3\times 0.33$  mm. The Si-face is polished by chemical-mechanical planarization method (CMP) with a miscut angle of about  $0.14^\circ$ . Due to such miscut angle, there always present SiC-bilayer steps of 0.25 nm in height and terraces of 100 nm in width on the surfaces, as shown by the section drawing in Figure 2.1(a). Steps on SiC substrate have a significant influence on graphene formation, which will be discussed in Chapter 3. Fortunately, we are able to investigate the effect of the surface morphology by using step-free SiC substrates which are supplied from Ujihara et al. for this study. On the surface of the step-free SiC, extremely wide terraces are formed by top seeded solution growth (TSSG) of SiC [41]. By such method, the terraces expand rapidly by step flow on 4H-SiC seed, forming terraces over 100- $\mu\text{m}$  wide and steps with height of about 1  $\mu\text{m}$ , as illustrated in Figure 2.1(b). Figure 2.1(c) shows an SEM image of vicinal SiC, on which weak contrast (highlighted by white dashed lines) indicate the step edges. On the other hand, in Figure 2.1(d), the step edges and wide terraces on step-free SiC surface are observed easily by optical microscope.

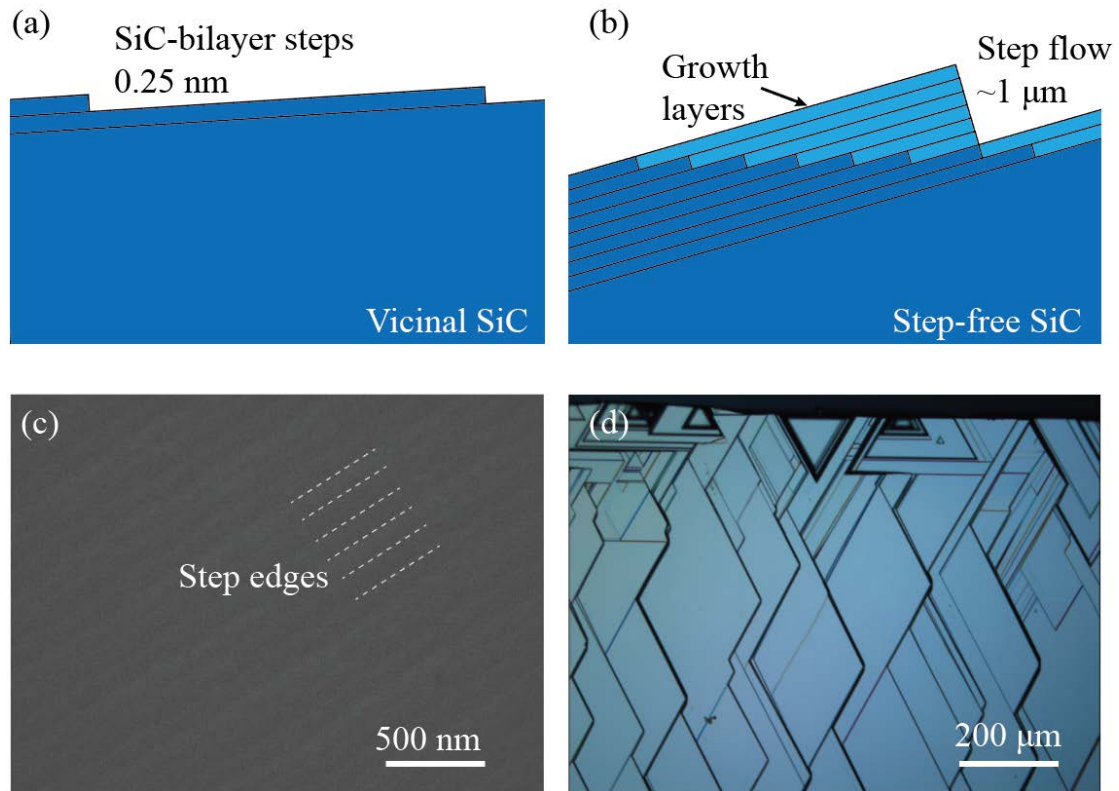


Figure 2.1: Schematic diagrams of the cross-section structure of (a) vicinal SiC (0001) substrates and (b) step-free SiC (0001) substrates. (c) SEM image of vicinal SiC. (d) optical microscope image of step-free SiC.

## 2.1.2 Laser lithography and reactive ion etching

In this research, by utilizing laser lithography and reactive ion etching (RIE), some of the substrates are patterned on the entire surface. To investigate the growth processes of graphene, the patterns are regarded as markers that we can observe the surface changes at the same position after each annealing.

The patterning processes are illustrated in Figure 2.2. Firstly, SiC (0001) substrates are cleaned in acetone by ultrasonic cleaner and then coated with photoresist (AZ P1350) about 500 nm thick on its surfaces by a spin coater (Figure 2.2(a)). After a 1-min prebaking at 100°C, the substrates are sent for the laser lithography. As shown in Figure 2.2(b), the photoresist is exposed to a laser beam with a designed pattern. A chemical change occurs at the exposed part of resist that allows

this resist to be subsequently removed in a solution of developer (Figure 2.2(c)). Thus, a resist mask is formed on the substrate surface. Then a post-baking for 2 min at 120°C is necessary to fix the resist mask before the etching. During the following RIE, as shown in Figure 2.2(d), a plasma of reactive gas is generated by a strong radio frequency electromagnetic field, from which high-energy ions impact and react with the resist-uncovered surfaces. In our case, SiC substrates are etched under the condition of CF<sub>4</sub> (40 sccm) / O<sub>2</sub> (20 sccm) mixture at a power of 200 W for 1 min. Finally, after removing the remained photoresist, a pattern of mesas is fabricated on the surfaces. As shown in a coherence scanning interferometry (CSI) image and its section profile (Figure 2.3), mesas with a height about 70 nm are formed after the patterning.

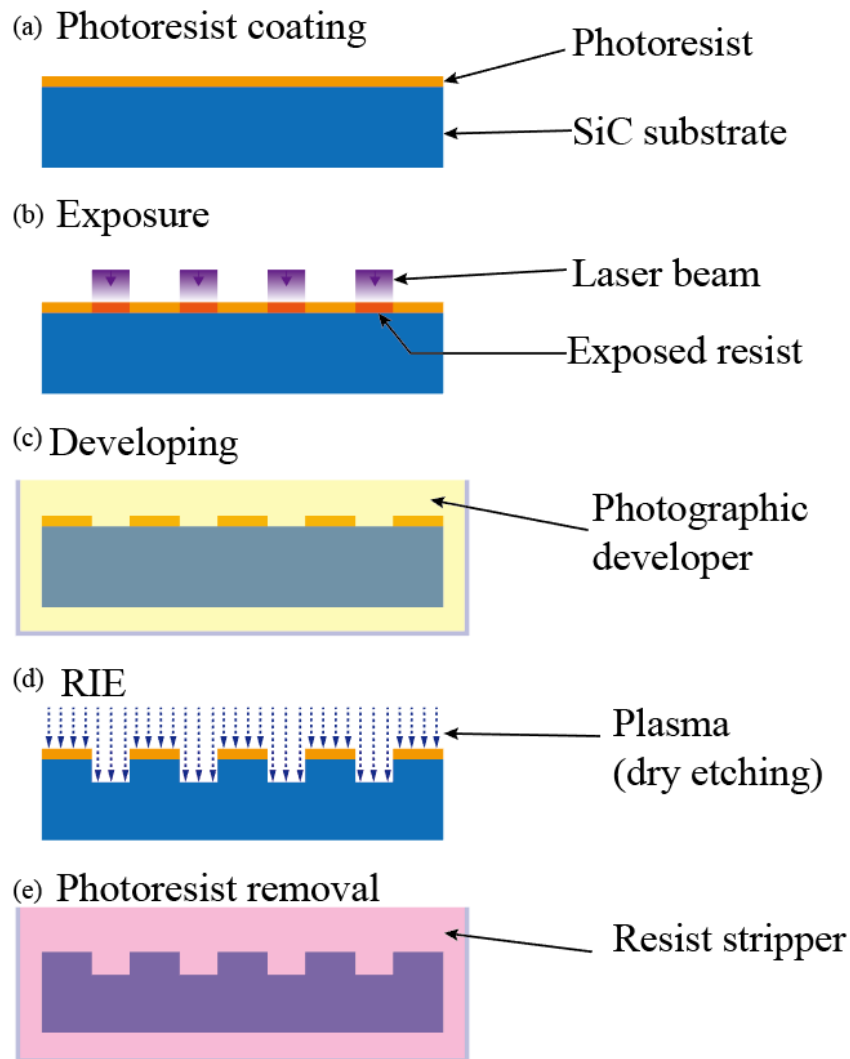


Figure 2.2: Schematic diagrams of the patterning processes by laser lithography and reactive ion etching.

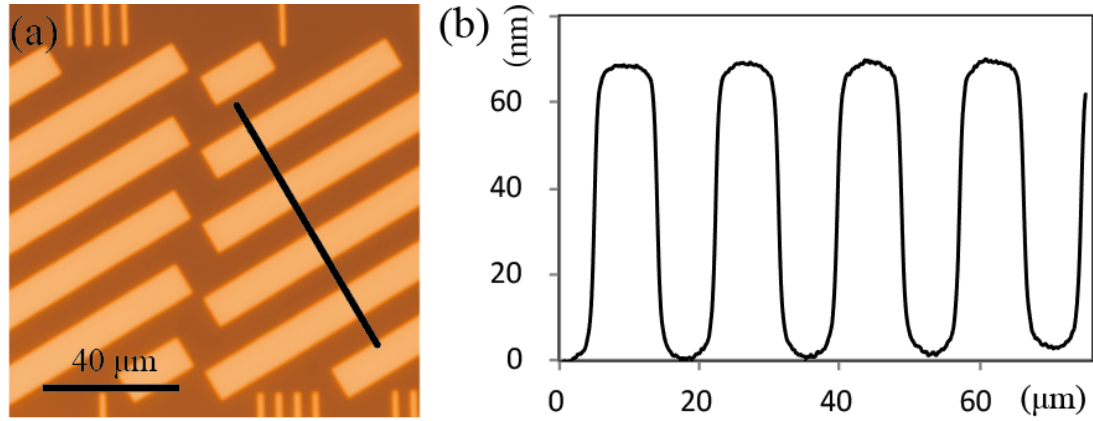


Figure 2.3: (a) Coherence scanning interferometry image of the SiC surface after patterning. (b) Profile along a black line in (a).

### 2.1.3 Annealing

Even in the case of UHV, annealing over 1100°C is necessary for the decomposition of SiC and sublimation of Si to grow epitaxial graphene. To reach such high temperature, several methods have been used for the annealing of SiC substrates, i.e. electromagnetic heating [37], resistive heating (Joule heating) [42], carbon heater [43]. In this study, SiC (0001) substrates are annealed by resistive heating *in situ* UHV-SEM/STM system.

After cleaning or patterning, SiC (0001) substrates are fixed on a molybdenum heating holder as shown in Figure 2.4(a), and transferred into the UHV-SEM/STM system. Notably, this setup always brings about a temperature gradient across the sample during the annealing, i.e. higher temperature at the center and lower temperature near the electrodes. As a result, graphene is firstly formed near the center area of SiC substrate with a size of 3-4 mm and surrounded by buffer layer and SiC regions as shown in Figure 2.4(b). Such three regions are easily recognized in SEM images, which will be shown in the next section. Utilizing this temperature distribution, changes of surface structures at various temperatures regions can be investigated on a sample.

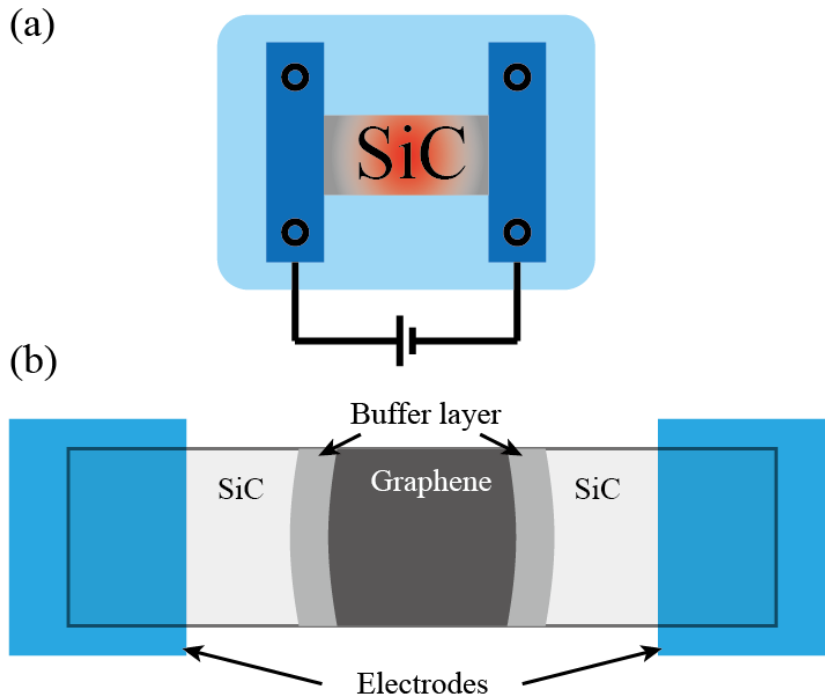


Figure 2.4: Schematic diagrams of (a) the setup of a SiC (0001) substrate in the heating holder and (b) substrate surface after graphene formation.

## 2.2 Characterizations

### 2.2.1 Scanning electron microscopy

SEM (scanning electron microscope) is a member of electron microscopes, which use a high-energy electron beam (range about 100 eV to 30 keV) instead of the light source to investigate sample surfaces. SEM can reach the resolution with the order of 1 nm (comparing to the ~500 nm of optical microscope) due to the extreme short electron wavelength. As shown a schematic diagram of SEM in Figure 2.5, an electron beam generated from an electron gun is focused by condenser lenses, and then passes through a scanning coil to reach the sample surface. The scanning coil is used for adjusting beam position in x-y axes, so that it can scans over an area of the sample surface. When the electron beam hits the surface, and interacts by producing several signals, which include secondary electrons, backscattered electrons, diffracted

back scattered electrons, photons and visible light. Signals of the secondary electrons or backscattered electrons are generally collected by a detector to image the sample surfaces.

Because of the one-atom thickness of graphene, low-voltage SEM contrasts are always used for distinguishing the graphene formation on SiC substrates [44]. In this study, all the SEM images are obtained with a primary electron of 2 keV. For our case, as shown in Figure 2.6(a), because of the temperature gradient across the SiC substrate during annealing, graphene areas with a darker contrast always be at the center, corresponding to the illustration in Figure 2.4(b). Then, three contrasts of bright, gray and dark can be found in turn from the low temperature to the high temperature area, which indicate the regions of SiC, buffer layer and graphene regions respectively (Figures 2.6(b) and (c)).

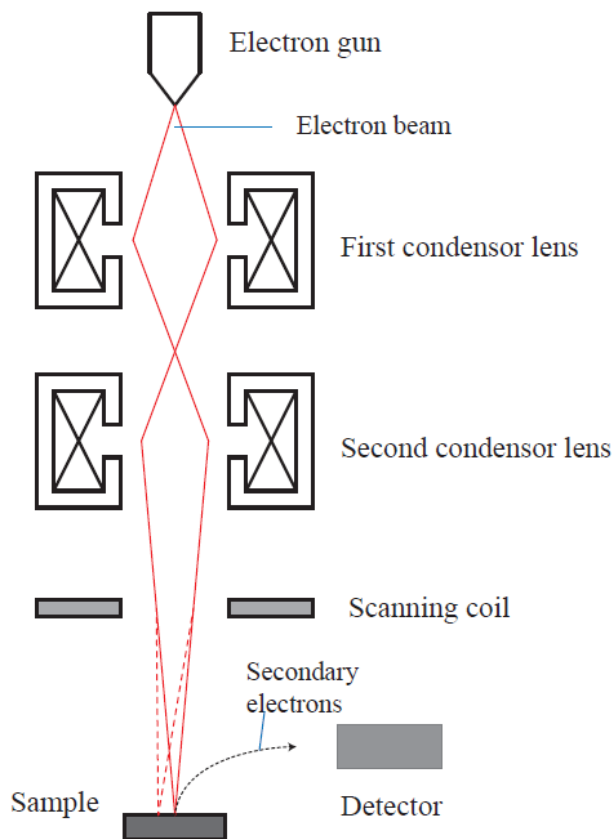


Figure 2.5: Schematic graph of basic SEM equipment.

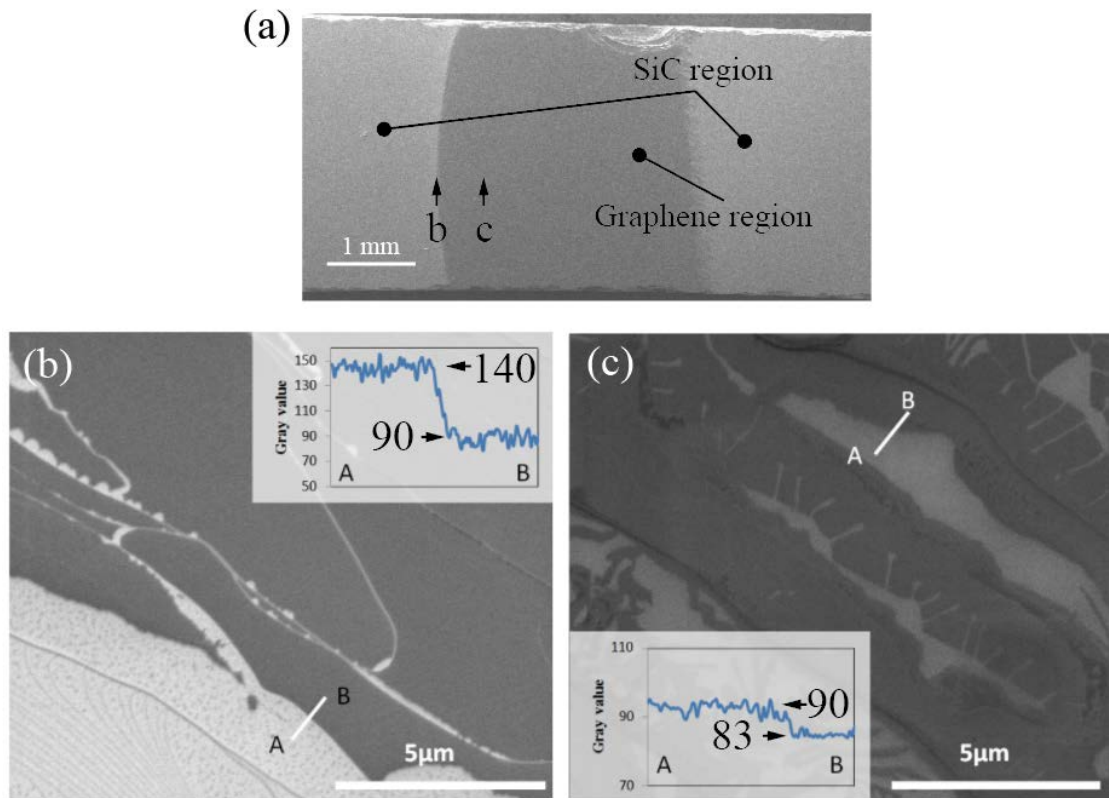


Figure 2.6 (a) SEM image of a SiC (0001) substrate surface after graphene formation, (b) and (c) magnified SEM images at position b and c in (a). The insert profiles in (b) and (c) indicate the contrast change of gray value along the white line from A to B.

## 2.2.2 Scanning tunneling microscopy

As a member of scanning probe microscopes (SPMs), STM (scanning tunneling microscope) is a well-developed instrument to obtain atomic level images of conductive sample surfaces. As showing in Figure 2.7, sample surfaces are imaged through the tunneling current between an atom on the tip of the probe and the atoms on sample surface, which can obtain the lateral resolution of 0.1 nm and depth resolution of 0.01 nm. For STM imaging, firstly, a probe is approached to the sample surface, with applying a bias voltage between the probe and the sample, until they are close enough to observe tunneling current; the gap between the tip and the sample surface is on the order of few nanometers. Then the probe scans across an area of

sample surface, and the surface of the area is mapped in images by the changes of tunneling current (constant height mode) or the changes of tip height (constant current mode). Because the tunneling current changes according to not only surface height but also density of states, an STM image includes information of both surface height and material changes.

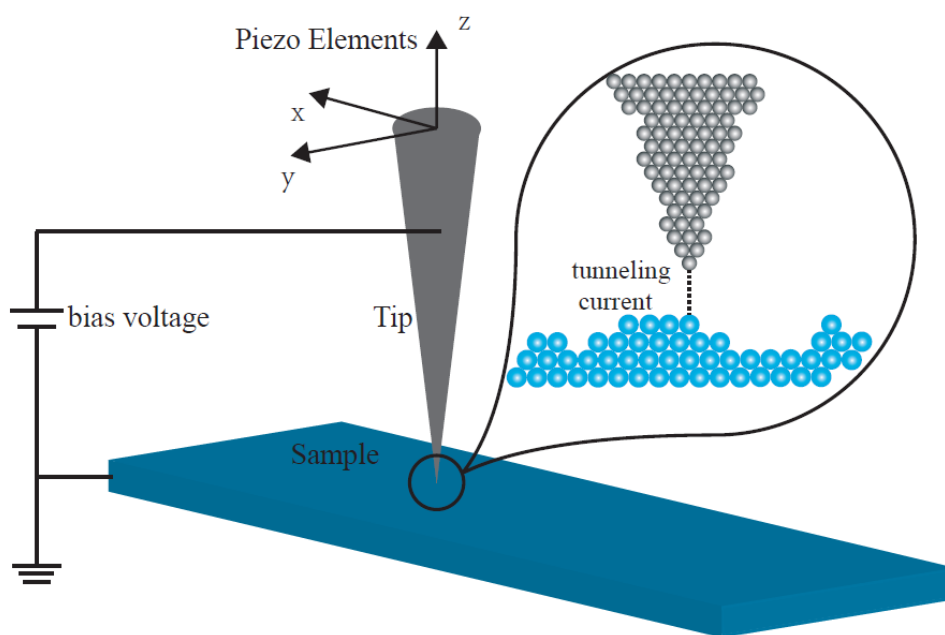


Figure 2.7: Schematic diagram of STM principle.

Tungsten (W) tips are used as STM probes in this work, which are prepared by electropolishing W wires. The electropolishing is a general technology to process metal materials, by which the metal materials will be etched as an anode in an electrolytic solution to achieve an expected shape. A schematic diagram of our setup of the electropolishing apparatus is shown in Figure 2.8. a W wire ( $\Phi 0.3$ ) is fixed as the anode and crossed through the center of a platinum (Pt) ring in sodium hydroxide (NaOH) aqueous solution (2 mol/l). The polishing starts by applying an adjustable voltage and stops automatically by monitoring a current change when the W wire is cut off. The curvature radius of the probe tip can be adjusted by the etching voltage, and the tip radius of less than 100 nm is used as STM probes.

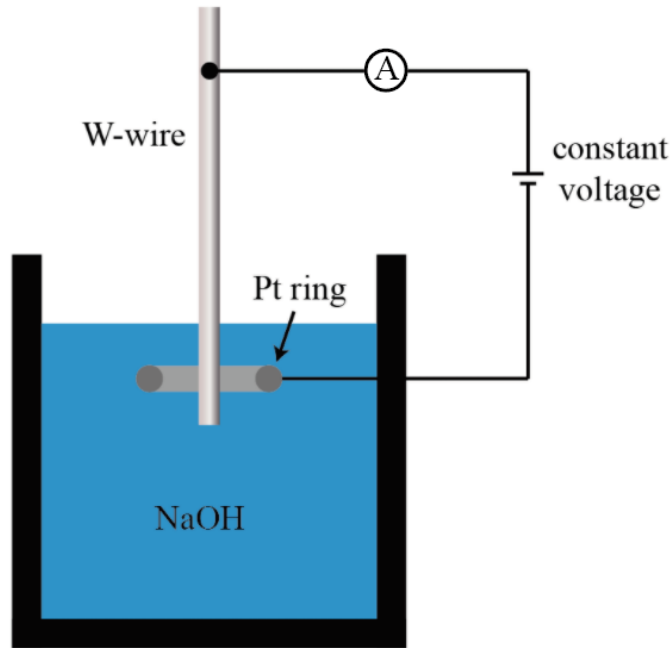


Figure 2.8: Setup of electroplishing apparatus for preparation of STM probes.

For the graphene on SiC (0001) substrates, a SiC ( $6\times 6$ ) moiré pattern is usually observed at the graphene formed areas by STM [46, 47]. As shown in Figure 2.9, a green dashed rhombus of the SiC ( $6\times 6$ ) is actually a quasi-cell of SiC ( $6\sqrt{3}\times 6\sqrt{3}$ )R $30^\circ$ . STM images always fail to recognize the ( $6\sqrt{3}\times 6\sqrt{3}$ )R $30^\circ$  structure and shows a quasi-cell the ( $6\times 6$ ) moiré pattern. Also, importantly, such moiré pattern demonstrates the existence of a buffer layer underneath the graphene. The locations of the sample surfaces where STM images are taken can be indicated by comparing with the SEM images at the same position, due to the *in situ* SEM/STM system, which will be introduced in Section 2.3.

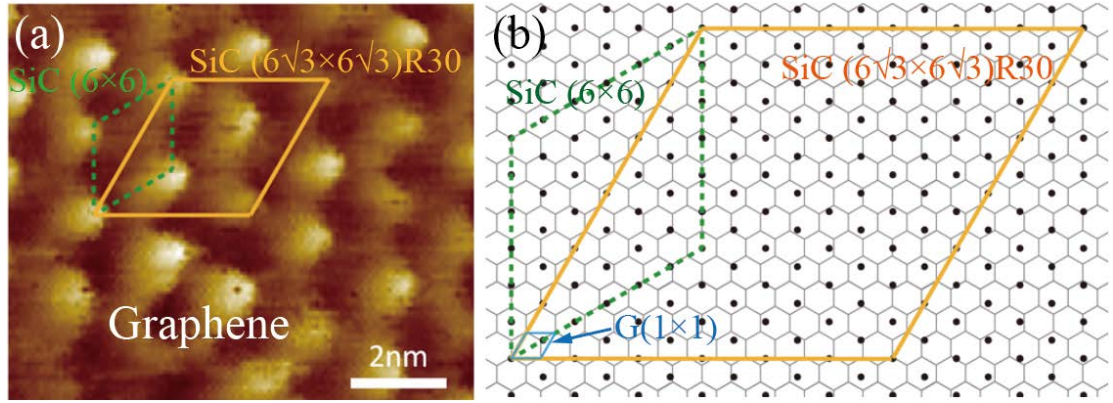


Figure 2.9: (a) STM image showing a moiré pattern of monolayer graphene with buffer layer underneath. (b) Atomic structure of the first graphite layer (buffer layer) on SiC surface, explaining the formation of moiré patterns. The buffer layer is shown as the gray honeycomb, and Si atoms in top layer of SiC are shown as the black balls. Blue and yellow rhombi indicate a graphite (1×1) unit cell and a SiC ( $6\sqrt{3} \times 6\sqrt{3}$ )R30° unit cell, respectively. A green dashed rhombus indicates the quasi-cell of SiC (6 × 6).

### 2.2.3 Reflection high-energy electron diffraction

Reflection high energy electron diffraction (RHEED) is a very efficient technique to investigate the surface crystallographic structure of materials. As shown in Figure 2.10, a high energy electron beam from an electron gun strikes the sample with an incident angle  $\theta$ , and then scattering of electrons from atoms at lattices of the sample surface occurs. The scattered electrons interfere at specific angles and reach the screen to form diffraction patterns (called RHEED patterns). The relation of sample surface structure and RHEED patterns is generally investigated by using Ewald's construction, which can demonstrate allowed diffraction conditions. As shown in Figure 2.11, Electrons are diffracted to the directions corresponding to the intersection of the reciprocal lattice rods and Ewald's sphere.

RHEED has been applied to study the reconstructions on SiC formed by annealing [48]. The patterns of SiC (1×1), SiC (3×3), SiC ( $\sqrt{3} \times \sqrt{3}$ )R30°, SiC

$(6\sqrt{3} \times 6\sqrt{3})R30^\circ$  and  $G(1 \times 1)$  were generally observed during the graphene formation on SiC substrates.

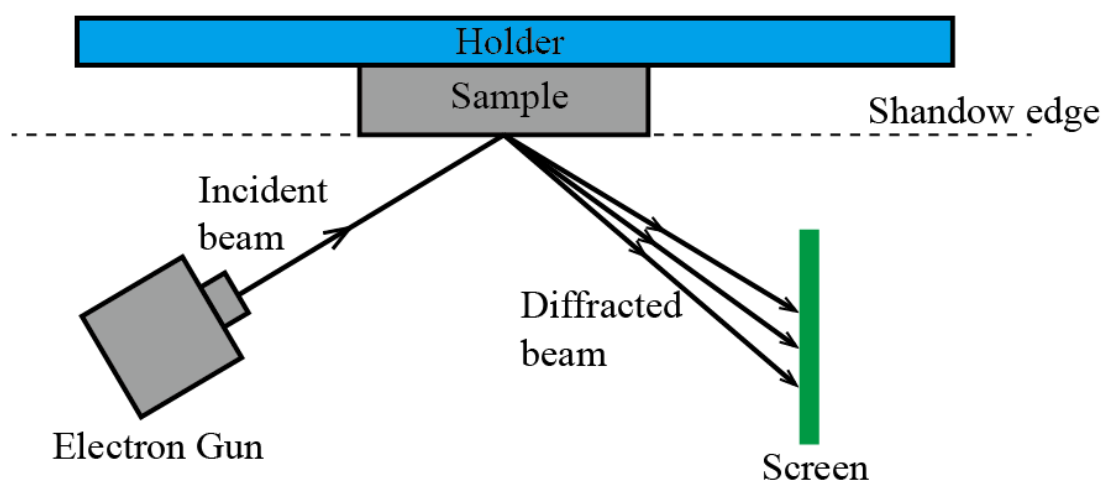


Figure 2.10: Schematic diagram of RHEED equipment.

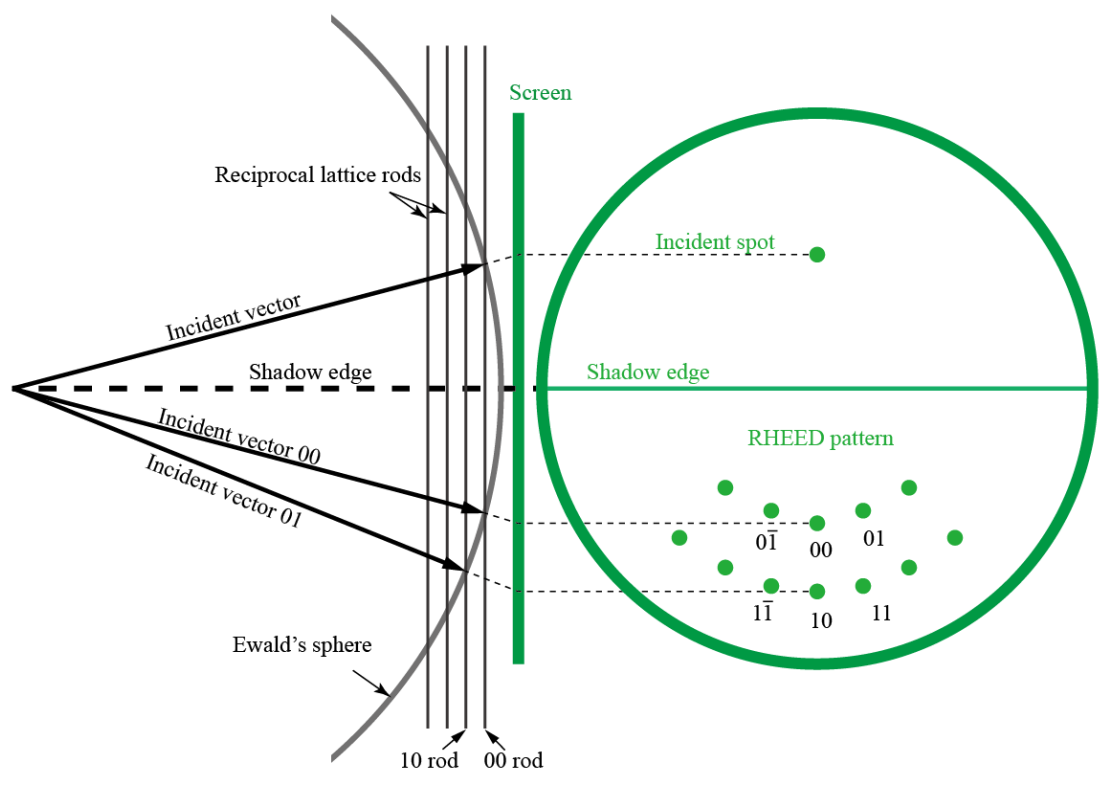


Figure 2.11: Schematic diagram illustrating the relation between the Ewald's sphere, reciprocal lattice rods and RHEED patterns.

## 2.2.4 Atomic force microscopy

Atomic force microscope (AFM) is one of SPM methods which can investigate the surface of both conducting and insulating materials. In AFM, as shown in Figure 2.12, a probe (under the tip of a cantilever) is tapping and scanning on the sample's surface. Under a constant force between atoms at the tip and atoms at the sample surface, the probe moves up and down with the surface and push the cantilever. A laser beam is reflected from the cantilever and the position change of the reflected laser beam is observed by a detector. By utilizing different signal acquisition methods, topography and phase images will be generated in AFM. Topography images intuitively demonstrate the height information of the surface. Phase images are plotted from a phase change between the applying vibration of cantilever and the vibration signal of laser, which is sensitive to the stiffness or adhesion of the sample surface. Such that, it also includes an information of surface material change in the phase images.

Due to various surface areas of SiC, buffer layer and graphene on the graphene/SiC samples, it is difficult to measure the height change between these areas by STM. Observations by ex situ AFM are carried out after the graphene formations, as shown in Figure 2.13, and the areas of graphene and buffer layer can be easily recognized by the phase images.

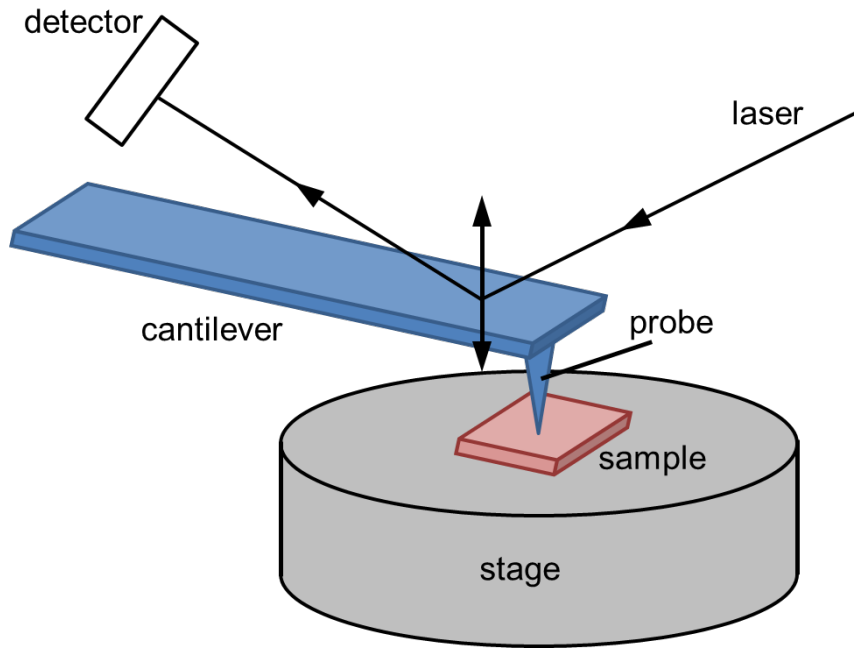


Figure 2.12: Schematic diagram of AFM.

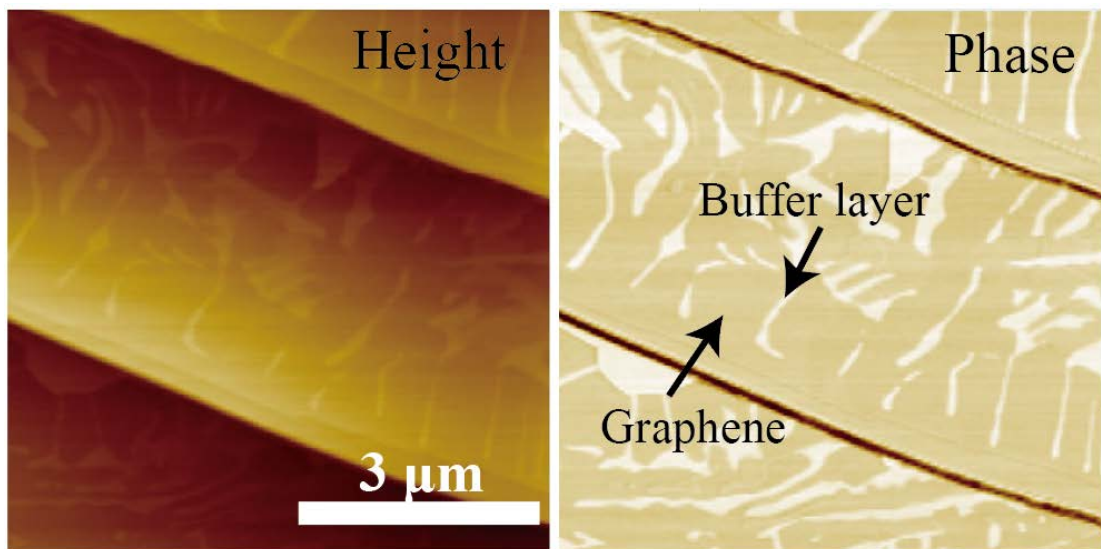


Figure 2.13: AFM height image and phase image of a graphene formed SiC (0001) substrate.

## 2.2.5 Raman spectroscopy

Raman spectroscopy is a spectroscopic technique to qualitatively and quantitatively analyze materials based by Raman scattering. A laser beam with the

frequency of  $\nu_0$  illuminates a sample, and scattered lights ( $\nu_0, \nu_0 \pm \nu_1, \nu_0 \pm \nu_2, \nu_0 \pm \nu_3 \dots \nu_0 \pm \nu_i \dots (\nu_i > 0)$ ) are collected. The lights with the same frequency ( $\nu_0$ ) due to elastic Rayleigh scattering is filtered out while the lights ( $\nu_0 \pm \nu_i$ ) from Raman scattering are measured by a spectrometer. The frequency changes  $\pm\nu_i$  between the incident laser and scattered lights are Raman shifts, which are inherent for materials. As shown in Figure 2.14, there are two types of Raman scattering: Stokes Raman scattering and anti-Stokes Raman scattering. If the energy of final vibrational state is higher than the initial state, the emitted photon shifts to a lower frequency and Raman shift will be  $-\nu_i$ , which is called Stokes shift. Such Raman scattering is called Stokes Raman scattering. On the contrary, if the final vibrational state is lower than the initial state, it is anti-Stokes Raman scattering and anti-Stokes shift will be  $+\nu_i$ . We generally obtain Raman spectra by measuring the signal of Stokes Raman scattered lights. The spectrum is plotted by taking Raman intensities as the vertical coordinate and Raman shifts as the horizontal coordinates. If Raman spectra are measured by scanning the laser beam on an area of the surface, a two-dimensional Raman map can be drawn by using various signals, such as an intensity mapping of specific Raman shift or a Raman shift mapping of a characteristic peak.

Usually, three peaks appear in Raman spectra for carbon materials in which carbon atoms are bonded in  $sp^2$  hybridization [49, 50], which are so-called G, D and 2D bands. The peaks of G-band appear at  $\sim 1600 \text{ cm}^{-1}$ , derived from the graphite-like in-plane mode. D-band peaks commonly at  $\sim 1350 \text{ cm}^{-1}$  are induced by disorders. The intensity of D peaks becomes stronger due to an increasing of defects or edges in graphene. The peaks of 2D-band appear  $\sim 2700 \text{ cm}^{-1}$  which are the second-order of D-band, involving two iTO (in-plane transverse optical phonons) modes near the Dirac points.

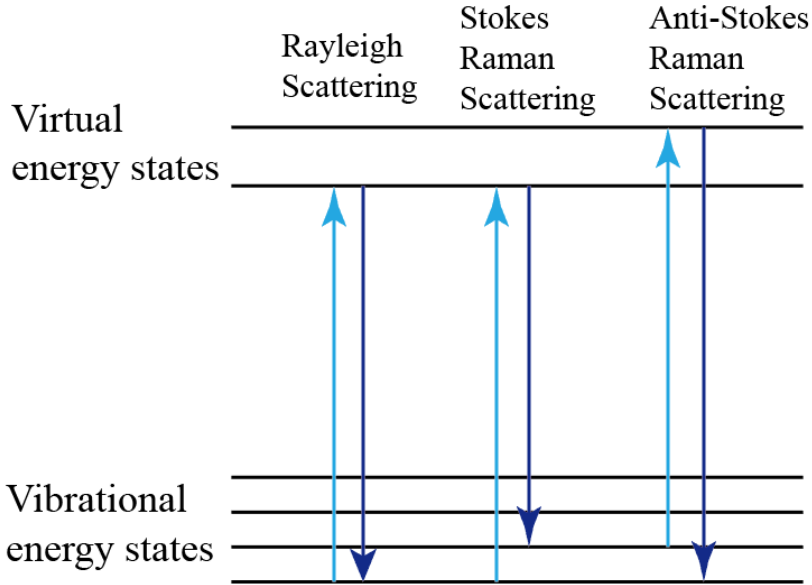


Figure 2.14: Schematic diagram of different Raman scattering types.

## 2.3 Setup of *in situ* UHV-SEM/STM system

Figure 2.15 shows a schematic diagram and a picture of the *in situ* UHV-SEM/STM system utilized in this research. This system is composed of three chambers, which are an exchange chamber, a main chamber and a preparation chamber. The exchange chamber is used to introduce the samples and STM probes from the air into the vacuum system. Then the samples can be transferred to the main chamber, where SEM and STM measurements are carried out. In this setup, the probe of STM is obliquely approached to sample, which allows the observation of position of the probe by the SEM. Thus, the surface morphology at a position can be observed and compared between SEM and STM images, as shown in Figure 2.16. The preparation chamber is a customized part of the system where the samples are annealed, and their surface structures are observed by RHEED. A set of a rotary pump and turbo molecular pump is connected to the exchange chamber and main chamber, and two ion pumps are used to maintain the ultra-high vacuum for main chamber ( $\sim 1 \times 10^{-8}$  Pa) and preparation chamber ( $\sim 1 \times 10^{-7}$  Pa).

To investigate different stages of graphene growth on SiC substrates in a gas atmosphere, pipes for gas-introduction and an independent pumping system (red parts in Figure 2.15(a)) are added to the preparation chamber. Thus, the fabrication of graphene and its characterizations by SEM, STM and RHEED can be carried out in one vacuum system without exposing to the air.

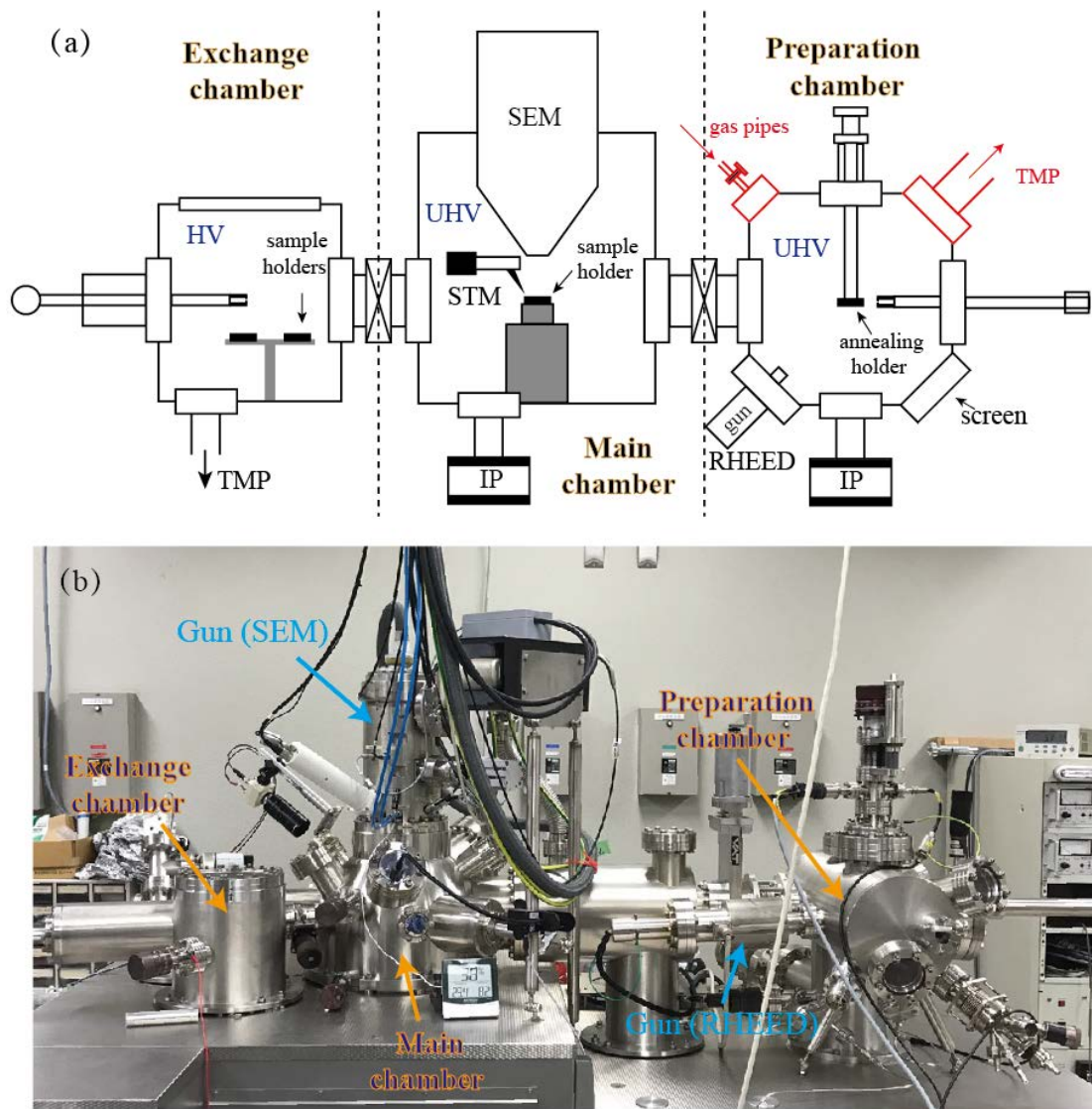


Figure 2.15: (a) Schematic diagram and (b) picture of the *in situ* UHV-SEM/STM system.

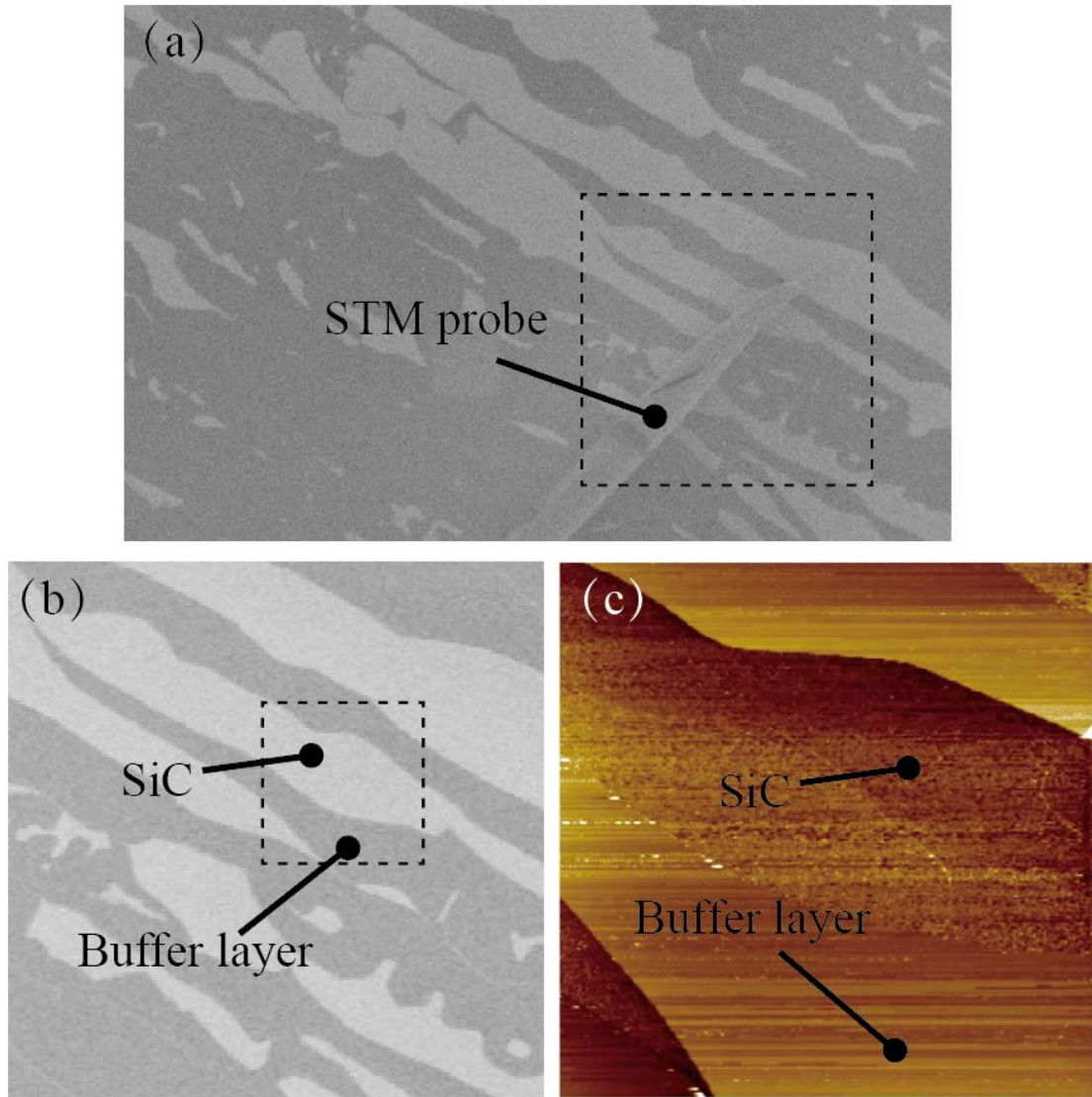


Figure 2.16: (a) SEM image of a buffer layer/SiC area on graphene formed SiC (0001) substrate with the STM probe over it. (b) Close-up SEM image of the black dashed area in (a) (the STM probe is moved away). (c) STM image scanned over the area of a black dashed frame in (b).

# Chapter 3 Graphene Growth on SiC (0001) Under Argon Atmosphere

## 3.1 Introduction

It is known that the graphene growth processes during thermal decomposition of SiC (0001) surface are dominated by many parameters such as surface morphology (step edges, terraces), atmosphere (UHV, inert gases, Si vapor) and annealing temperature and duration. In general, there are two kinds of graphene nucleation due to the surface morphology as shown in Figure 3.1; one is the growth from step edges where SiC decompose most effectively, and another is the growth from pits which are formed by Si sublimation on terraces [25]. When a pit is opened on a terrace the pit edges act as the same as step edges where graphene extends. The pit formation leads to a decrease of graphene domain size by increasing graphene nucleus density. Sun et al. [37] reported that the SiC surfaces with abundant steps are necessary to fabricate pit-free graphene on SiC substrates. Although the pit formation is suppressed, graphene nucleus density is still considerably high because of the abundant step edges. Also, annealing of SiC substrates in an atmosphere, such as inert gas [37] and Si vapor [38], slows down the decomposition rate and suppresses the formation of pit. Recently, graphene growth in Ar atmosphere has been widely used to produce few-layer and large-scale epitaxial graphene on SiC substrate. However, due to the complex annealing parameters, the growth process of graphene in Ar atmosphere is not well understood and many questions on its growth mechanism remain still.

In this chapter, the influences of SiC surface morphology, gas pressure, and annealing temperature on graphene growth on SiC (0001) in Ar atmosphere are investigated by *in situ* SEM/STM system. The changes of surface morphology during graphene growth at same position on a sample surface are also observed to study the monolayer graphene forming process.

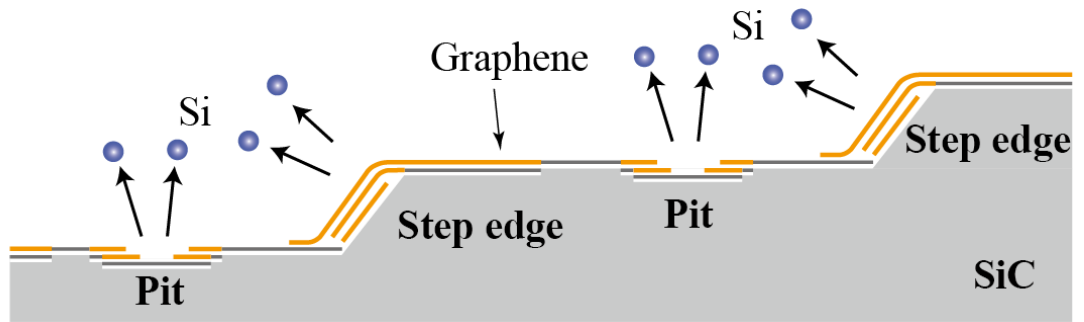


Figure 3.1: Schematic diagram of graphene nucleation on SiC (0001) surface.

## 3.2 Experimental and results

### 3.2.1 Graphene growth on step-free SiC surfaces

Step-free SiC (0001) substrates were annealed for graphene formation under the following three conditions, (i) from 900°C to 1300°C (by 100°C step, 10 min per step) in UHV, (ii) from 1400°C to 1600°C (by 100°C step, 20 min per step) in 1 atm Ar and (iii) 1550 °C for 1 h in 1 atm Ar. All three conditions result in formation of graphene on SiC surface. The graphene formation was confirmed by *in situ* RHEED and surface morphology of the samples after graphene growth is measured by *ex situ* AFM.

Figure 3.2 shows height and phase AFM images of the surface after graphene growth under these three annealing conditions. In the height AFM images, depression areas are pits formed by the decomposition of surface SiC. Graphene is formed in the pits as confirmed by the dark contrasts in the phase AFM images. For the condition (i), as shown in Figures 3.2(a) and (b), high density of pit formation leads the size of graphene domains grown to about 100 nm. For the condition (ii), as shown in Figures 3.2(c) and (d), less pits are formed on the surface than condition (i) and monolayer graphene in the size about 2  $\mu\text{m}$  is confirmed. Also, multilayer graphene near edges and buffer layer islands (white arrows) are observed. Besides the above two conditions, Figures 3.2(e) and (f) show the surfaces after annealed under the condition

(iii), where a monolayer graphene domain formed in a pit with the size about 10  $\mu\text{m}$ . The annealing conditions and domain sizes of graphene are summarized in Table 3.1.

Table 3.1: Annealing conditions and domain sizes of graphene grown on step-free SiC (0001).

<b>Annealing</b>	<b>Conditions</b>	<b>Max domain sizes</b>
<b>i</b>	1300°C, 10 min, UHV	100 nm
<b>ii</b>	1600°C, 20 min, 1-atm Ar	2 $\mu\text{m}$
<b>iii</b>	1550°C, 1 hour, 1-atm Ar	10 $\mu\text{m}$

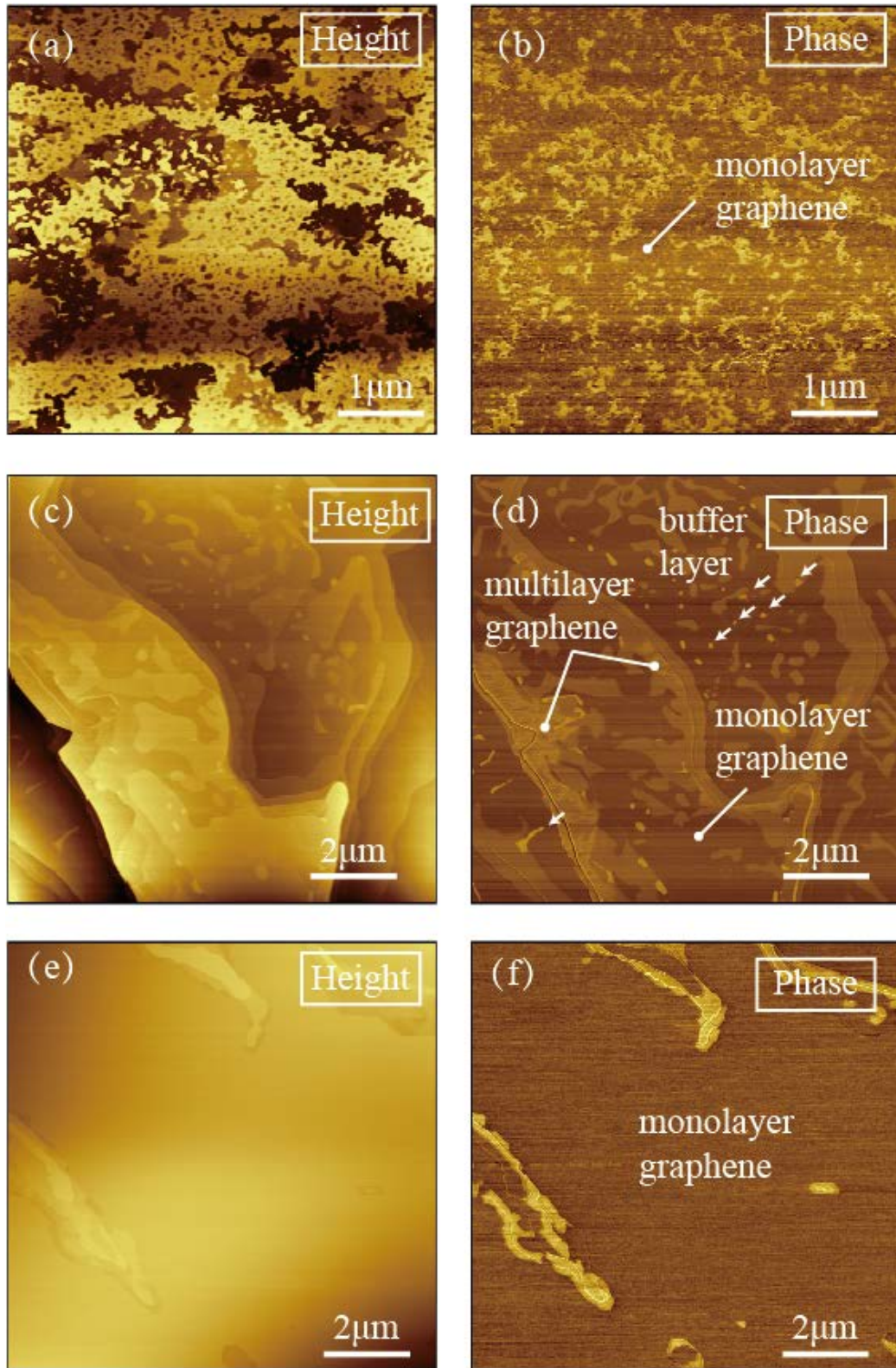


Figure 3.2: AFM height and phase images of step-free SiC (0001) surface after annealing at (a, b) 1300°C for 10 min in UHV, (c, d) 1600°C for 20 min in 1 atm Ar, and (e, f) 1550°C for 1 h in 1 atm Ar.

### 3.2.2 Graphene growth at various pressures and temperatures

Three vicinal SiC (0001) substrates were annealed in Ar atmospheres of 0.5 atm, 0.1 atm and 1 atm respectively. Each sample was heated repeatedly for several times at various temperatures from 1300°C until the graphene formation. The annealing durations at different temperatures of the three samples are listed in Table 3.2, Table 3.3 and Table 3.4. For the case of the annealing at 0.5 atm Ar, the sample was annealed once for each temperature and investigated by *in situ* RHEED and STM after each annealing step. For the cases of 0.1 atm and 1 atm, the samples were annealed several times at same temperature, for the sake of surface morphology changes at the same temperatures.

#### Annealing at 0.5 atm Ar

Figure 3.3 shows a series of STM images of the sample surfaces after each annealing at various temperatures under Ar at the pressure of 0.5 atm. Step bunching takes place during the annealing processes, leading to the growth of flat terraces. After the hydrogen etching (1300°C, 15 min, 0.1 atm H<sub>2</sub>), in Figure 3.3(a), a terrace with the width of about 300 nm forms, and the step height is 0.75 nm, corresponding to the 3 SiC-bilayer steps on the surface. Subsequently, the substrate is annealed at 1300°C. As shown in Figure 3.3(b), a terrace grows to about 600 nm (twice the width of the terraces at previous stage in Figure 3.3(a)), and the step height is 1.5 nm which corresponds to the formation of 6 bilayer steps on the surface. After that, steps bunch further by subsequent annealing as shown in Figures 3.3(c) and (d) after the annealing at 1400°C and 1480°C, and finally terraces grow to more than 4 μm in width after 1520°C annealing as shown in Figure 3.3(e).

RHEED patterns in  $[10\bar{1}0]$  azimuth of the SiC substrate is shown in Figure 3.4, which indicates the change of surface structures during the annealing process. It

firstly presents clear spots (downward triangles) of SiC ( $1 \times 1$ ) (SiC stoichiometric surface) after hydrogen etching as shown in Figure 3.4(a). In Figure 3.4(b), by subsequent heating at  $1300^\circ\text{C}$ , weak spots (downward triangles) of SiC ( $3 \times 3$ ) appears. Then the SiC ( $1 \times 1$ ) surface shows up again after the annealing at  $1400^\circ\text{C}$ , as shown the downward triangles in Figure 3.4(c). Finally, the patterns of SiC ( $6\sqrt{3} \times 6\sqrt{3}$ ) $R30^\circ$  and graphene ( $1 \times 1$ ) (spots marked by downward triangles) are observed after annealing at  $1480^\circ\text{C}$  (Figure 3.4(d)) which suggests that buffer layers and graphene are formed on SiC surface. And satellite spots (shown by arrows) also appear due to secondary scatterings between SiC and graphene [48].

### **Annealing at 0.1-atm and 1 atm Ar**

The step-bunching behavior is further investigated by measuring average terrace widths of the samples during annealing under 0.1 and 1 atm Ar. Figure 3.5 shows the terrace width as a function of the annealing temperature. Terrace width increases most rapidly at the annealing temperature of  $1400^\circ\text{C}$  in the both annealing condition of Ar pressures.

Figure 3.6 shows STM images of graphene formed surfaces under these three different Ar pressures (0.1, 0.5 and 1 atm). Although, after the long-time annealing pits extend and connect to each other, deep depression areas (white arrows) can be observed as the centers of the pits. As shown in Figure 3.6 the pit formation is dramatically reduced in Ar of 1 atm than that of 0.1 atm. Although the Ar pressure did not show any significant effect on the step-bunching process, it played a vital role for suppressing the formation of pits due to the decomposition of SiC on terraces. In other words, it is found that terraces width is determined by the annealing temperature and duration, while the pit formation depends on Ar pressure.

Table 3.2: Annealing durations of the sample annealed in 0.5-atm-Ar.

<b>Temperature</b>	<b>1300°C</b>	<b>1400°C</b>	<b>1480°C</b>	<b>1520 °C</b>	<b>1550°C</b>
<b>Duration</b>	30 min	15 min	15 min	8 min	8 min

Table 3.3: Annealing durations of the sample annealed in 0.1-atm-Ar.

<b>Temperature</b>	<b>First time</b>	<b>Second time</b>	<b>Third time</b>
<b>1300°C</b>	15 min	15 min	15 min
<b>1400°C</b>	15 min	15 min	15 min
<b>1450°C</b>	15 min	15 min	15 min
<b>1500°C</b>	15 min	15 min	15 min

Table 3.4: Annealing durations of the sample annealed in 1-atm-Ar.

<b>Temperature</b>	<b>First time</b>	<b>Second time</b>	<b>Third time</b>	<b>Fourth time</b>
<b>1300°C</b>	30 min	30 min		
<b>1400°C</b>	30 min	15 min	15 min	
<b>1450°C</b>	15 min	15 min	15 min	15 min
<b>1500°C</b>	15 min	15 min		
<b>1550°C</b>	15 min	15 min		
<b>1600°C</b>	15 min			

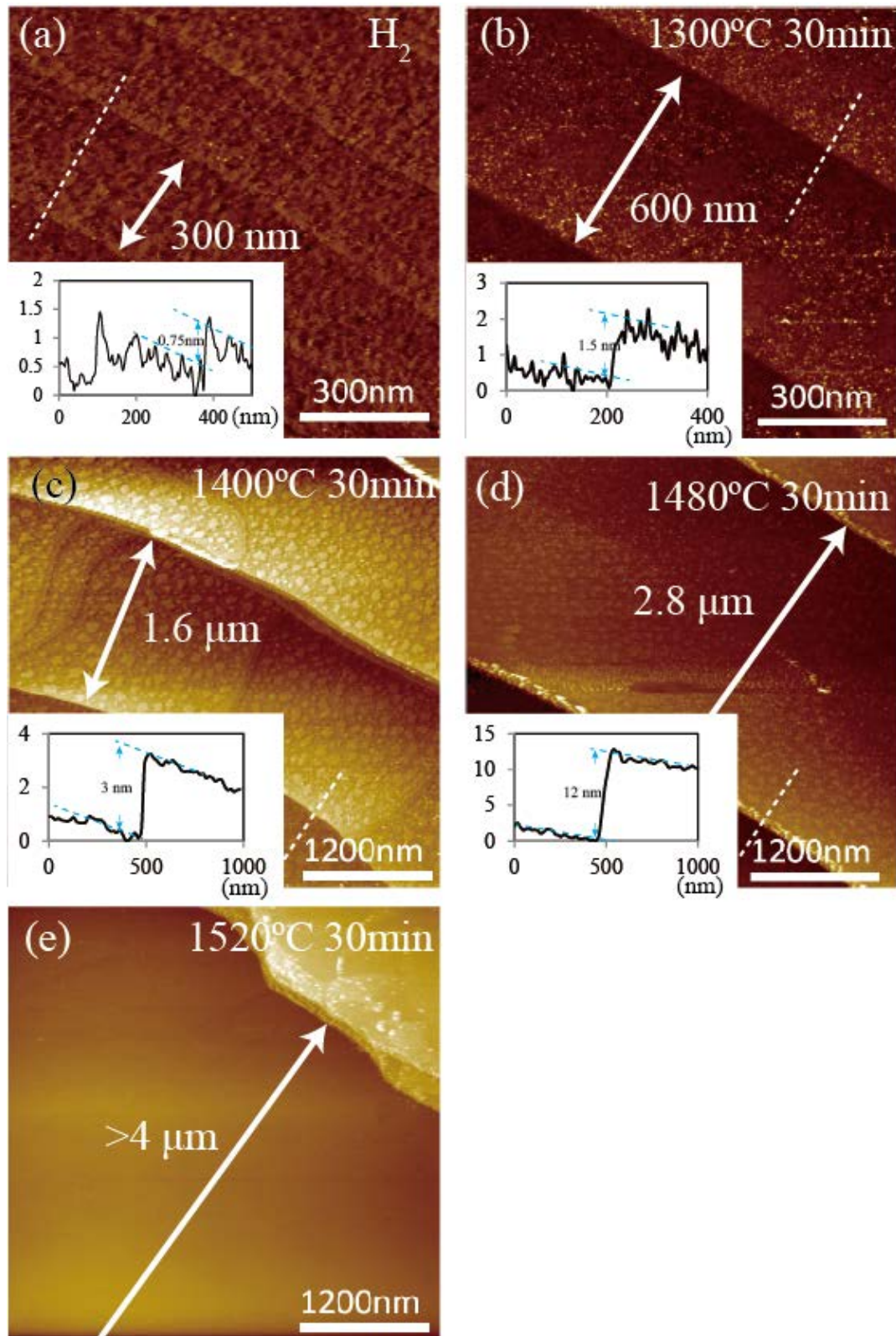


Figure 3.3: STM images of vicinal SiC (0001) substrate after (a) hydrogen etching, (b) 1300°C, (c) 1400°C, (d) 1480°C, (e) 1520°C annealing in 0.5 atm Ar. Inserts in (a-d) are profile of dashed lines in the STM images. (a-d): Tip bias voltage  $V_b = -1.5$  V, tunneling current  $I_t = 0.1$  nA. (e) bias voltage  $V_b = 0.1$  V, tunneling current  $I_t = 0.1$  nA.

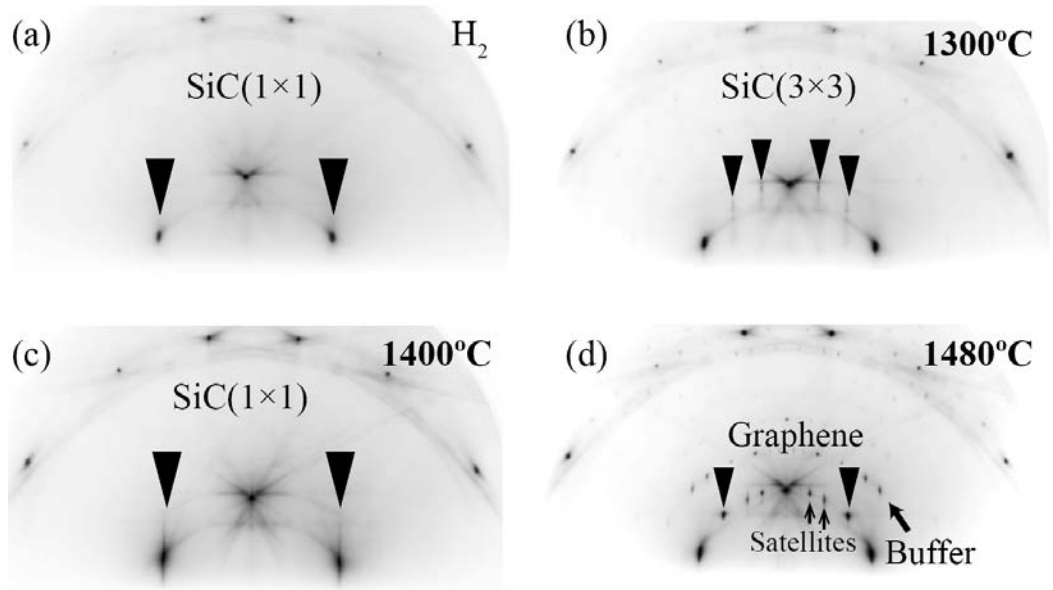


Figure 3.4: RHEED patterns of the sample after (a) hydrogen-etching, and annealing at (b)  $1300^\circ C$  (c)  $1400^\circ C$ , (d)  $1480^\circ C$  in 0.5-atm-Ar atmosphere, in the azimuths of  $[10\bar{1}0]$ .

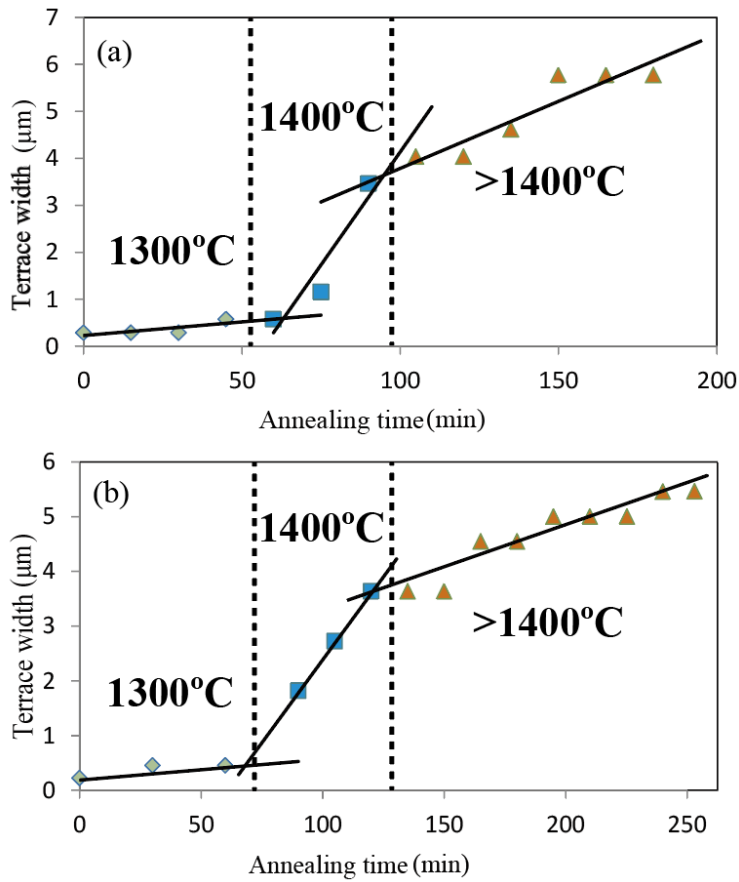


Figure 3.5: Average width of terraces versus annealing time, (a) in 0.1 atm Ar; (b) in 1 atm Ar.

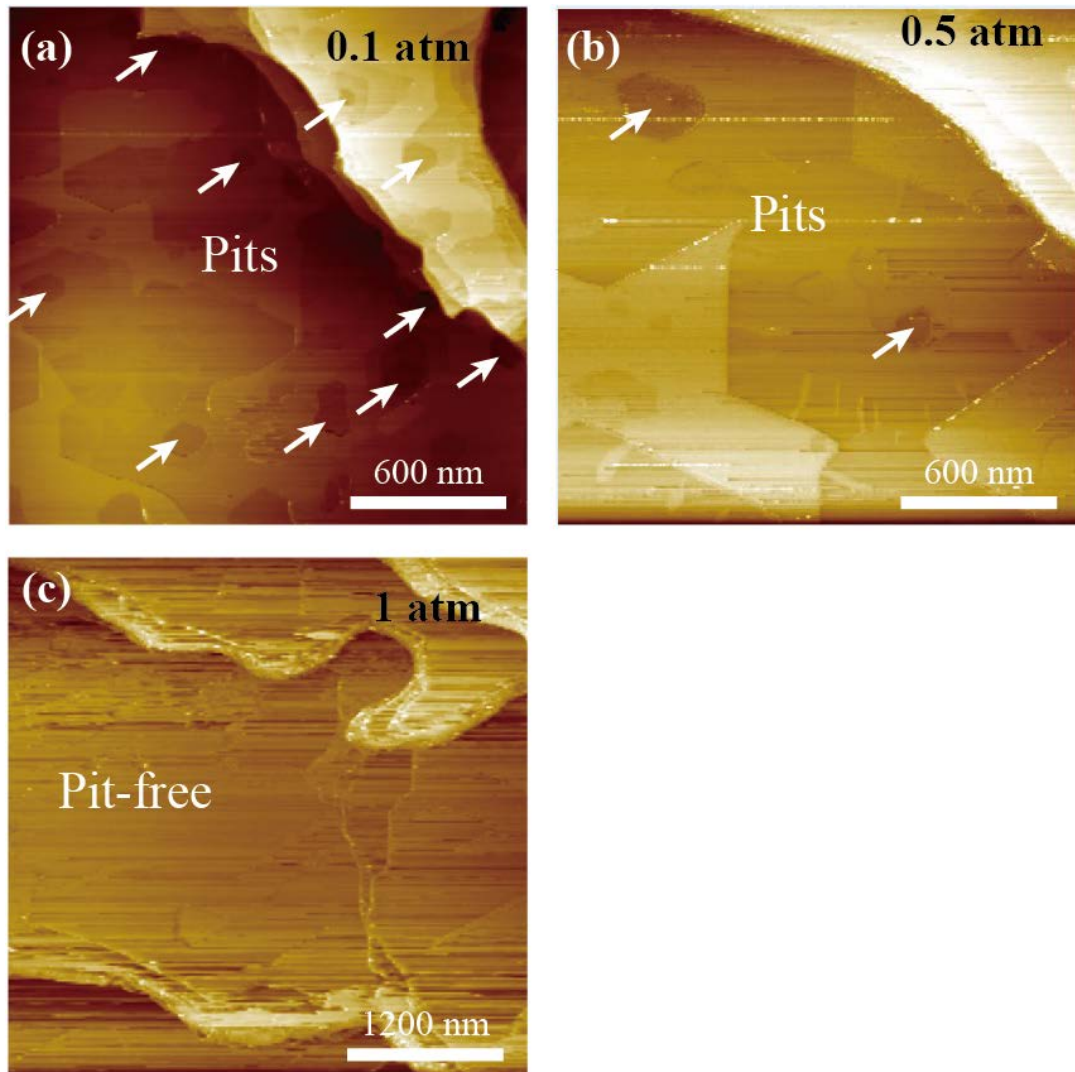


Figure 3.6: STM images of SiC (0001) surfaces after graphene formation in (a) 0.1 atm Ar (b) 0.5 atm Ar and (c) 1 atm Ar. All STM images are obtained at tip bias voltage  $V_b=0.1$  V, tunneling current  $I_t=0.1$  nA.

### 3.2.3 Graphene growth on wide terraces

A vicinal SiC (0001) substrate was annealed twice in 1 atm Ar; firstly 3 h at 1400°C for step bunching and then 1 h at 1550°C for graphene growth. Graphene formed surface is investigated by *in situ* SEM and STM, and *ex situ* AFM.

Figure 3.7(a) shows an SEM image of graphene grown on 4- $\mu\text{m}$ -wide terraces by annealing at 1550°C for 60 min. Dark bands shown by white arrows are step bunches, where multilayer graphene is formed. As shown in Figure 3.7(b), large gray regions on the terraces are monolayer graphene. Striped buffer layers remained on the terraces with bright contrast. Figure 3.8(a) shows a high resolution STM image of monolayer graphene region. This image is scanned with  $2048 \times 2048$  pixels over an area of  $800 \times 800 \text{ nm}^2$ , in which a clear moiré pattern, as shown in Figure 3.8(b), is observed in the entire region. The moiré pattern does not show a perfect hexagonal lattice, which is because of a sample draft and conditions of STM probe tip during the 20-hours scanning. Besides, several bright spots can be found in this area (indicated by white arrows in Figure 3.8(c)).

After the *in situ* observations, the surface morphology of the same sample was also investigated by AFM. Because of the temperature distribution during the resistive heating, surfaces annealed at various temperatures were observed on one sample. Figures 3.9(a) and (b) show AFM height and phase images, respectively, of a low temperature annealed region, indicating graphene formed only from step bunches with its width of about 500 nm. Figure 3.9(c) shows a height profile along a line A to B in Figure 3.9(a), revealing that the height change from surface buffer layer to monolayer graphene is about 1.2 nm, corresponding to a height change by erosion of 6 SiC bilayers (1.5 nm) and formation of one-layer graphene (0.3 nm).

Figure 3.10(a) shows an AFM height image of a terrace where a monolayer graphene of about 2  $\mu\text{m}$  in width extending from the bunched step and a striped buffer

layer (downward arrows) are grown. As revealed by the height profile in Figure 3.10(b), the striped buffer layer is about 0.45 nm higher than the monolayer graphene areas, which is also different from the height of the surface buffer layer. This height (0.45 nm) suggests a height difference between 3 SiC bilayers (0.75 nm) and a one-layer graphene (0.3 nm), indicating that 3 bilayers of SiC are remained under the striped buffer layer. Moreover, Figure 3.10(c) shows a height profile of the step bunch region in Figure 3.10(a), where a height change of 0.45 nm on the terrace, corresponding to a height change by erosion of 3 SiC bilayers (0.75 nm) and formation of a new graphene layer (0.3 nm), reveals the formation of bilayer graphene near the step bunch.

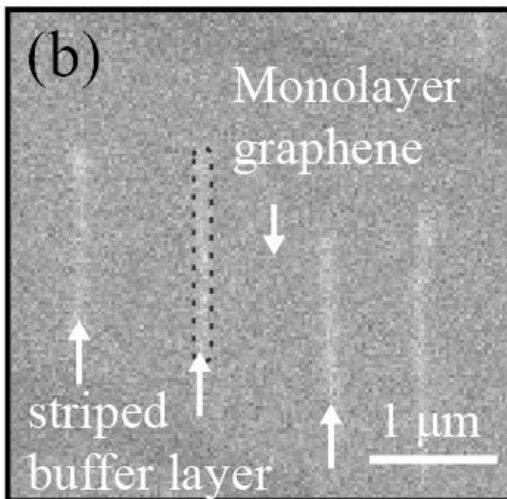
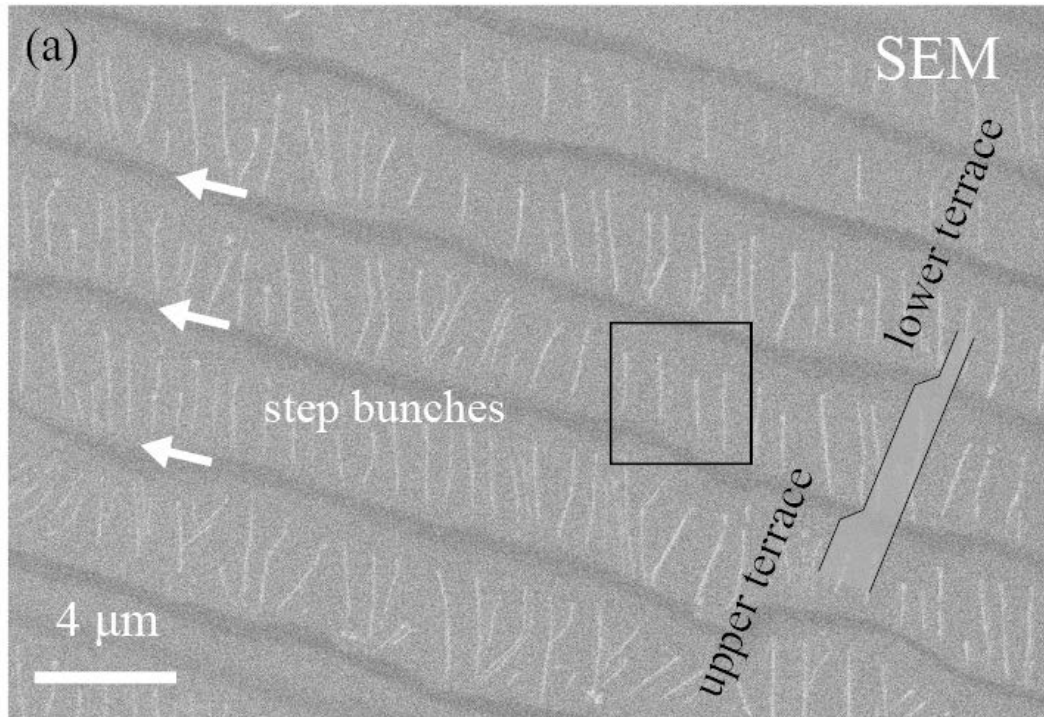


Figure 3.7: SEM images of graphene on a SiC (0001) substrate after annealed at 1550°C for 60 min; (b) zoomed image of a black frame in (a).

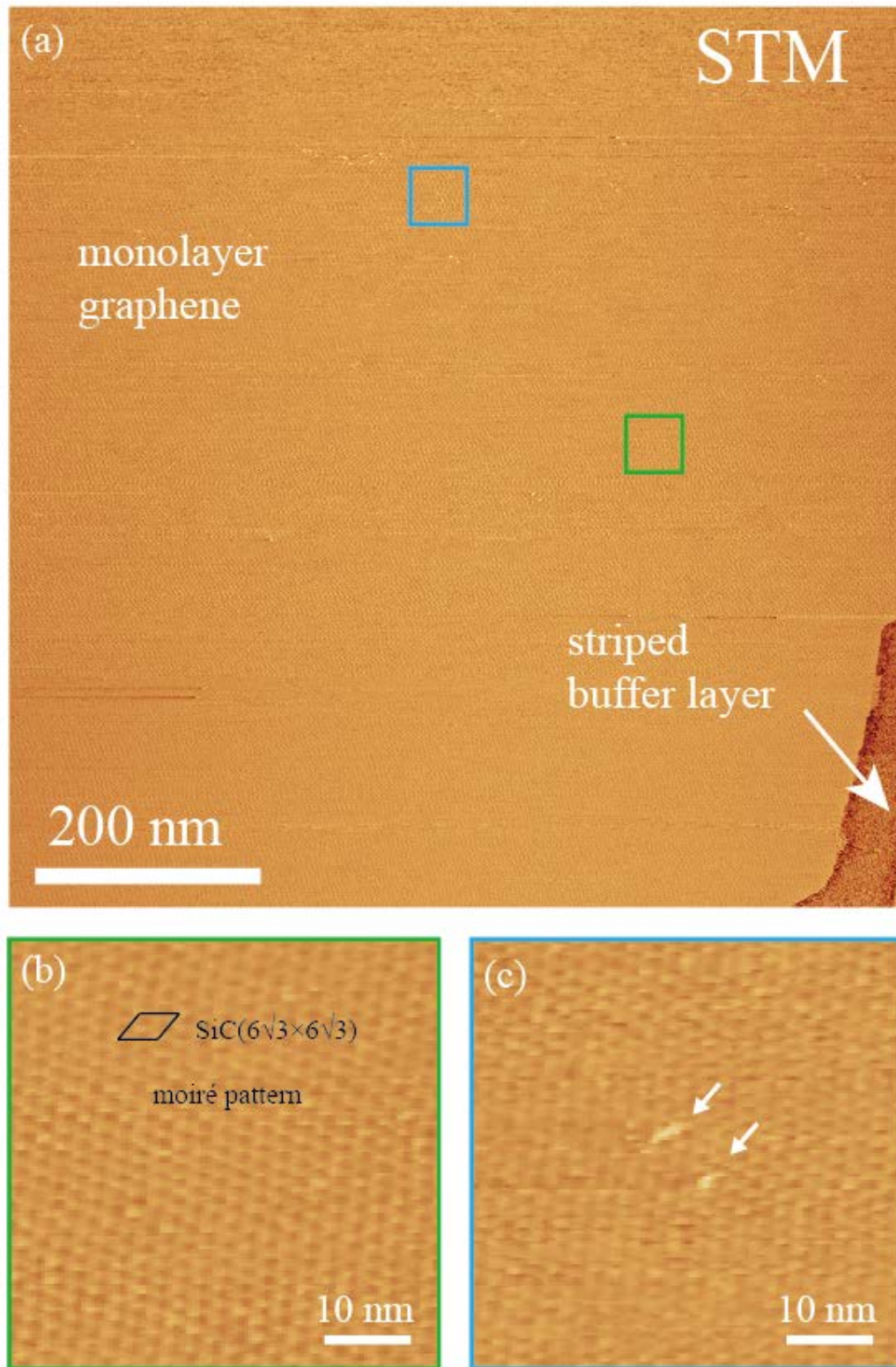


Figure 3.8: (a) STM image (800×800 nm, tip bias voltage  $V_b=0.1$  V, tunneling current  $I_t=0.1$  nA) of the same sample in Figure 3.7. (b) and (c) are enlarged images of monolayer graphene in (a).

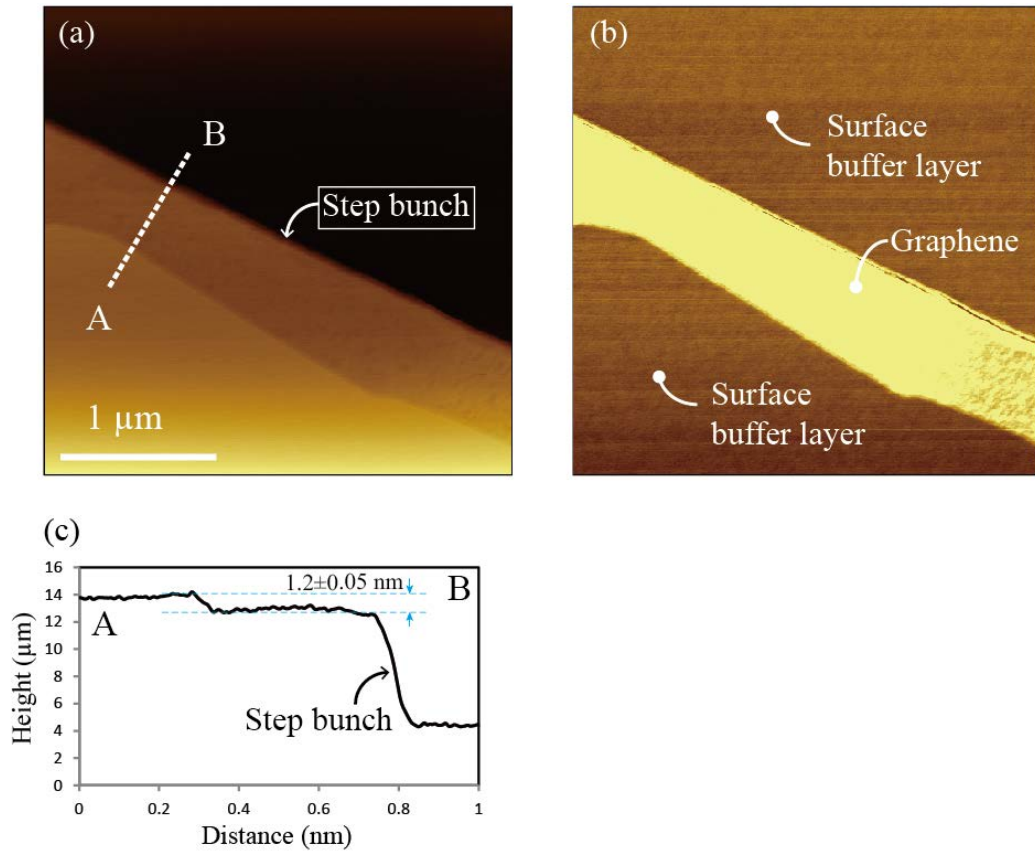


Figure 3.9: AFM (a) height and (b) phase images of monolayer graphene formed from a step bunch. (c) Profile of the dashed line A-B in (a).

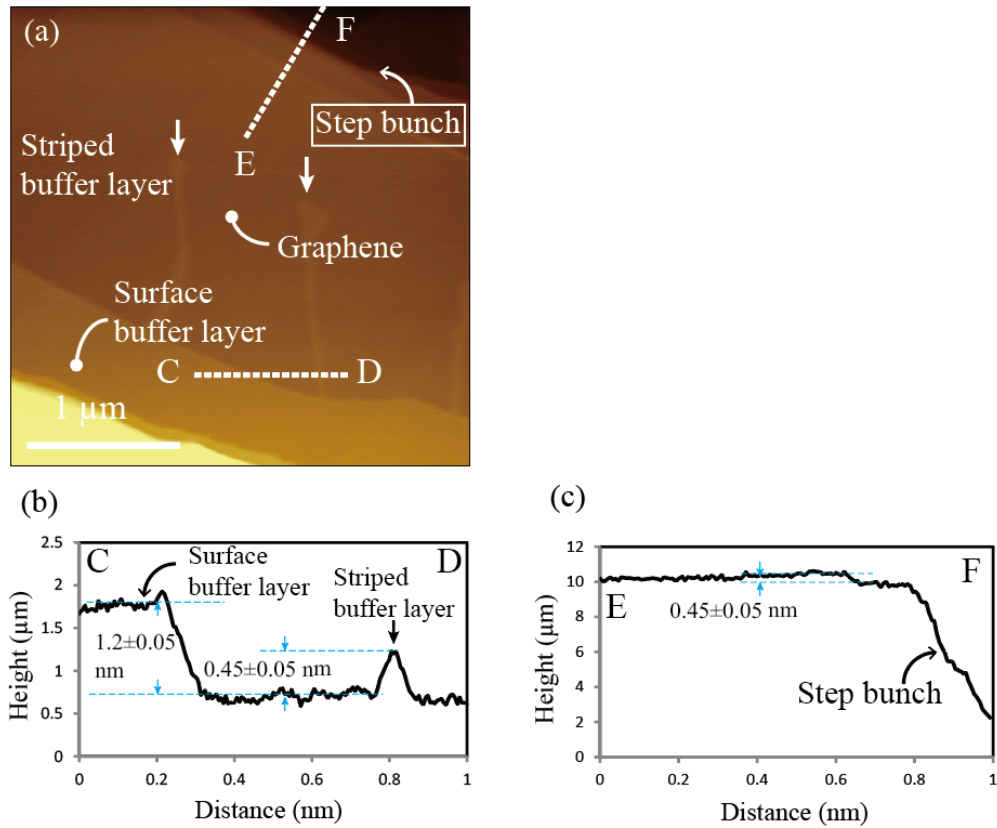


Figure 3.10: (a) AFM height image of monolayer graphene formed with striped buffer layer. (b) Profile of the dashed line C-D in (a). (c) Profile of the dashed line E-F in (a).

### 3.2.4 Observation of graphene growth processes on wide terraces

A patterned SiC (0001) substrate was annealed repeatedly at 1550°C for 15 min several times under 1 atm Ar for the graphene formation. After each annealing step, the same surface areas of the sample were recorded by *in situ* SEM.

#### Growth processes from step bunches

Figure 3.11 shows a series of SEM images of monolayer graphene growth from bunched steps indicated by black arrows. Black downward triangles show the same position of the substrate in the images. Graphene firstly formed uniformly over a width of 500 nm from the bunched steps after annealing for 30 min as shown in

Figure 3.11(a). By subsequent annealing, the striped morphology of a buffer layer started to form when graphene grew about 800 nm from the bunched steps (Figure 3.11(b)). When the growth front of graphene reached the next step (Figure 3.11(c)), the striped buffer layer shrank and disappeared (Figures 3.11(d) and (e)). As shown in Figure 3.11(e), although multilayer graphene grew at step bunches as well, its growth speed is much slower than the monolayer graphene growth on terraces.

### **Starfish-like graphene growth on terrace**

A new type of monolayer graphene nucleation with a starfish-shape was observed. Figure 3.12 shows a series of SEM images of a region where starfish-like monolayer graphene forms on a terrace. Before the appearance of the starfish-like nucleus, ordinary monolayer graphene growth from a step bunch is observed as shown in Figures 3.12(a) and (b). The starfish-like graphene nucleates on the terrace and extends branches after the annealing for 60 min as shown in Figure 3.12(c). Figure 3.12(f) is an enlarged view of the black frame in Figure 3.12(c). It can be seen that “arms” of the starfish points to a specific direction of  $\langle 10\bar{1}0 \rangle$  of the SiC substrate. By subsequent annealing, graphene grown from the starfish nucleus and that from step bunches contacted with each other, as shown in Figure 3.12(d). Being different from the case of graphene growth from step bunches, random-shaped buffer layer islands (Figure 3.12(e)) are left in the graphene areas grown from the starfish-like nuclei.

Figure 3.13 shows SEM and STM images of the same area of a sample after the graphene had covered the whole terrace. Two graphene areas can be distinguished in the SEM image; one is the area of graphene grown from the step bunches, and the other, the graphene area formed from the starfish-like nuclei. The former includes the striped buffer layer, and the latter includes the buffer layer islands with random shapes.

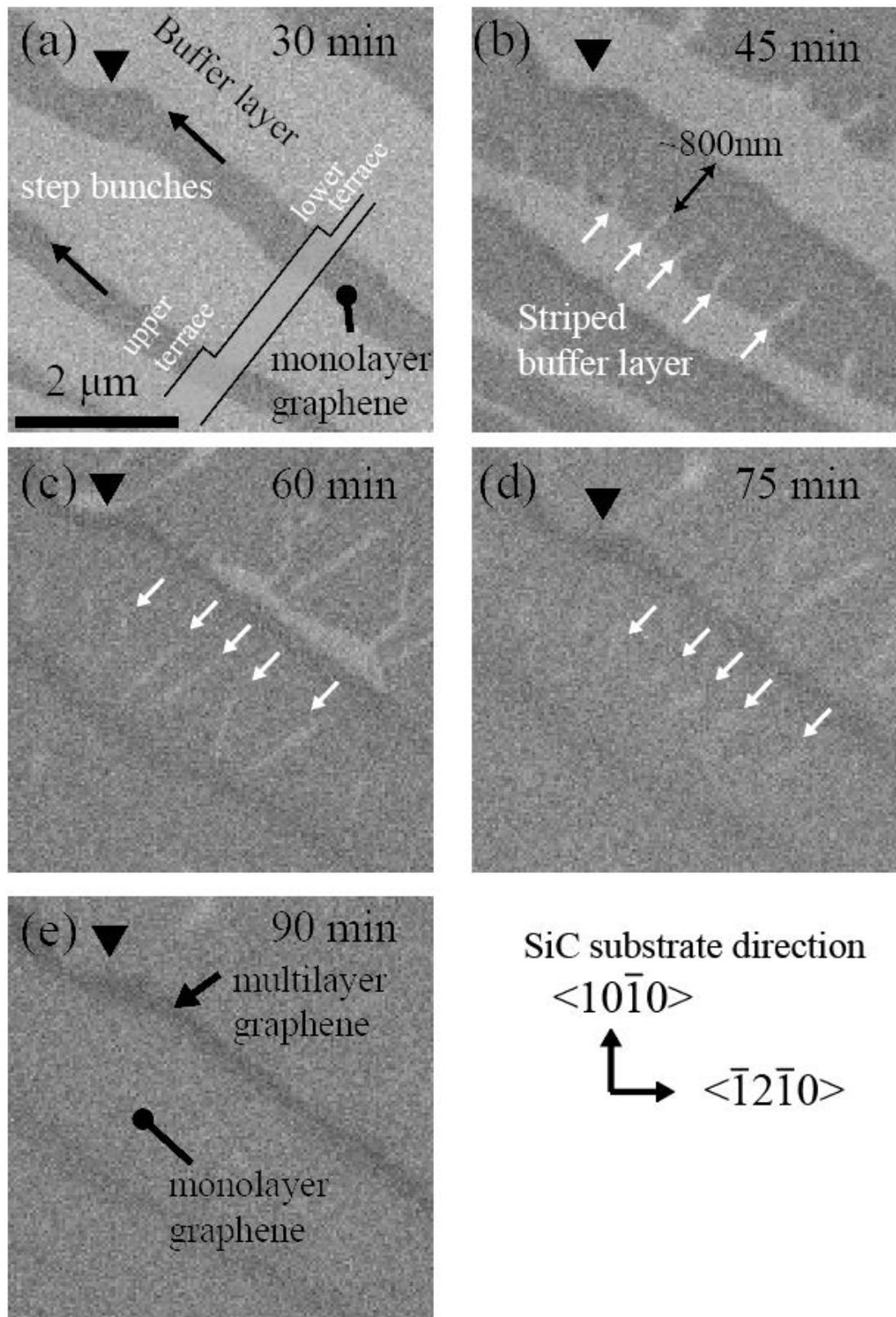


Figure 3.11: Series of SEM images of the same position of the surface during graphene formation from step bunches, with annealing time shown in each figure. Black downward triangles at upper left of the figures are position markers.

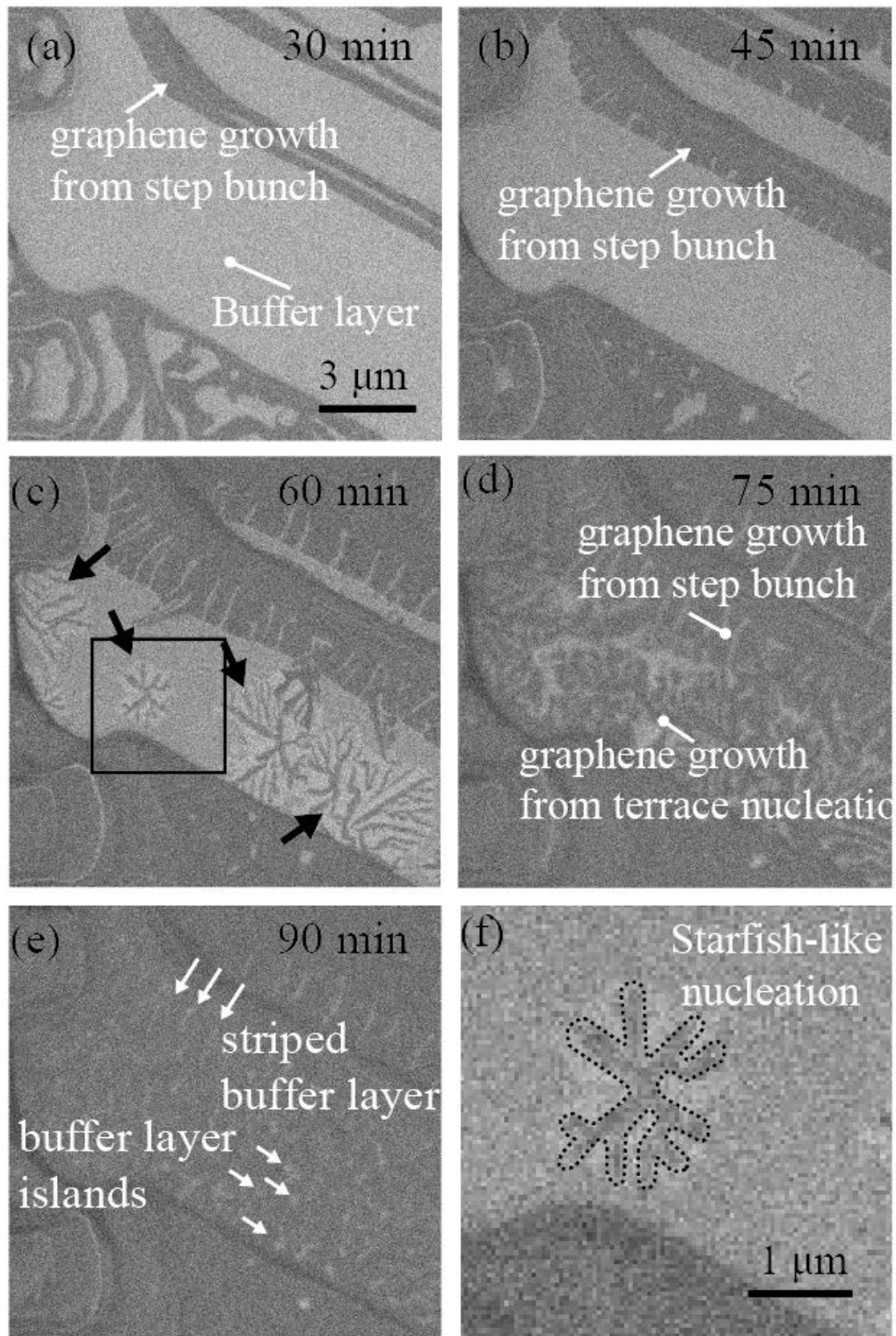


Figure 3.12: (a-e) Series of SEM images of starfish-like graphene nucleation on terraces after the sample annealed for 30 to 90 min; (f) enlarged view of a black frame in (c).

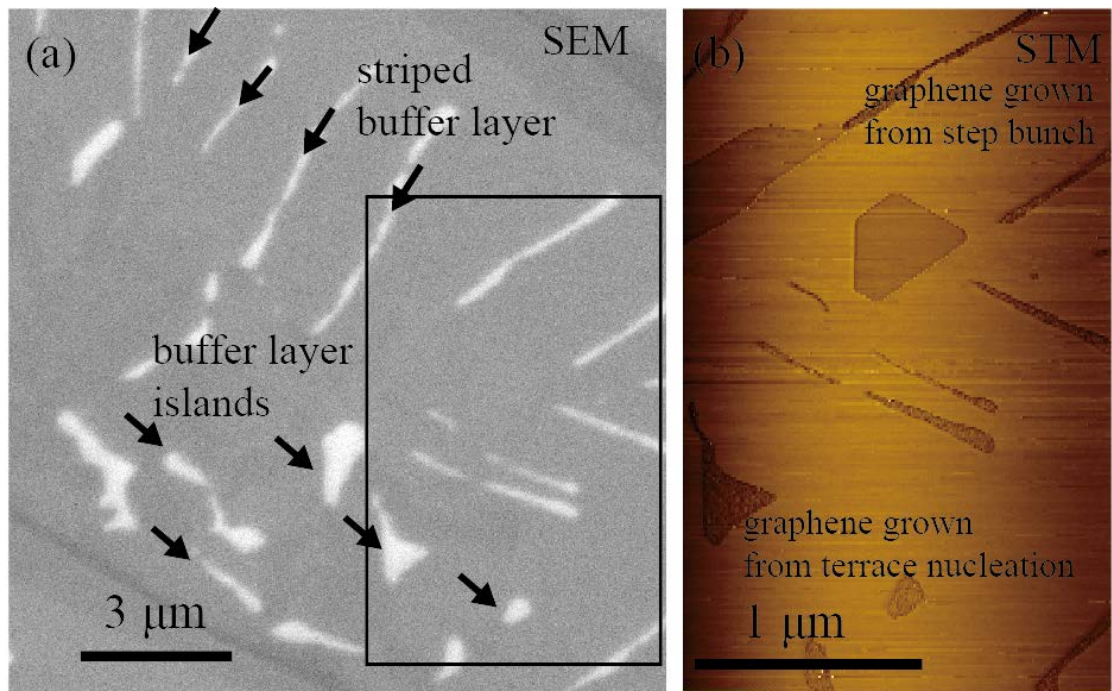


Figure 3.13: (a) SEM image and (b) STM image ( $V_b=0.1V$ ,  $I_t=0.1nA$ ) scanned over a black framed area of the sample with graphene formed after annealing for 90 min.

### 3.3 Discussions

#### 3.3.1 Graphene growth on step-free SiC surfaces

As introduced section 3.1, graphene nucleates at step edges and at pit edges on terraces. For an extreme situation, the graphene formation on step-free SiC (0001) substrates were investigated as shown in Figure 3.2. In Figures 3.2(a) and (b), as expected, a lot of pit formed on the step-free surface due to the rapid decomposition of SiC in UHV, and domain size of graphene is only about 100 nm. On the other hand, as shown in Figures 3.2(c) and (d), Ar atmosphere with a pressure of 1 atm suppresses the formation rate of pit during the annealing at 1600°C and thus graphene has a larger domain size of about 2 μm. However, as the result of pit expansion, pit edges appeared on the step-free surface, and multilayer graphene formed at the edges. In other words, the absence of step edges on step-free SiC surfaces results in that

graphene can only nucleates at pit edges with decomposition of SiC on terraces, as illustrated in Figure 3.14(a). Then, as shown in Figures 3.2(e) and (f), the prolonged annealing at the lower temperature (1550°C) in 1-atm Ar atmosphere promoted the reducing of pit formation and the large domain ( $\sim 10\ \mu\text{m}$ ) forming of graphene in the pits, as illustrated in Figure 3.14(b). Nevertheless, there remains a significant issue for the graphene formation on step-free SiC surface. That is the random nucleation of graphene in the pits on step-free surface, which makes such process uncontrollable and is inappropriate for device manufacturing. We suggest that creating step edges purposefully by patterning on the step-free SiC surface and subsequently growing graphene at low temperature in 1 atm Ar atmosphere may have an increasing chance for application of graphene on electric devices.

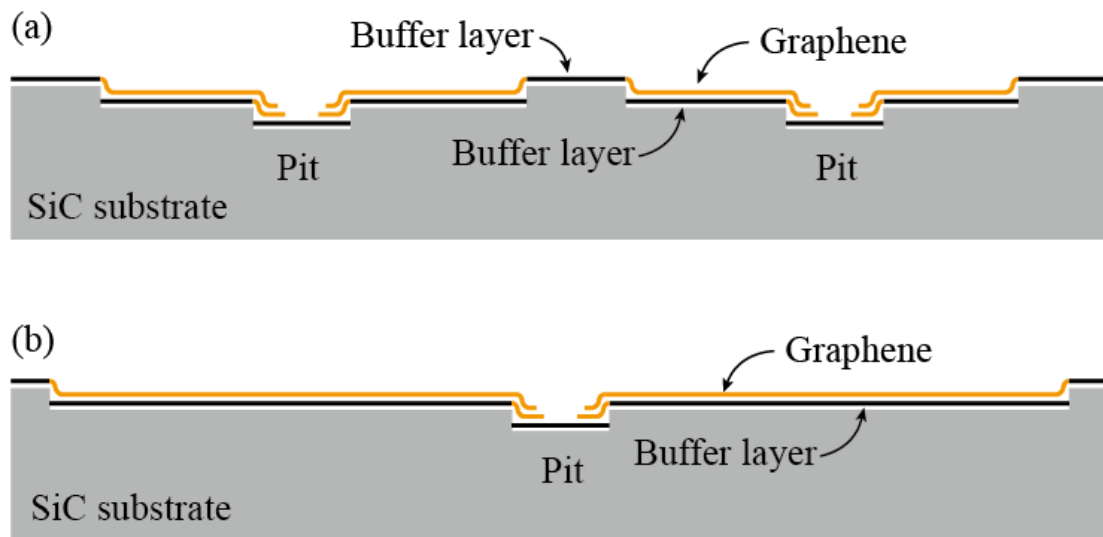


Figure 3.14: Schematic section view of graphene formation on step-free SiC surfaces at annealing condition of (a) higher temperature and short time, (b) lower temperature and long time.

### 3.3.2 Dependence of graphene formation on gas pressure and annealing temperature

Single crystalline SiC (0001) substrates are polished on-axis of [0001] with an inevitable miscut, which lead to the steps on surfaces. During the annealing processes, a broadening of the terraces is observed due to the effect of step bunching, as shown in Figure 3.3. Two kinds of step bunching were found to occur in this process, i.e., one is the bunching of less than one-unit cell and the other, over one-unit cell. This observation is also consentient with precious reports [52]. As observed in Figures 3.3 (a) and (b), due to the crystal structure of 6H-SiC, it is natural that steps firstly bunch to 3 and 6 bilayer steps to obtain the stable surfaces [53]. Step edges subsequently bunched to the height over one-unit cell (6 bilayers) of SiC, as observed in Figures 3.3 (e) and (f). This kind of bunching happens to obtain some thermodynamically stable facets of  $(11\bar{2}n)$  [54].

The increasing rate of terrace width is the highest at the annealing temperature of 1400°C both under 0.1 and 1 atm Ar, as shown in Figure 3.5. Considering the RHEED observation in Figure 3.4, several reasons can explain the slowing down of step-bunching rate during the stages of the annealing below and above 1400°C. For the case of 1300°C, the pattern of SiC ( $3 \times 3$ ) demonstrated a Si-rich super structure on SiC Si-face [48]. The Si-rich surface indicates the annealing temperature of 1300°C is still too low for the sublimation of decomposed Si and the low temperature reduces the decomposition rate of SiC. On the other hand, the buffer layer and graphene formed after annealing above 1400°C, which covered the SiC surface, can also suppress the sublimation of Si atoms. Therefore, the stoichiometric SiC surface, i.e. a bare SiC surface without any super structure and adsorbate, is achieved at 1400°C, which facilitates the sublimation of Si, leading the enhanced step-bunching.

Although Ar pressure had no effect on step-bunching process, it played a

significant role for suppressing the formation of pits, as is observed in the STM images of graphene surfaces formed under different Ar pressures (Figure 3.6). The density of pits (white arrows) as a function of Ar pressure is shown in Figure 3.15, revealing the pit density decreases dramatically with increasing the Ar pressure in the range of 0.1-1 atm.

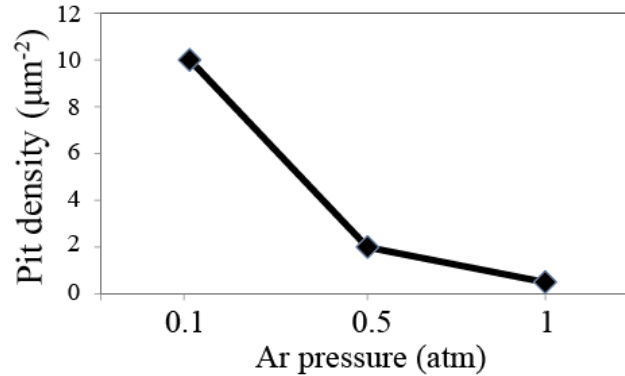


Figure 3.15: Ar pressure dependence of the densities of pits formed after graphene formation on SiC (0001).

### 3.3.3 Graphene growth on wide terraces

#### Growth of monolayer graphene on wide terraces

The discussion in section 3.3.2 suggests that wide terraces (over 4-μm on width) can be grown by step-bunching process at 1400°C before the formation of graphene layers. However, similar to the step-free SiC samples, the lack of step edges on a wide-terrace surface still leads to the formation of pits on terraces during graphene formation at high temperature (over 1600°C) in Ar pressure of 1 atm, as Figure 3.16(a) illustrates the case. Hence, the prolonged annealing at lower temperature (1550°C) is also carried out for graphene growth on wide terraces, where monolayer graphene consequently covered more than 90% area of the SiC surface, as revealed by the SEM image in Figure 3.7. The buffer layer with striped morphology remained in monolayer graphene areas, also known as the striped buffer layer [55], is a typical feature of monolayer graphene grown only from step edges.

### Single crystalline monolayer graphene on a wide terrace

As shown in Figure 3.8, the STM image of monolayer graphene areas reveals the presence of bright spots, which indicate to different electronic states due to vacancy defects. Such defect is commonly found for epitaxial graphene on SiC [56], but no domain boundary is detected in the present study. Since the regions of monolayer graphene in other STM images also showed the same feature (no grain boundary), we consider that monolayer graphene grown from step bunches forms as one domain. Such being the case, the annealing at 1550°C makes graphene nucleate only at the step bunches and slowly grow toward the other side of a terrace avoiding the pit formation, as illustrated in Figure 3.16(b). Moreover, the wide terraces with monolayer graphene extended over 100- $\mu\text{m}$ -scale, which means the single crystalline monolayer graphene with its size more than  $4 \times 100 \mu\text{m}$  is formed on the surface.

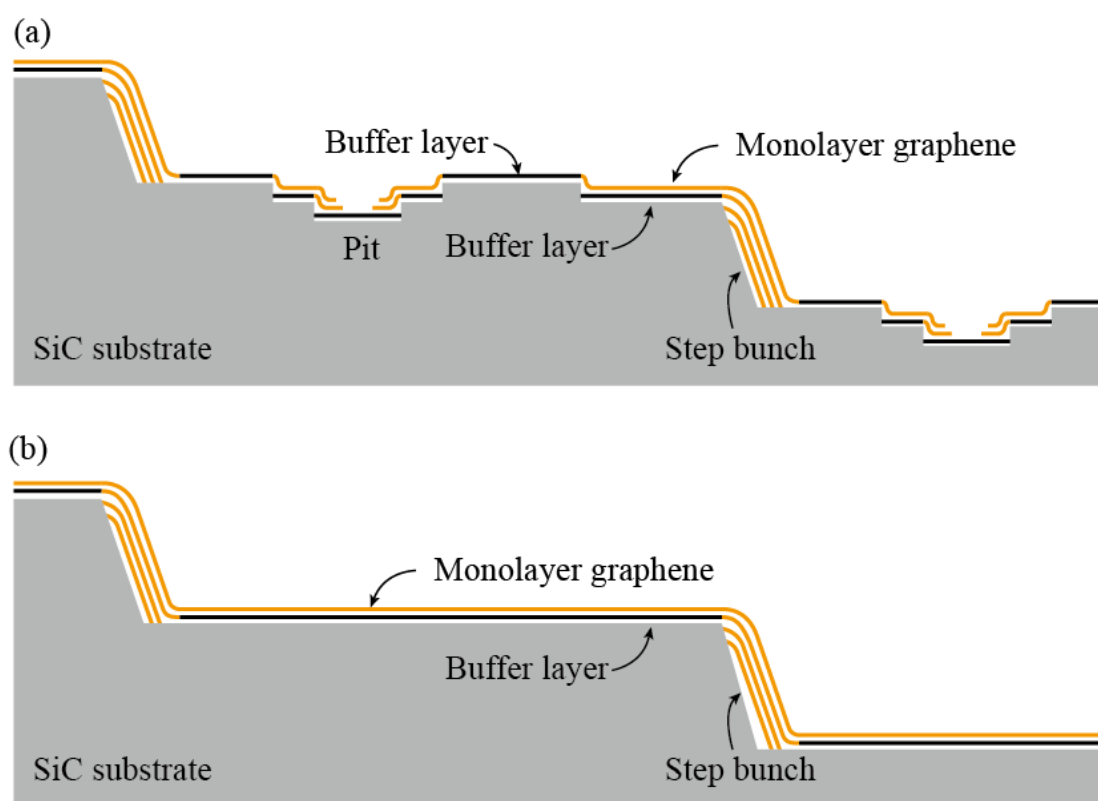


Figure 3.16: Schematic section view of graphene formation on vicinal SiC surfaces at annealing condition of (a) higher temperature and short time, (b) lower temperature and long time.

### **Origin of height difference of 1.2 nm and 0.45 nm on a terrace covered with graphene/buffer layer**

It has been commonly known that, for the case of graphene growth on 6H-SiC, carbon atoms included in one-layer graphene are supplied by the decomposition of 3-bilayer-SiC (0001) [25, 57-59]. Actually, there still has no direct evidence about how much SiC was eroded to form the first graphene layer from a bunched step. As it observed in Figure 3.9(c), the 1.2-nm height difference indicates a step between 6 bilayers of SiC and one-layer graphene as shown by a schematic sketch in Figure 3.17(a) (a section structure in the dashed frame in the right profile). In other words, 6-bilayer is decomposed for the growing of the first graphene layer from the step bunch, which has not been reported in any previous studies. It is still reasonable that 6 bilayers of SiC are firstly eroded instead of a 3-bilayer from a bunched step edge to obtain the more stable SiC structure, because in the case of 6H-SiC, 6-bilayers are contained in a unit cell [53].

We found that the height of striped buffer layer is lower than that of surface buffer layer, as shown in Figure 3.10(b). Figure 3.17(b) show the section structure of the striped buffer layer, the formation mechanism of which will be discussed in the next section. We also observed the growth of bilayer graphene near the step bunch (Figure 3.10(c)). As shown by the section structure (Figure 3.17(c)) at the boundary between monolayer and bilayer graphene region, it is probable that the decomposition of SiC is greatly suppressed under the 2 carbon layers (first graphene layer and underneath buffer layer); only 3-bilayer of SiC is eroded to form the new buffer layer, such that the second-layer graphene grow much slower than monolayer graphene grows.

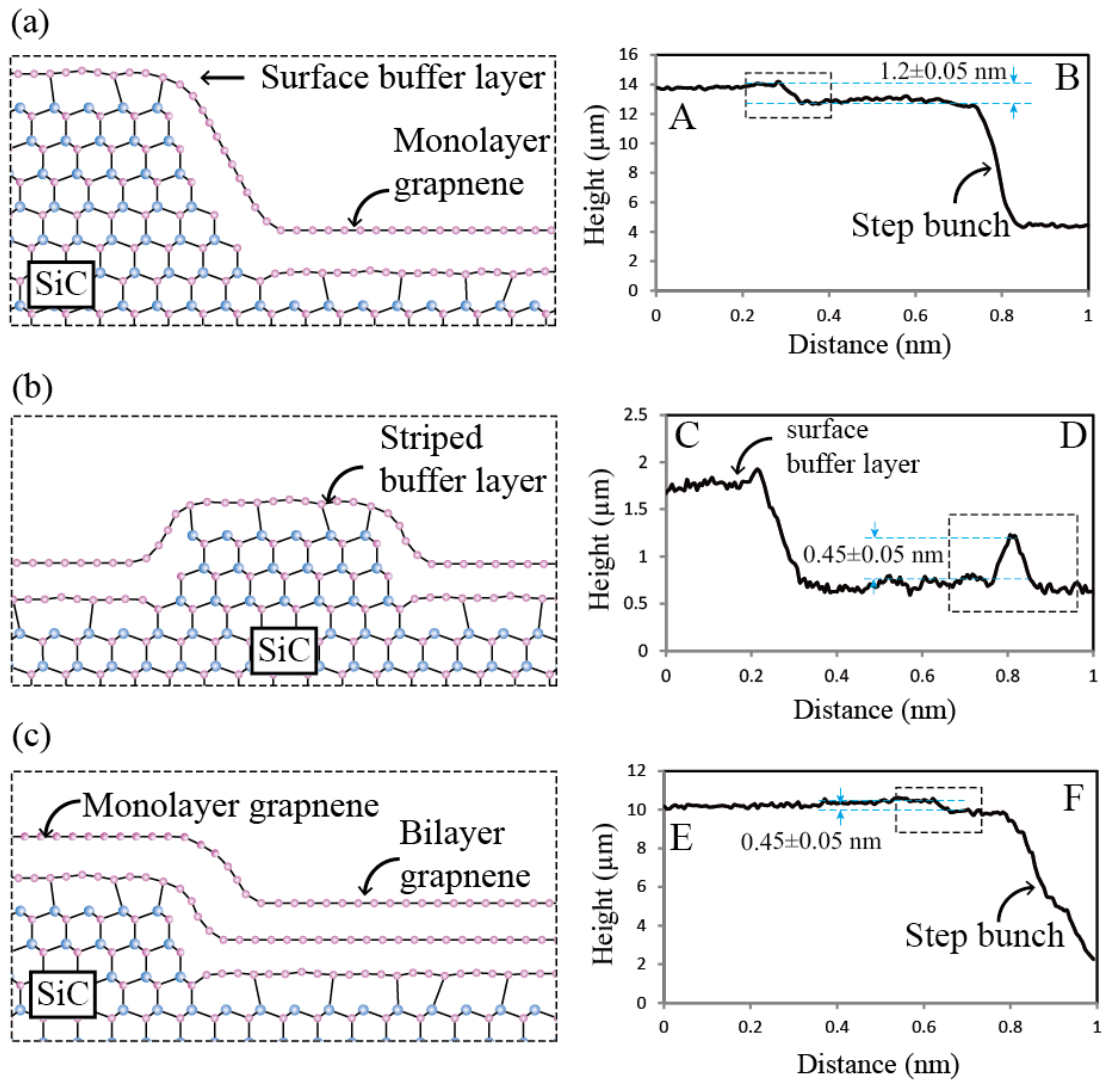


Figure 3.17: Schematic sketches of the section structure in the dashed frame in right profiles (from Figures 3.9 and 3.10) of (a) surface buffer layer/monolayer graphene, (b) striped buffer layer and (c) monolayer graphene/bilayer graphene.

### 3.3.4 Graphene growth mechanisms from step bunches

We had fabricated monolayer graphene uniformly from the step bunches on 4- $\mu\text{m}$  terraces, as described in section 3.3.3. The striped buffer layer remained in graphene domains after monolayer graphene covered the whole terraces. Borovikov *et al.* discussed the formation of striped buffer layers after the graphene growth under a background Si pressure [55]. They explained such phenomenon by using a curvature

driven mechanism for step edge stability, i.e., the decomposition rate in concave regions is higher than that in convex regions. However, such explanation is only a speculation from an observation of the surface morphology after the graphene growth finished. In order to make clear how monolayer graphene grows from the step bunches on wide terraces and why such a striped buffer layer forms during graphene growth, we investigated the whole processes of the graphene growth on the wide terraces as shown in Figure 3.11.

According to the explanation by Borovikov *et al.* [55], the striped buffer layer should form randomly from a step edge at the beginning of graphene growth. However, our observation showed that the monolayer graphene firstly grew uniformly over a width of 800 nm from the step bunches, and then the striped buffer layer started to form with the height level different from the surface buffer layer (discussed in section 3.3.3), which cannot be explain by their mechanism. In our case, we consider that such striped buffer layer played a role as pathways of decomposed Si and C atoms during the graphene growth on terraces, as illustrated in Figure 3.18. It is believed that a monolayer graphene is formed by a transformation from the surface buffer layer when a new buffer layer grows by decomposing 6 bilayers of SiC underneath. Because only the C atoms in 3-layer SiC is going to form the new buffer layer, decomposed Si atoms and the rest of the C atoms at the front of new buffer layer must diffuse between the monolayer graphene and the new buffer layer toward the step bunches. At the first stage, graphene grows near the step bunches and the decomposed atoms can easily arrive at step bunches as shown in Figures 3.18(a) (b) and (k). This stage corresponds to the SEM image after 30 min of the annealing (Figure 3.11(a)). Figure 3.18(b) shows the density distribution (shown by color density) and diffusion path (white arrows) of decomposed atoms giving that such uniform diffusion results in the uniform graphene growth at the first stage. The maximum width of uniform graphene band adjacent to the step bunches (i.e. 800 nm for this annealing condition) is considered to correspond to a diffusion length of the decomposed atoms. At the second stage, graphene starts to grow beyond the diffusion

length of decomposed atoms (the stage shown in Figures 3.18(c) and (d)), and the atoms near the decomposed location are unable to diffuse to the step bunches directly, so that they may move along the boundary between buffer layer and graphene to somewhere appropriate for the diffusion to the step bunch. As a result of that, a striped buffer layer begins to form at positions in a distance between the step bunch (800 nm for this annealing condition), where Si atoms are able to diffuse towards the step bunch (Figures 3.18(e) and (f)). With the progress of graphene growth, the diffusion of decomposed atoms occurs through a gap along the graphene-buffer boundary as a pathway to the step bunch (Figures 3.18(g) (h) and (l)), corresponding to the SEM image after 45 min of the annealing (Figure 3.11(b)). During graphene growth toward the end of the terrace, decomposition of SiC under the striped buffer layer is suppressed by the supply of passing Si and C atoms, leaving the striped buffer layer even after the graphene covered over the whole terraces. Finally, the striped buffer layer became narrow and disappeared from the back region (upper side) of a terrace as shown in Figures 3.18(i) and (j), corresponding to the SEM image after 75 min of the annealing (Figures 3.11(c) and (d)).

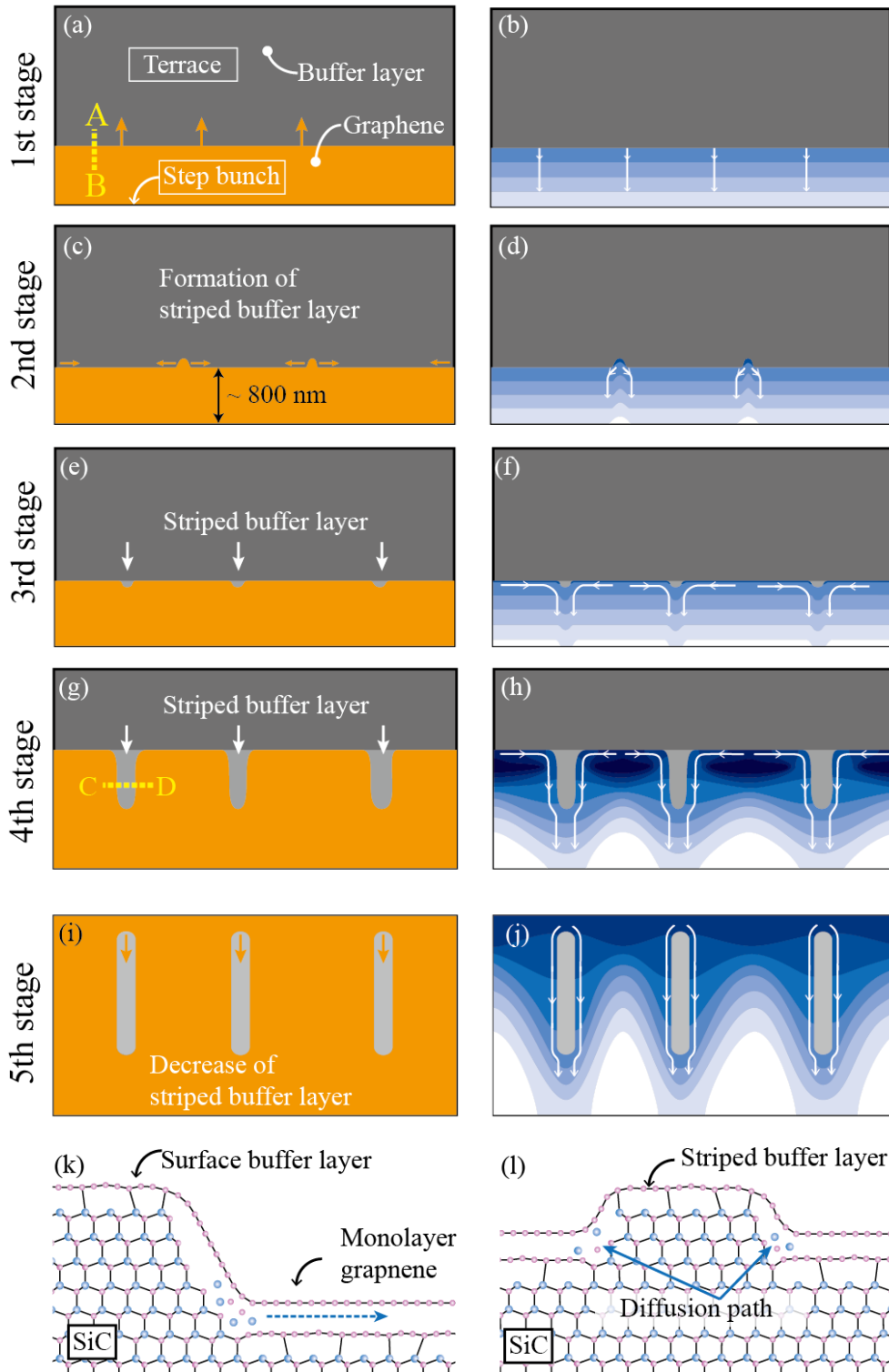


Figure 3.18: (a-j) Sketch diagrams of morphology change (left column) and decomposed atom density distributions (right column) during the graphene growth from a step bunch. In the right diagrams, the change in density of blue color demonstrates the atoms density distributions and white arrowed lines demonstrate the diffusion paths. (k) Section structure of the dashed line in (a). (l) Section structure of the dashed line in (g).

### 3.3.5 Starfish-like graphene nucleation on terraces

We have observed a new type of starfish-like nucleation of monolayer graphene on the terraces, as presented in Figure 3.12. Notably, no pit is formed on the terrace in the present case (Figure 3.13(a)), which clearly differs from the previously reported graphene growth on a terrace by forming pits (Figure 3.1). It should also be noted that two regions of graphene, i.e. the graphene grown from the step bunches with strip buffer layer and the graphene formed from starfish-like nuclei on terraces with random-shaped buffer layer islands, are observed after graphene formation. However, no domain boundary is observed between these two graphene regions in STM image (Figure 3.13(b)), suggesting that graphene areas grown on the terrace and from the step bunch coalesce as one domain without pit formation.

It is considered that the starfish-like graphene is formed due to sublimation of decomposed Si atoms from a defect. Figure 3.19 shows the comparison between the graphene formation in pits and from defects. As shown in Figure 3.19(a), graphene in a pit, which usually has trigonal or hexagonal shape, includes a buffer layer region in its center. The rapid decomposition of SiC breaks the surface buffer layer and deepens the pits as illustrated in Figure 3.19(b). As shown in Figure 3.8, monolayer graphene (used to be the surface buffer layer) has a certain amount of defects. Because of the low temperature graphene growth, Si atoms diffuse so gently toward a defect for sublimation in our case (Figures 3.19(c) and (d)) that the monolayer graphene could nucleate and grow on the terraces without forming pits. This process of monolayer graphene growth is significant for the large domain graphene growth on completely pit-free SiC surfaces.

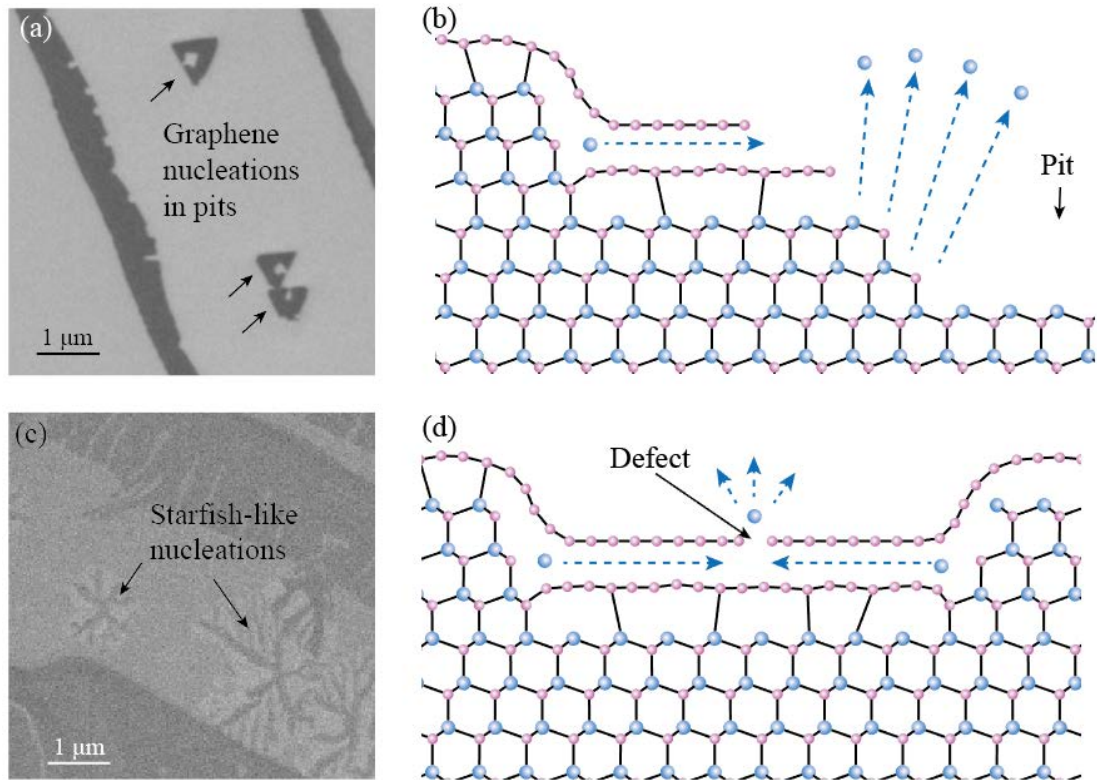


Figure 3.19: (a) SEM image of graphene formed in pits. (b) Schematic of section structure of a graphene nucleation in a pit. (c) SEM image of graphene formed from a defect. (d) Schematic of section structure of a starfish-like nucleation.

### 3.4 Summary

In this chapter, the graphene growth by thermal decomposition of SiC was studied by using an *in situ* the UHV-SEM/STM system at various annealing conditions, e.g., gas pressure, annealing temperature and SiC surface morphology.

A low temperature graphene growth was carried out on the step-free SiC substrate. As a result, graphene with domain size of about 10 μm was formed in the pit. However, due to the uncontrollability of pit formation, it was found that the step-free substrate is not suitable for graphene growth control.

By investigating the annealing processes of vicinal SiC substrates, growth of

terraces due to the step bunching was observed, which occurred before the formation of buffer layer on SiC surfaces. It was found that the rate of terrace widening at the temperature of about 1400°C was the highest. Also, Ar pressure did not show any significant effect on this process, but played an important role for suppressing the formation of pits during graphene growth.

Hence, as a pretreatment for graphene growth, annealing at 1400°C for 3 hours was firstly carried out to enlarge the terrace widths. Subsequently, by heating at relatively low temperature (1550°C) for 1 hour, monolayer graphene could be started to grow from the step bunches and was extended over wide terraces without pit formation. As the result, pit-free single crystalline monolayer graphene was fabricated with the size of  $4 \times 100 \mu\text{m}$ . The AFM images suggested that the first graphene layer was formed by decomposition of 6-bilayer SiC from the step bunch, while the second graphene layer was formed by decomposition of 3-bilayer SiC and grew much slower than the first layer.

We also succeeded in recording the morphology changes of a SiC surface during the graphene growth at the same location on a wide terrace by *in situ* SEM. According to the observation, the formation of striped buffer layer is considered to be a result of the diffusion of decomposed atoms through a narrow space between a monolayer graphene and a newly formed buffer layer. Moreover, a new type of starfish-like graphene nucleation was observed on the terraces. The two graphene regions grown from step bunches and from starfish nuclei are finally connected to form a larger domain of graphene covering the wide terraces without pit formation.

# Chapter 4 Etching of Epitaxial Graphene with Oxygen

## 4.1 Introduction

Reactions with active gasses, such as hydrogen and oxygen, are important approaches to modify the graphene formed on SiC (0001) surfaces. It has been already reported that hydrogen intercalation can be used for decoupling the buffer layer from the SiC (0001) substrate [60-62]. As shown in Figure 4.1 [60], by an annealing in hydrogen atmosphere above 600°C, instead of the C atoms in buffer layer hydrogen atoms bond to the Si atoms of SiC surface. As a result of that, buffer layer and monolayer graphene surface transform to quasi-free-standing monolayer graphene and bilayer graphene respectively. LEED observations (Figures 4.1(e) and (f)) have indicated the decouple of buffer layer by the hydrogen intercalation.

A similar phenomenon by using oxygen treatments has also been well studied, which can transform a buffer layer to a monolayer graphene by forming an oxide layer under the buffer layer [63-66]. Oida et al. [63] have reported that a low-temperature annealing in an oxygen (O<sub>2</sub>) atmosphere (1 atm, 250°C, 5 s) turns the buffer layer to a monolayer graphene by forming a thin oxide layer (thickness of 0.3 nm) underneath the buffer layer. Following these studies, some other groups found that water vapor or air can also be used as oxygen source for the intercalation. Ostler et al. [64] reported that annealing in a water vapor atmosphere (~28 mbar) resulted in a formation of monolayer graphene from a surface buffer layer surfaces (500°C, 30 min) and a bilayer graphene from a monolayer graphene surfaces (650°C, 30 min). Oliveira et al. [65] investigated the oxygen intercalation to monolayer graphene surfaces by the annealing in air (600°C, 40 min) and fabricated a decoupled bilayer graphene on SiC surfaces. Recently, they also fabricated quasi-free-standing bilayer graphene nanoribbons (about 300 nm in width) by annealing a SiC substrate with

monolayer graphene nanoribbons formed near step edges under the same condition (air, 600°C, 40 min) [66]. They also found that the surface buffer layers on terraces were etched after the annealing in air, as shown in Figure 4.2 [66]. They explained the etching of surface buffer layer by the presence of C atoms with  $sp^2$ -to- $sp^3$  rehybridization that enhances the chemical reactivity of the buffer layer [66, 67].

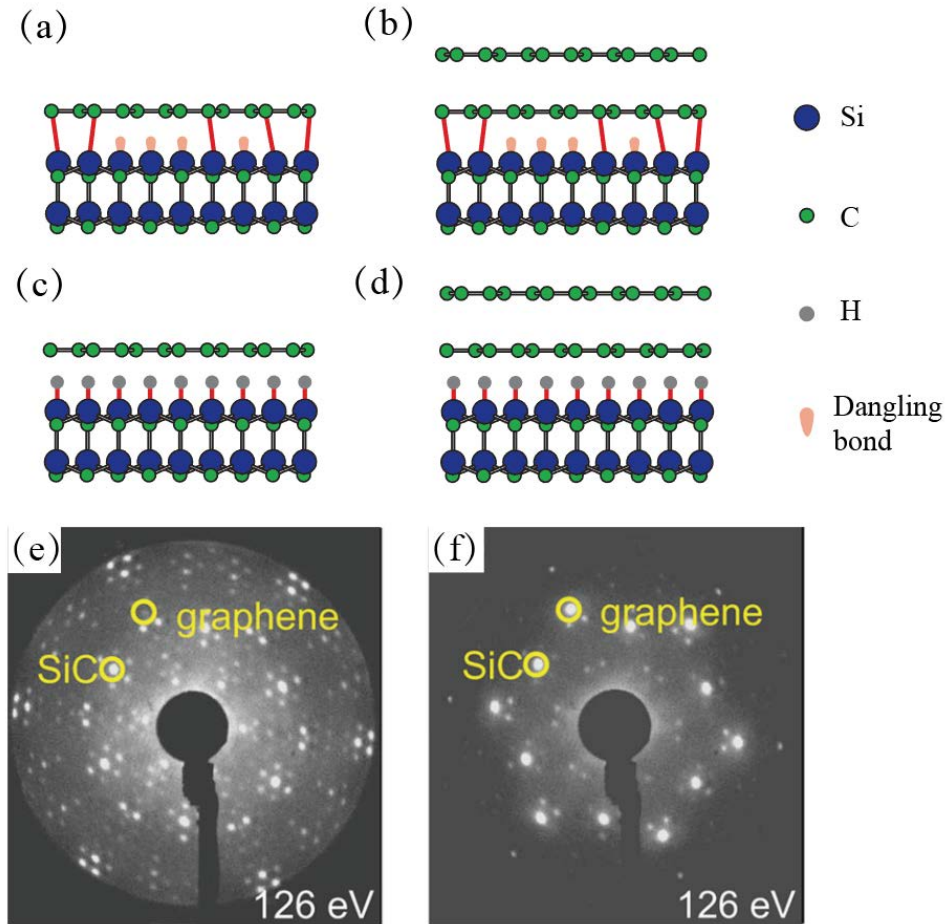


Figure 4.1: Schematic diagrams of section atomic structure of (a) surface buffer layer and (b) monolayer graphene before the hydrogen intercalation. (c) and (d) section atomic structure of (a) and (b) after the hydrogen intercalation. (e) and (f) LEED patterns of buffer layer surface before and after the hydrogen intercalation [60].

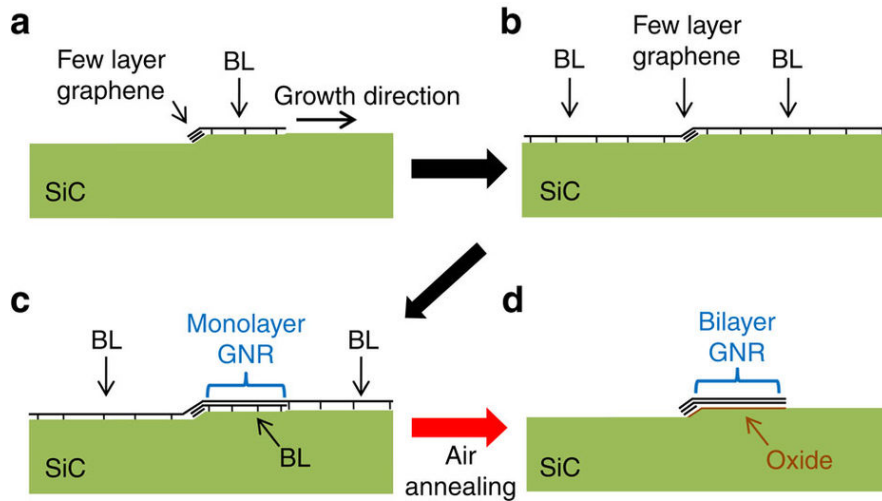


Figure 4.2: Schematic section diagrams of (a-c) monolayer graphene nanoribbon and (d) bilayer graphene nanoribbon after the air annealing [66].

Thus, Oliveira et al. have selectively etched the surface buffer layer during the fabrication of bilayer graphene nanoribbons by the annealing in air. In this study, we try to etch a surface buffer layers on a wide terrace but not to decouple a buffer layer underneath a monolayer graphene by using an extreme low partial pressure of oxygen as illustrated in Figure 4.3. The selective etching also results in a formation of free-edge monolayer graphene without the connection to surface buffer layers. The free-edge structure is more meaningful for the case of monolayer graphene nanoribbons, which will be discussed in the next chapter.

As explained in section 1.3, the surface buffer layer is a precursor for monolayer graphene, so that its quality (crystallinity) is crucial for graphene growth. However, there is just few report focusing on the quality of surface buffer layer [68, 69], and thus more investigation of the surface buffer layer is necessary. Such that, we investigate the etching processes of a surface buffer layer to clarify the crystallinity of surface buffer layers.

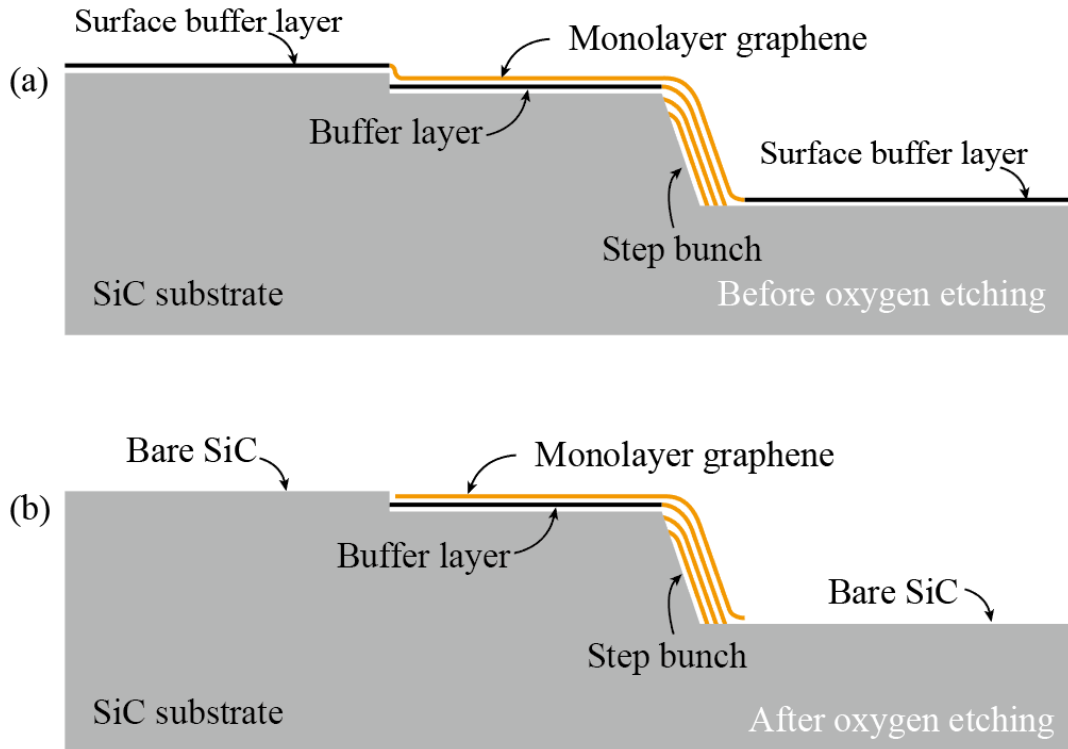


Figure 4.3: Schematic cross sections of SiC (0001) substrates with graphene on their surfaces (a) before and (b) after the selective oxygen etching.

## 4.2 Experimental and results

### 4.2.1 Sample preparation and characterizations

The vicinal SiC (0001) substrates were patterned with markers on their surfaces by laser lithography and RIE, so that we can identify different positions on the surface of samples after various etching stages. Before the annealing processes, SiC substrates were cleaned in acetone by an ultra-sonic cleaner for 30 min to remove surface impurity. After an introduction of samples to the preparation chamber, a hydrogen etching (0.1-atm-hydrogen at 1300°C for 15 min) was first carried out for surface cleaning. Then, graphene was fabricated by annealing at 1550°C for 1 hour in a 1-atm-Ar atmosphere. The selective oxygen etching was carried out in a mixed atmosphere of O<sub>2</sub> ( $\sim 10^{-3}$  Pa) and Ar (1 atm) at 1300°C for 15 min, and changes of the surface structures were investigated by the *in situ* RHEED, SEM and STM. An *ex situ*

micro-probe Raman spectroscopy was also carried out for graphene and buffer layer evaluation before and after the selective oxygen etching. To avoid adverse influences of adsorbates such as oxygen and water after the exposure to air during the Raman measurement, the graphene/SiC samples after the Raman measurement in air was not used for the subsequent etching processes.

## 4.2.2 Results of selective oxygen etching

Figure 4.4(a) shows an SEM image of SiC (0001) surface after the oxygen etching for 15 min, where monolayer graphene layers extends about 2  $\mu\text{m}$  in width from the step bunches (white v-shaped arrows), and a triangle of graphene in a pit is found on a terrace. The striped morphology indicated by black arrows is the typical feature of monolayer graphene with striped buffer layers formed on SiC substrates, and the formation mechanism of the stripes was discussed in section 3.3.4. A Raman mapping of graphene-2D peak intensity in the same area of Figure 4.4(a) is shown in Figure 4.4(b). The mapping image well corresponds to the SEM image, indicating that the graphene remains along the step bunches and in the pit after the oxygen etching. The Raman spectra before and after the etching are shown in Figure 4.5, which are taken from the surface buffer layer areas on the terraces before (red) and after (blue) the oxygen etching. Raman signals from the bare SiC substrates have been subtracted from all the spectra. Broad peaks (downward triangles) around 1350  $\text{cm}^{-1}$ , 1490  $\text{cm}^{-1}$  and 1580  $\text{cm}^{-1}$  in the spectrum before the oxygen etching indicate the presence of a buffer layer [69]. After the etching these signals are absent in the spectrum, which means that the surface buffer layer is removed and the bare SiC surface appeared. Raman spectra obtained from the monolayer graphene region near the step bunches before (red) and after (blue) the oxygen etching are shown in Figure 4.6. The typical graphene peaks (G:  $\sim 1580 \text{ cm}^{-1}$ ; 2D:  $\sim 2700 \text{ cm}^{-1}$ ) and buffer layer peaks are observed in both spectra, which indicates that the monolayer graphene remained after the oxygen etching.

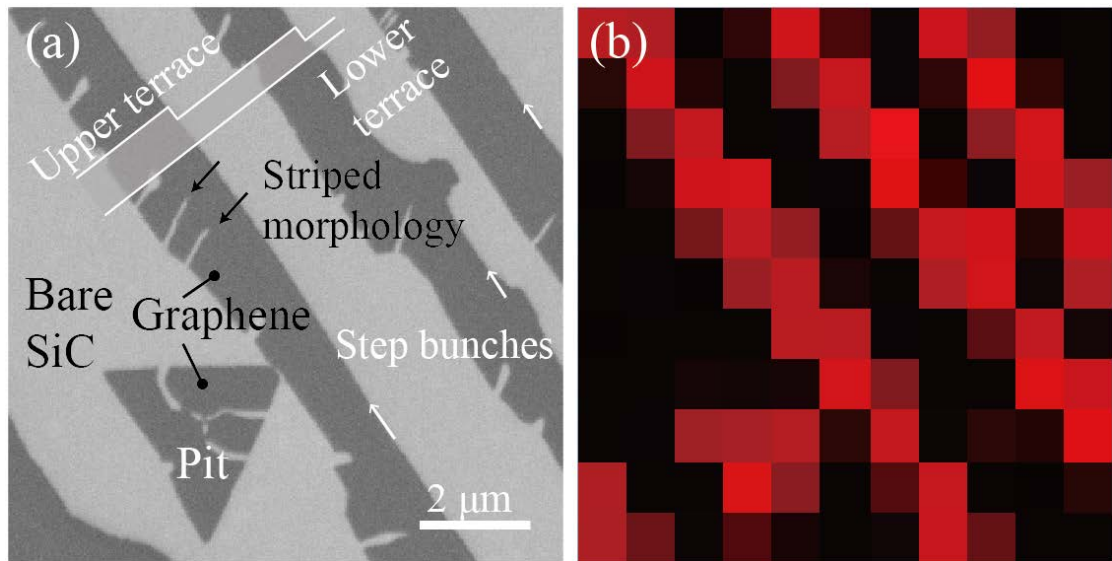


Figure 4.4: (a) SEM image of the thermally decomposed SiC (0001) surface after selective oxygen etching, (b) Raman mapping of Graphene 2D peak at the same area of (a).

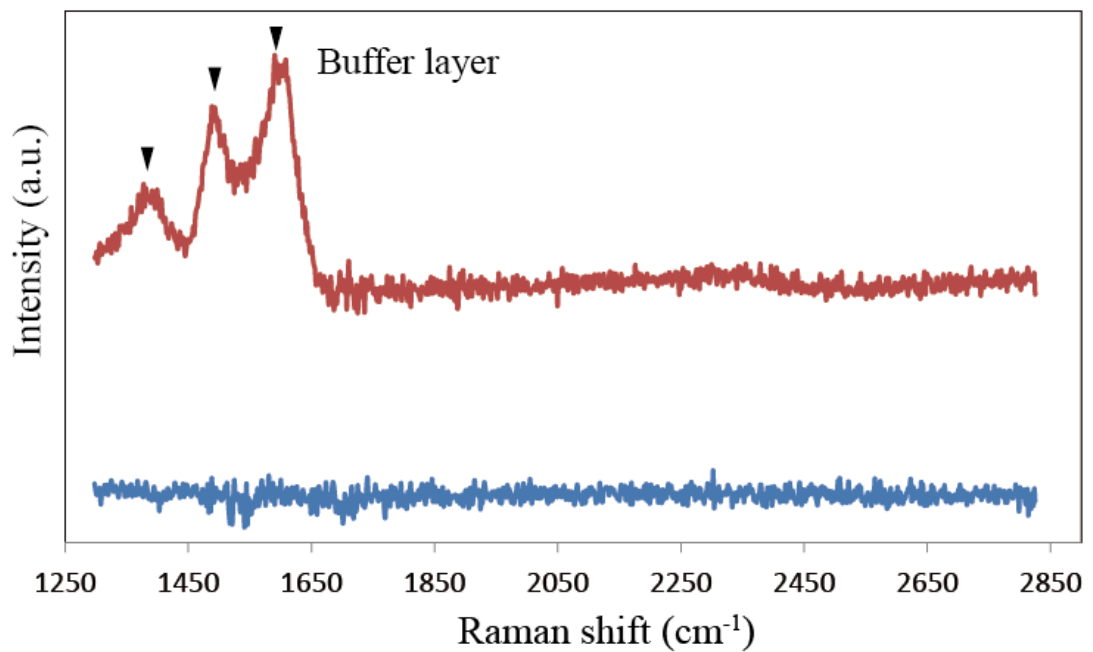


Figure 4.5: Raman spectra measured at surface buffer layer region before (red) and after (blue) the selective oxygen etching.

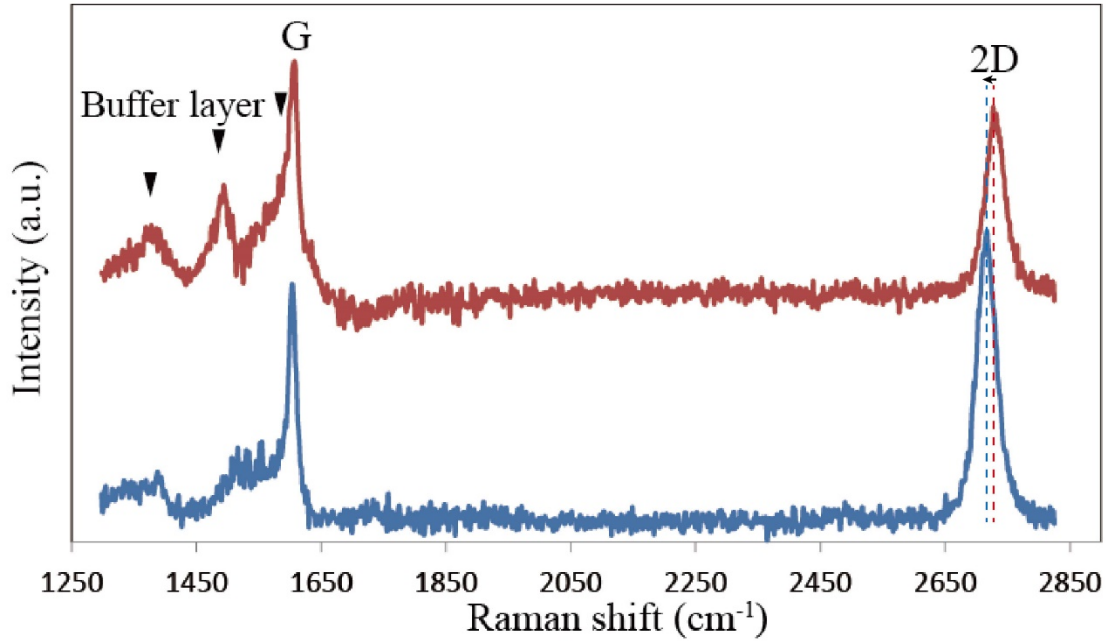


Figure 4.6: Raman spectra measured at graphene region near step bunch before (red) and after (blue) the selective oxygen etching.

Figure 4.7(a) shows an RHEED pattern from the SiC (0001) with graphene layers in the azimuth direction of  $[10\bar{1}0]$  before the oxygen etching, showing diffraction spots of SiC (0001)  $(1\times 1)$ , SiC (0001)  $(6\sqrt{3}\times 6\sqrt{3})R30^\circ$ , graphene  $(1\times 1)$  and the satellites due to secondary scatterings between SiC and graphene [48]. The  $(6\sqrt{3}\times 6\sqrt{3})R30^\circ$  spots, which indicates the presence of buffer layers, though weak, still exist in the RHEED pattern after the oxygen etching (Figure 4.7(b)). As a comparative experiment, a graphene formed SiC (0001) sample was annealed in 0.1-atm-hydrogen at 800°C for 10 min to bring about hydrogen intercalation on its surface, and the surface structure changes were also investigated by the RHEED, as shown in Figure 4.8. The pattern before the intercalation in Figure 4.8(a) shows the spots of buffer layers, SiC and graphene, which are the same as those in the RHEED pattern of Figure 4.7(a). However, due to the hydrogen intercalation between the SiC surface and buffer layers, the entire buffer layer was decoupled from the SiC substrate, such that only the spots of SiC and graphene with their satellites remain in the RHEED pattern in Figure 4.8(b). The same phenomenon can also be observed by the

RHEED patterns in the azimuth direction of  $[1\bar{2}10]$ , as shown in Figures 4.8(c) and (d).

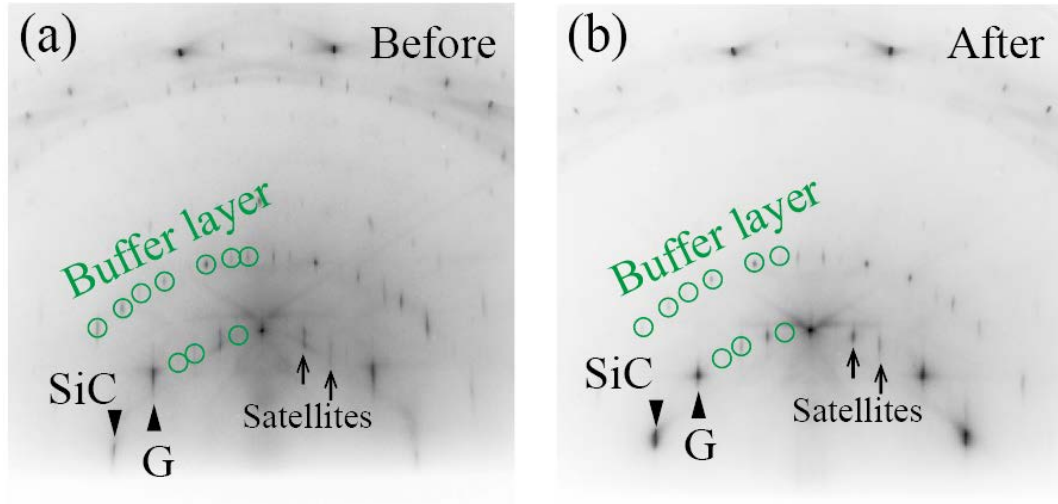


Figure 4.7: RHEED patterns from the center of the SiC (0001) substrate with graphene (G) formation (a) before and (b) after 15 min of the selective oxygen etching. Both patterns are obtained in the azimuth of  $[10\bar{1}0]$ .

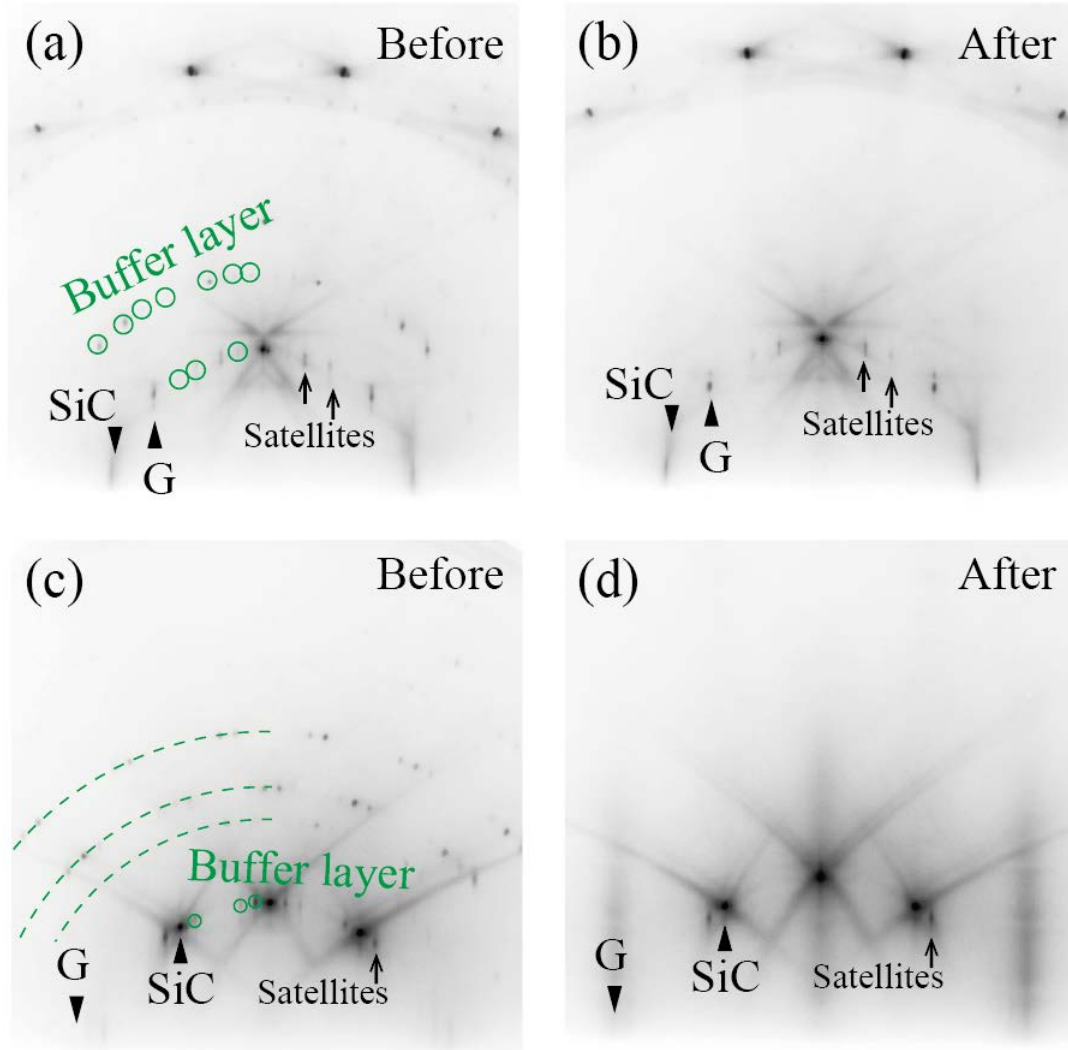


Figure 4.8: RHEED patterns of graphene formed on SiC (0001) (a, c) before and (b, d) after hydrogen intercalation by annealing in 0.1-atm- $H_2$  at 800°C for 10 min. (a, b)  $[10\bar{1}0]$  and (c, d)  $[\bar{1}2\bar{1}0]$  azimuths.

Figure 4.9(a) shows an SEM image of an oxygen etched surface where monolayer graphene formed from step bunches with the striped morphology. An STM image taken from a region indicated by a black frame in Figure 4.9(a) is shown in Figure 4.9(b), in which a graphene area with the striped morphology can be observed. Figure 4.9(c) shows a magnified STM image of the graphene area scanned in a black dashed frame in Figure 4.9(b), where a clear moiré pattern of SiC (0001) ( $6\sqrt{3} \times 6\sqrt{3}$ ) is observed with a random entire undulation besides the moiré pattern. For a comparison, an STM image of graphene area without the selective oxygen etching is

shown in Figure 4.10. Graphene areas with the striped morphology are hard to be recognized, and boundaries of graphene areas are shown by the dashed white lines.

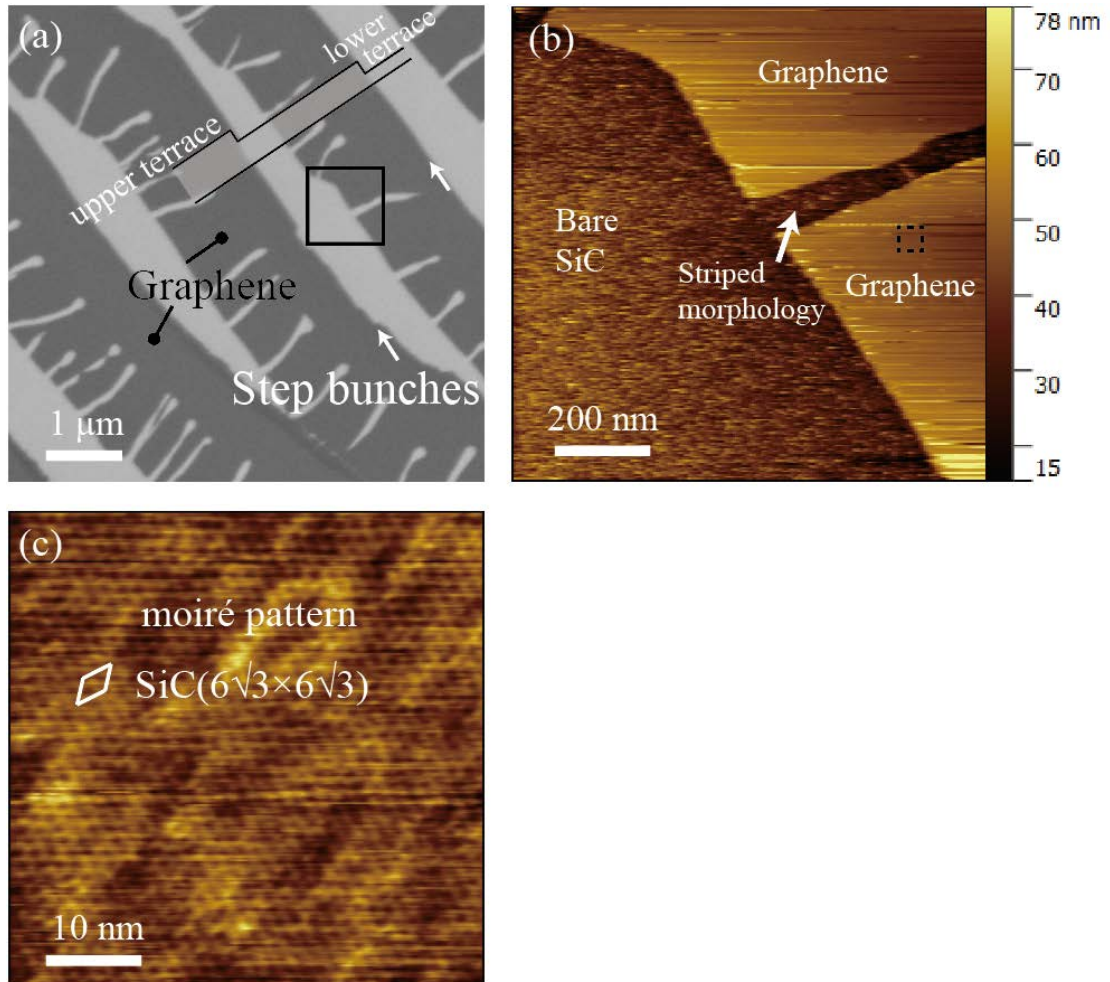


Figure 4.9: (a) SEM image of a graphene formed surface after selective oxygen etching, (b) STM image scanned in a black frame in (a), (c) STM image scanned in a black dashed frame in (b). STM images are taken at  $V_b = -1.5$  V,  $I_t = 0.1$  nA.

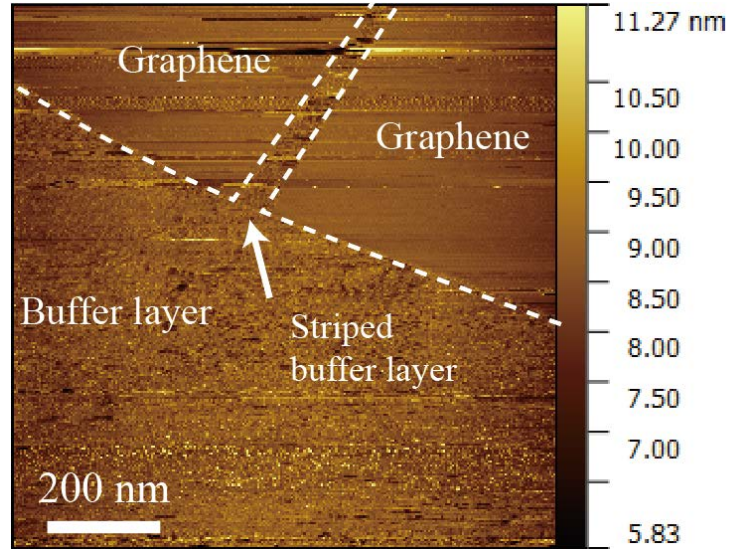


Figure 4.10: STM image of graphene and buffer layer area without the selective oxygen etching ( $V_b=-1.5$  V,  $I_t=0.1$  nA).

### 4.2.3 Etching processes of surface buffer layer

To investigate the surface changes during the selective oxygen etching, 5 min annealing in the  $O_2$ -Ar mixture was repeated 3 times, and the same position on the surface was observed after each annealing by SEM. Figure 4.11 shows a series of SEM images of the buffer layer region (relatively low temperature region) before (Figure 4.11(a)) and after the oxygen etching for 5 min (Figure 4.11(b)), 10 min (Figure 4.11(c)) and 15 min (Figure 4.11(d)).

In Figure 4.11(a), buffer layers on terraces and a bare SiC terrace where buffer layer does not form yet (at the lower-left corner with a brighter contrast) are observed. Thin lines with a bright contrast indicated by white arrows are step bunches between the terraces covered with buffer layers. After oxygen etching for 5 min (Figure 4.11(b)), bands with the bright contrast expand their width to about 100 nm near the step bunches (v-shaped black arrows). The step bunches are recognized by a line profile from A to B in Figure 4.11(b), as shown in Figure 4.11(e), indicating the buffer layer is etched and bare SiC surfaces appear near the step bunches. Some bright spots,

indicated by black triangles, appear on terraces, suggesting the etching on the buffer layer surface. Moreover, as observed at the lower left corner of Figure 4.11(b), a ruggedly etched edge appears at the downside of a step bunch which is different from the case of the smooth etching at other edges. Actually, some etching sites are also observed at the downside of step bunches, as indicated by black arrows in Figure 4.12 (larger area view of Figure 4.11(b)).

By subsequent oxygen etching for 10 min in total (Figure 4.11(c)), buffer layers are further etched from step bunches (v-shaped black arrows) and on surfaces (black triangles), forming wider areas of bare SiC surfaces. The etching is also observed began to occur on the entire buffer layer area with forming bright freckles on it. The SEM image of Figure 4.11(c) also shows that the etching of surface buffer layer occurs non-uniformly on a terrace. Figure 4.11(f) shows a section profile of average contrast change across the dashed frame region from C to D in the image of Figure 4.11(c). Finally, in Figure 4.11(d), after oxygen etching for 15 min, the entire buffer layer is etched off and the whole surface changed to a bare SiC surface.

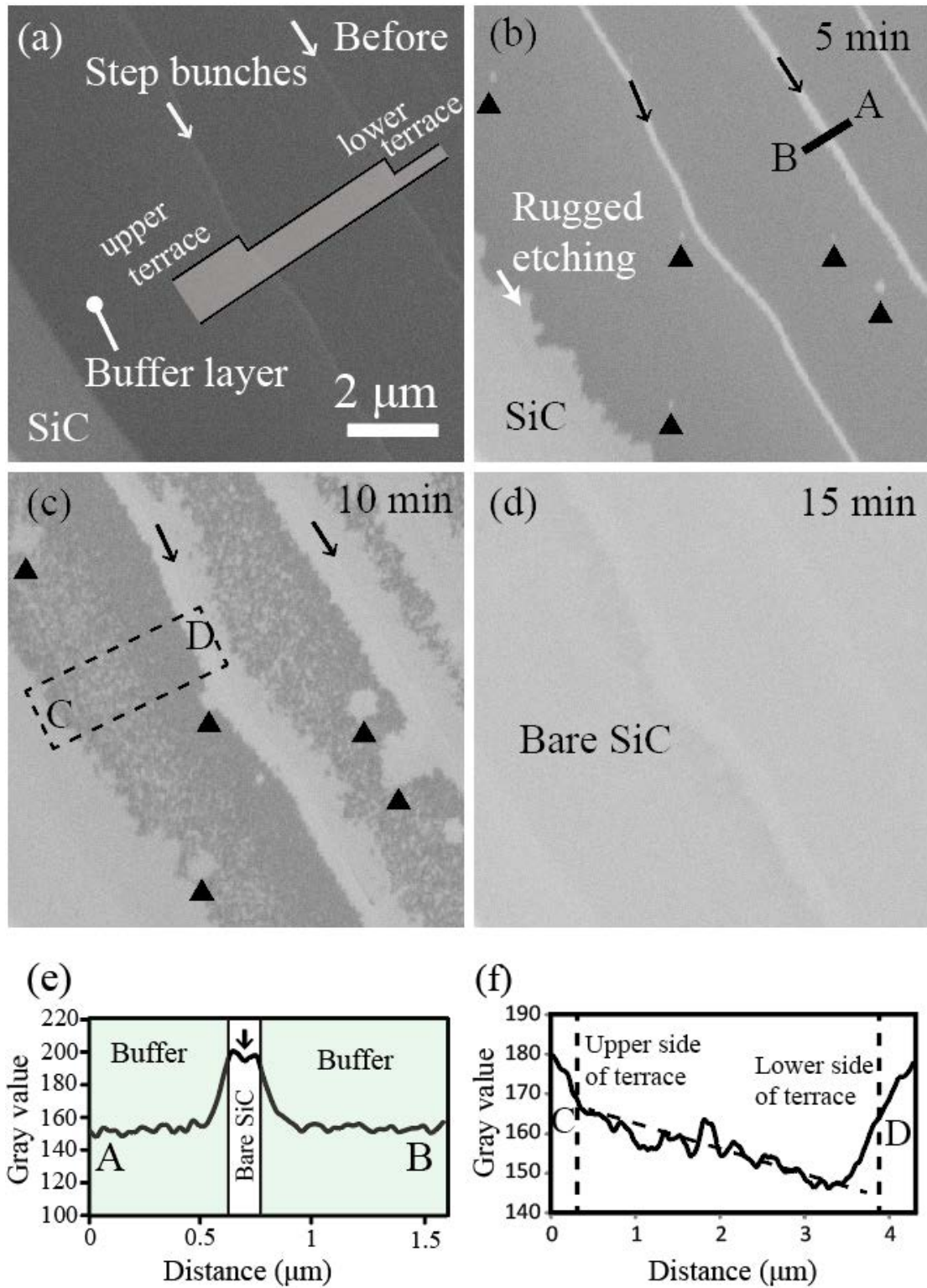


Figure 4.11: Series of SEM images of surface changes during the selective oxygen etching at a buffer layer formed region: (a) before the etching, (b) after the etching for 5 min. (c) after the etching for 10 min, (d) after the etching for 15 min. (e) Section profile along the black line A-B in (b). (f) Average contrast change (gray value) across a dashed frame region in (c).

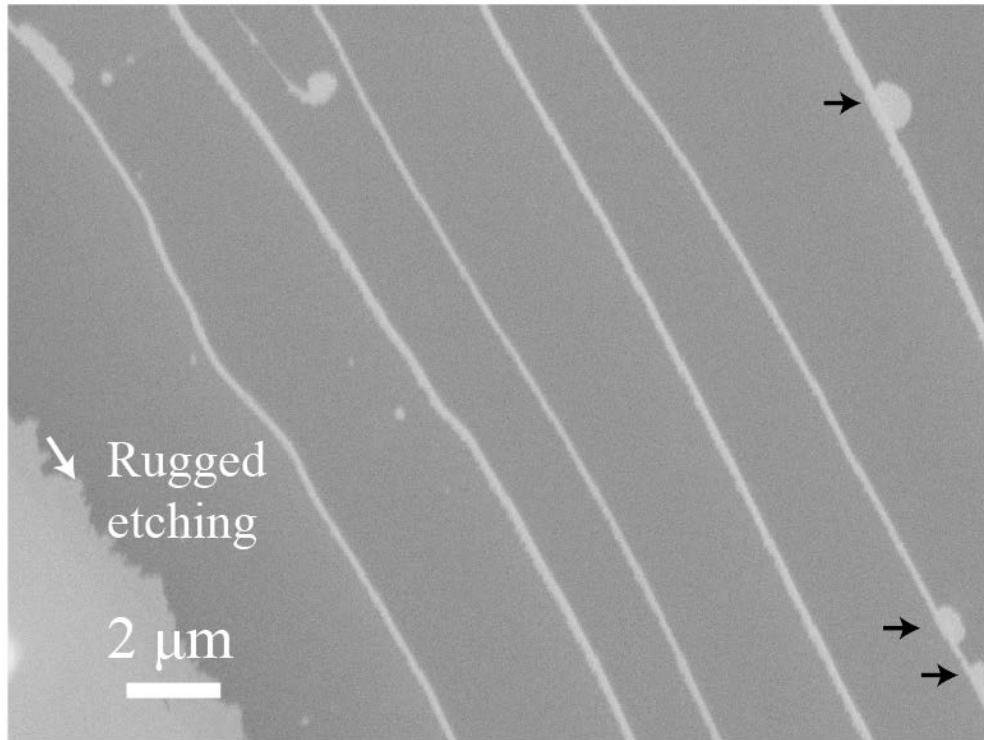


Figure 4.12: SEM image scanned over an area wider than that of Figure 4.11(b).

## 4.3 Discussions

### 4.3.1 Etching of surface buffer layer under oxygen-argon mixture

The graphene Raman results revealed that surface buffer layer is removed, and graphene layers survived after the oxygen etching in the O<sub>2</sub>-Ar atmosphere. In Figure 4.6, the red shift of the 2D peak (spectrum after the etching) is due to a stretched strain after the formation of Si oxide (Si<sup>+</sup> and Si<sup>4+</sup>) between carbon layers and SiC substrate after oxygen treatment [65, 58], which means that the SiC substrates in our case is slightly oxidized. However, the width of the 2D peak did not change, which is contradictory to the formation of bilayer graphene.

The *in situ* RHEED observations (Figures 4.7 and 4.9) also support the presence of buffer layer underneath the monolayer graphene after the oxygen treatment. Since

the surface buffer layer is completely etched by oxygen treatment, as shown by the Raman spectra (Figure 4.5), so that the  $6\sqrt{3} \times 6\sqrt{3}$  spots in the RHEED pattern (Figure 4.7(b)) indicates the presence of the buffer layer underneath the monolayer graphene. In other words, if the oxygen etching decoupled the buffer layer by intercalation, the  $6\sqrt{3} \times 6\sqrt{3}$  spots would disappear as shown for the case of hydrogen intercalation in Figure 4.8.

As revealed by in the STM image (Figure 4.9(b)), the bare SiC areas are imaged as lower height due to the lower conductivity of SiC than graphene, which also supports the idea that the surface buffer layer is etched off. For the comparison with the etched surface in Figure 4.9(b), Figure 4.10(d) shows an STM image of graphene area without the selective oxygen etching, in which the surface buffer layer exists and is at the same height level with the graphene region. In addition, the moiré pattern in Figure 4.9(c) demonstrates the existence of the buffer layer under monolayer graphene, which is consistent with the Raman (Figure 4.6) and RHEED observations (Figure 4.7). For the monolayer graphene area, the random entire undulation in Figure 4.9(c) is probably because of the formation of small amounts of oxide under carbon layers, corresponding to the red shift of graphene 2D peak in Figure 4.6. Thus, all the above facts suggested that the annealing in the extreme low partial pressure oxygen atmosphere caused a selective etching of the surface buffer layer on terraces, while the buffer layer underneath monolayer graphene still exists as the buffer layer.

### **4.3.2 Mechanisms of surface buffer layer etching**

We have observed the processes of the selective etching of surface buffer layers as shown in Figure 4.11. As illustrated the etching processes in Figure 4.13, it is found that besides from the step bunches the etching also starts at some positions in the surfaces buffer layer after oxygen etching for 5 min. Such etching may occur at a defect of buffer layer, since plenty defects and strain exist due to the  $sp^2$ -to- $sp^3$

rehybridization structure on buffer layer [69]. It is common that the edges and defects with a lower chemical stability are etched first. Then the further annealing brought about the entire etching of surface buffer and finally bare SiC appeared on the substrate surface. Figures 4.11(c) and (f) also reveal the contrast change across the terrace after etching for 10 min. As shown in Figure 4.14, the distribution of gray value indicates higher buffer layer coverage at D side than that at C side. Therefore, surface buffer layer more easily be etched at upper side of a terrace (C side). According to the report from Strupinski et al. [68], the surface buffer layer will form with higher quality and a more ordered structure (better crystallinity) and less  $sp^3$  hybridization under a condition of faster Si sublimation, i.e. more supply of free C atoms. They also reported that a buffer layer formed near the upper side of a step bunch has higher quality due to the abundant supply of C atoms from the step bunch. Thus, our observation can be explained as follow; the surface buffer layer formed at the upper side of a step bunch has a well-organized structure, while the high density of defects and  $sp^2$ -to- $sp^3$  rehybridization in the buffer layer at the lower side of a step bunch due to a deficit of carbon, which makes it much easier to be etched. The ruggedly etched edge in Figure 4.11(b) and the high density etching sites at the lower side of step bunches (Figure 4.12) also agree with this explanation.

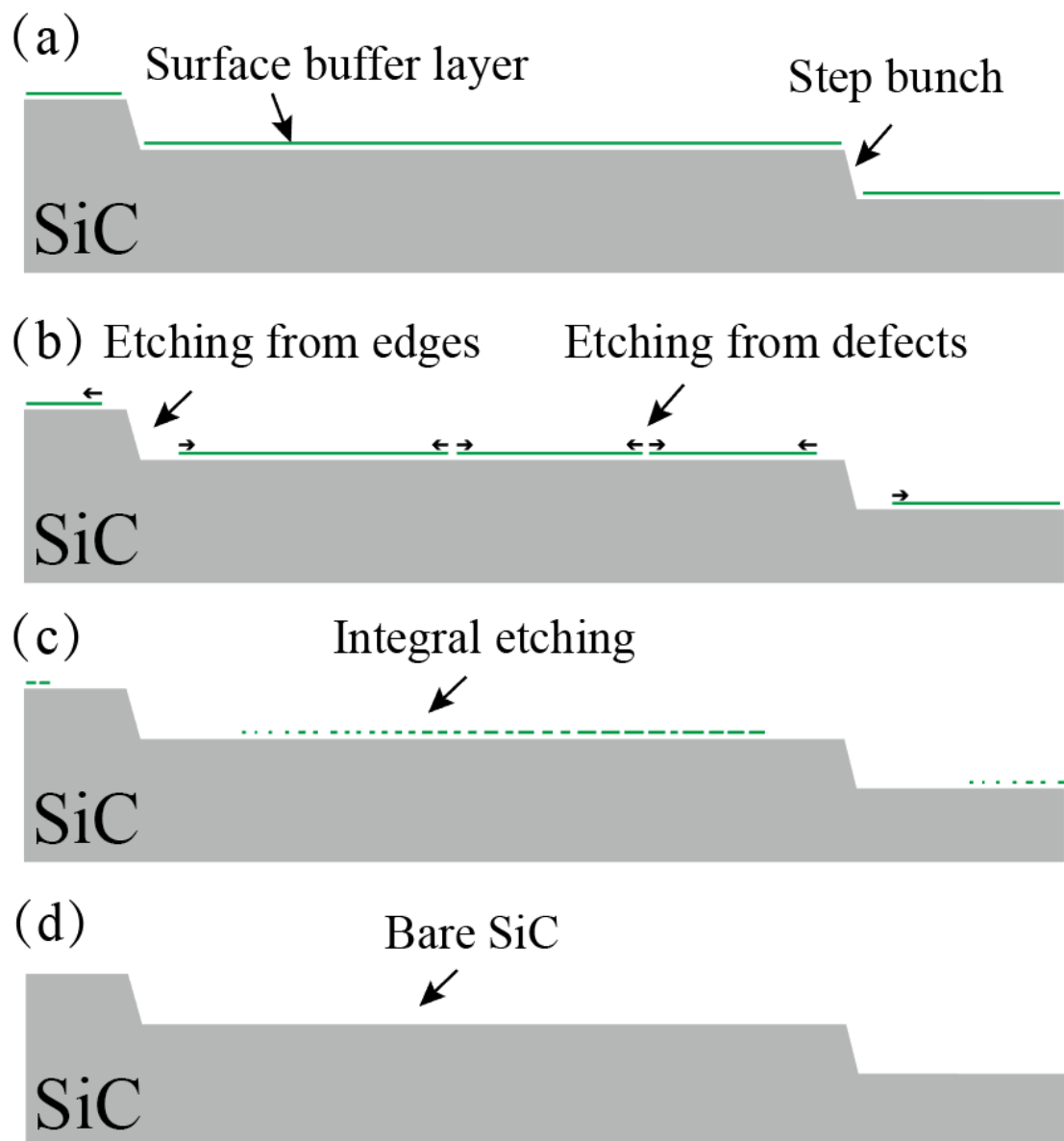


Figure 4.13: Schematic section view of surface buffer layer etching processes. (a) Buffer layers covers on the whole terraces before the etching. (b) The etching starts form buffer layer edges and defects after 5 min. (c) An entire etching is taking place after 10 min. (d) All the buffer layer is etched and bare SiC appears on the surfaces after 15 min.

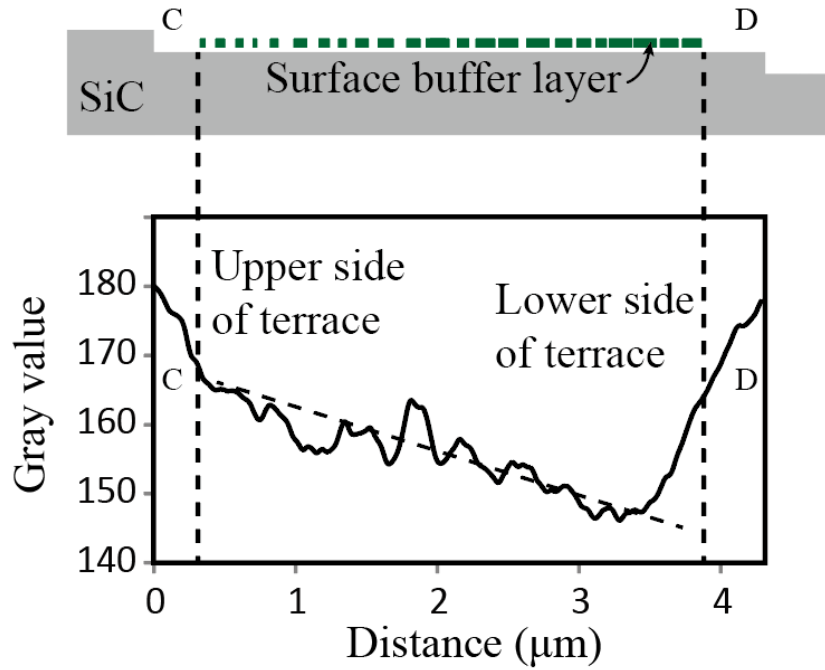


Figure 4.14: Schematic section view of the terrace etched after 10 min in Figure 4.11(c) comparing with the profile of Figure 4.11(f).

## 4.4 Summary

Annealing processes of thermally decomposed SiC (0001) in an O<sub>2</sub>-Ar atmosphere was investigated by *in situ* SEM/STM system. We found that the annealing selectively etched the surface buffer layer on SiC terraces and left the monolayer graphene intact, showing that monolayer graphene was fabricated without the connection to a buffer layer on SiC substrates. It was also found that the non-uniform etching occurred on the surface buffer layer region during the etching process, indicating a spatial change of the crystallinity of the surface buffer layer on a terrace.

# Chapter 5 Formation and Oxygen Etching of Graphene Nanoribbon

## 5.1 Introduction

Generally, graphene nanoribbons are produced from graphene sheets by conventional lithography methods [70, 71]. As shown in Figure 5.1, Wang et al. utilized aluminum (Al) nano-lines as a mask on a graphene sheet for the lithography. After an etching by Ar plasma, graphene nanoribbons with the width about 20 nm was remained. However, the lithography always brings about defects and disordered edge structures of the ribbons [72, 73]. The thermal decomposition of SiC (0001) has been used for fabrication of high quality graphene nanoribbons. Sprinkle et al. reported the formation of graphene nanoribbon at the side-wall of the step edges on a patterned SiC (0001) surface [74], as shown in Figure 5.2. By a further annealing, as new buffer layer forms underneath surface buffer layer, graphene nanoribbons can also grow on terraces by extending side-wall ribbons [38, 66]. Due to the property of epitaxial graphene growth on SiC, fabrication of graphene nanoribbons by thermal decomposition of SiC is a self-organized growth method. In other words, the edge types of graphene nanoribbons are controlled by the orientation of SiC step edges, and no further processing is necessary.

However, there are still some key issues remained in this method. Previous studies [75, 76] have shown a fact that the graphene nanoribbon at step edges is always bonded to a buffer layer on the terrace, being similar with the situation of the connection between surface buffer layer and monolayer graphene, as described in Chapter 4. Although TEM studies [77] and simulations [78] indicated the graphene formation at the step edges, there is still no detailed description about the connection of graphene nanoribbon and surface buffer layer.

In fact, there is only few studies on growth process of graphene nanoribbons at SiC (0001) step edges, and it is still short of knowledge about its growth mechanism. In this research, we observe the formation processes of graphene nanoribbons at the step edge by *in situ* SEM/STM system. Moreover, because of the connection between graphene nanoribbon and surface buffer layer, the unique features of edge states, i.e. band gaps and spin states, do not emerge. Such that the selective etching of surface buffer layer is also carried out for graphene nanoribbons formed surfaces.

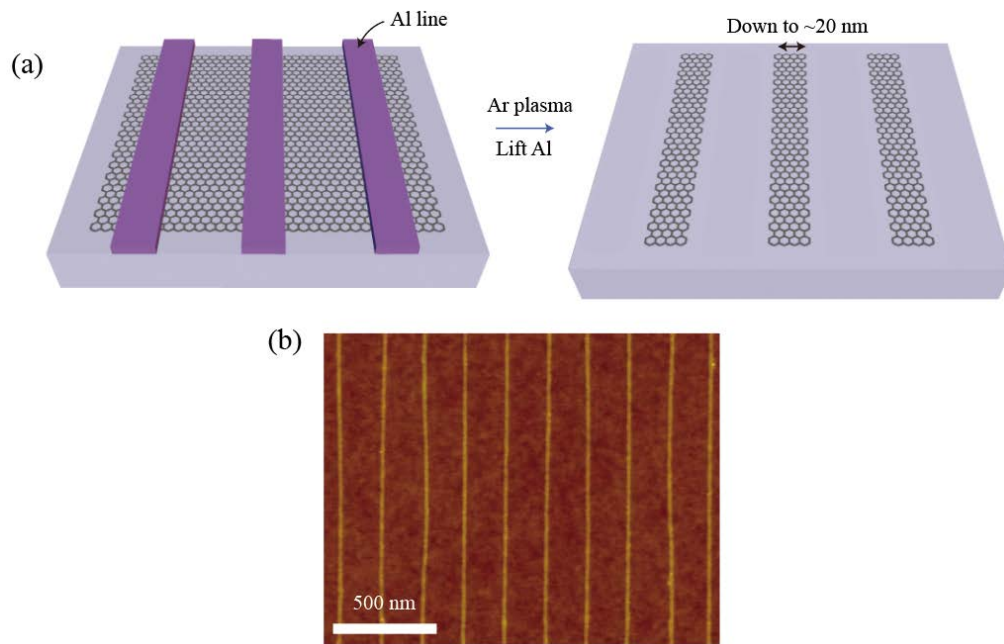


Figure 5.1: (a) Schematic diagrams of formation process of graphene nanoribbon by lithograph. Al lines are firstly covered on a graphene sheet (left). After an Ar plasma etching and removing Al lines, nanoribbons is formed with the width about 20 nm. (b) AFM image of 20-nm graphene nanoribbons by the lithograph [70].

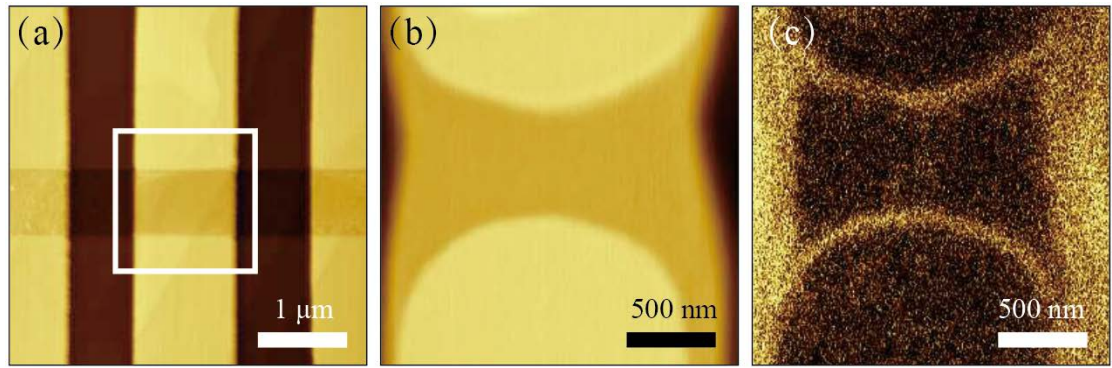


Figure 5.2: (a) AFM image of a patterned SiC (0001) surface. A horizontal trench (20 nm of the depth) in the center and two longitudinal trenches (100 nm of the depth) at flank are patterned on the surface. (b) AFM image of the outlined area in (a) after the graphene formation. (c) EFM image of the area of (b). Bright contrast indicates the graphene nanoribbon with the width about 40 nm [74].

## 5.2 Experimental and results

The patterned vicinal SiC (0001) substrates were used for the investigation in this section. After the hydrogen etching (0.1-atm-hydrogen at 1300°C for 15 min), graphene formation was carried out by annealing at 1550°C for 1 hour in a 1-atm-Ar atmosphere. As mentioned in section 2.1.3, due to the temperature distribution by resistive heating, we can always find a buffer layer region at the low temperature regions on the substrate surfaces after graphene formation. Figure 5.3 (a) shows an SEM image of a buffer layer area, and the two contrasts signify the presence of two regions, the bare SiC (bright) and buffer layers (dark). The surface area indicated by a dashed square is also observed by STM as shown in Figure 5.3 (b), in which the buffer layer is formed from the step bunches (dashed arrows). Figure 5.3 (c) shows an SEM image of another buffer layer area where the buffer layer has fully covered the terraces. Bright contrasts between the buffer layers indicates the positions of step bunches (dashed arrows).

Growth processes of graphene nanoribbons are also observed as shown the SEM

images in Figure 5.4. Figure 5.4 (a) indicates a surface of buffer layer after graphene formation at 1550°C for 15 min in 1-atm-Ar atmosphere. The buffer layer has covered on the whole terraces and left straight step bunches with the bright contrast (black dashed arrows). After the next 15 min annealing, ribbons formed from the step bunches on the terraces with a width of appropriately about 200 nm. The same growth processes are shown in Figures 5.4(c) and (d), in which ribbons can form along curved step bunches on the terraces. Notably, graphene nanoribbons are grown only on the terraces which is fully covered by the surface buffer layer.

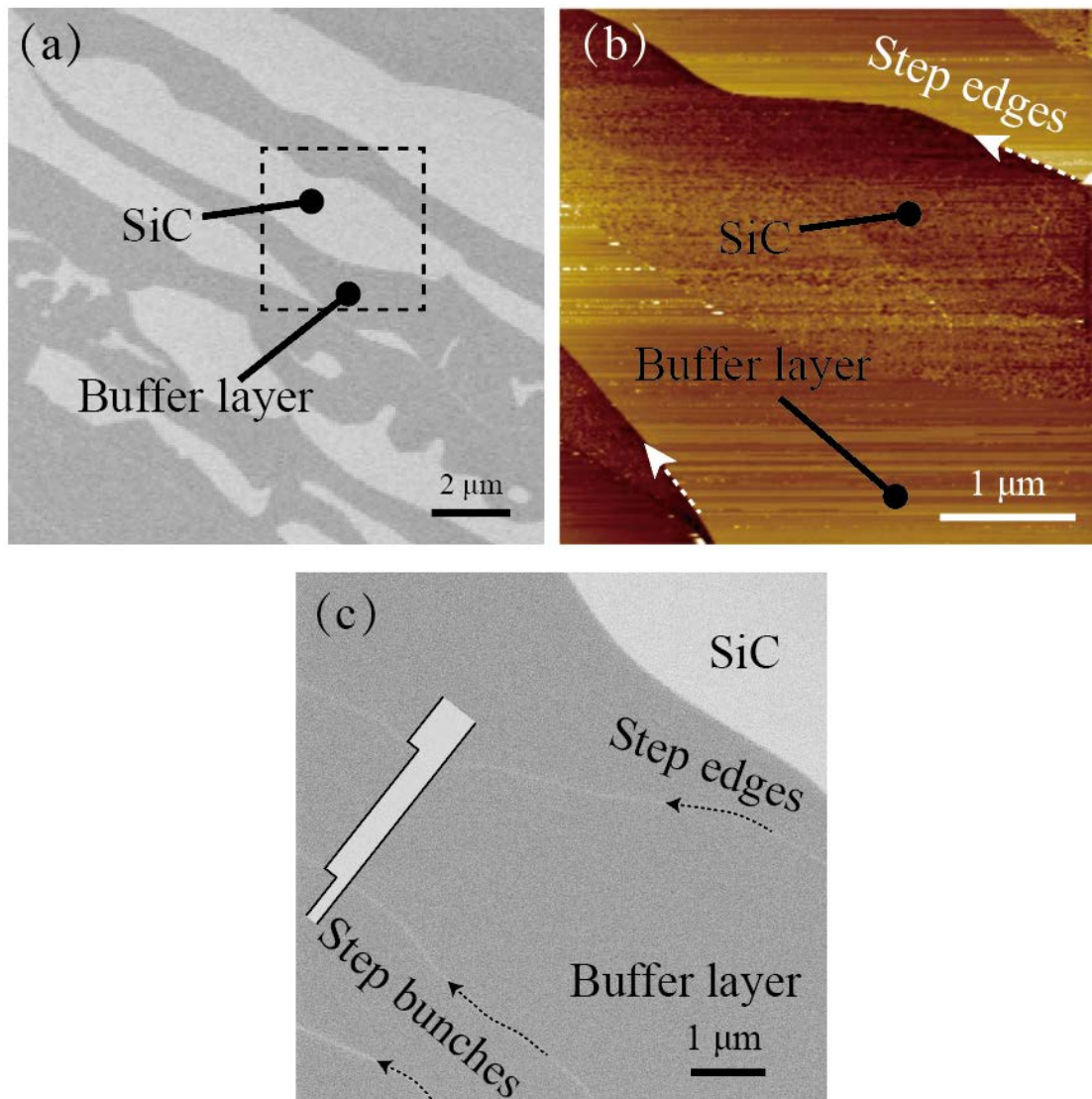


Figure 5.3: (a) SEM image of a buffer layer region. (b) STM image scanned at a dashed outline area in (a) at  $V_b = -1.5$  V,  $I_t = 0.1$  nA. (c) SEM image of a buffer layer region with a larger buffer layer coverage than that of (a).

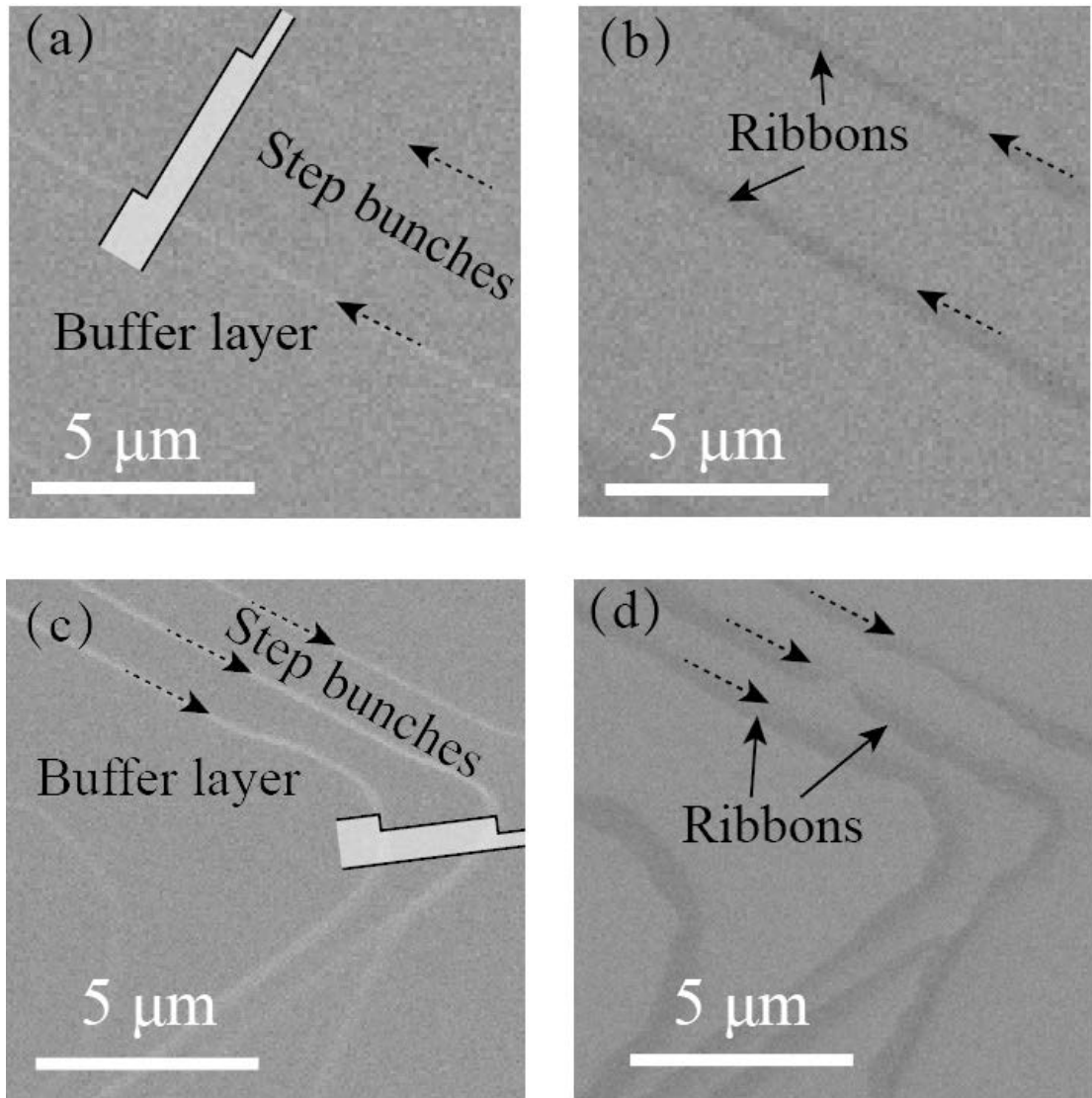


Figure 5.4: SEM images of a position with (a) the buffer layer surface after the annealing at 1550°C for 15 min and (b) graphene nanoribbons at straight step bunches after the annealing for 30 min in total. (c) and (d) SEM images of ribbon formation in another position of the same sample with curved step bunches on the surface.

The selective oxygen etching of the graphene nanoribbon formed surface was carried out to remove the surface buffer layer and fabricate graphene nanoribbons with free edges. The etching was carried out in the O<sub>2</sub>-Ar mixture (O<sub>2</sub>: ~10<sup>-3</sup>Pa, Ar: 1 atm) for 5 min annealing and repeated 3 times. The same position on the surface was observed after each annealing by *in situ* SEM. A series of SEM images in Figure 5.5 show changes of surface morphology caused by the etching in a region where monolayer graphene nanoribbons (shown by arrows in Figure 5.5(a)) had grown at

step bunches with width of tens nm to about 200 nm. The first 5-min oxygen etching did not bring about noticeable change in morphology, as shown in Figure 5.5(b). Subsequently, the etching of entire buffer layer areas started (Figure 5.5(c)) and finally only graphene nanoribbons remained on the SiC surface (Figure 5.5(d)). Since the direction of step edges is not controlled before the graphene formation in the present experiment, the graphene nanoribbons with free edges (open edges) shown in Figure 5.5(d) has mixed edges of armchair and zigzag types.

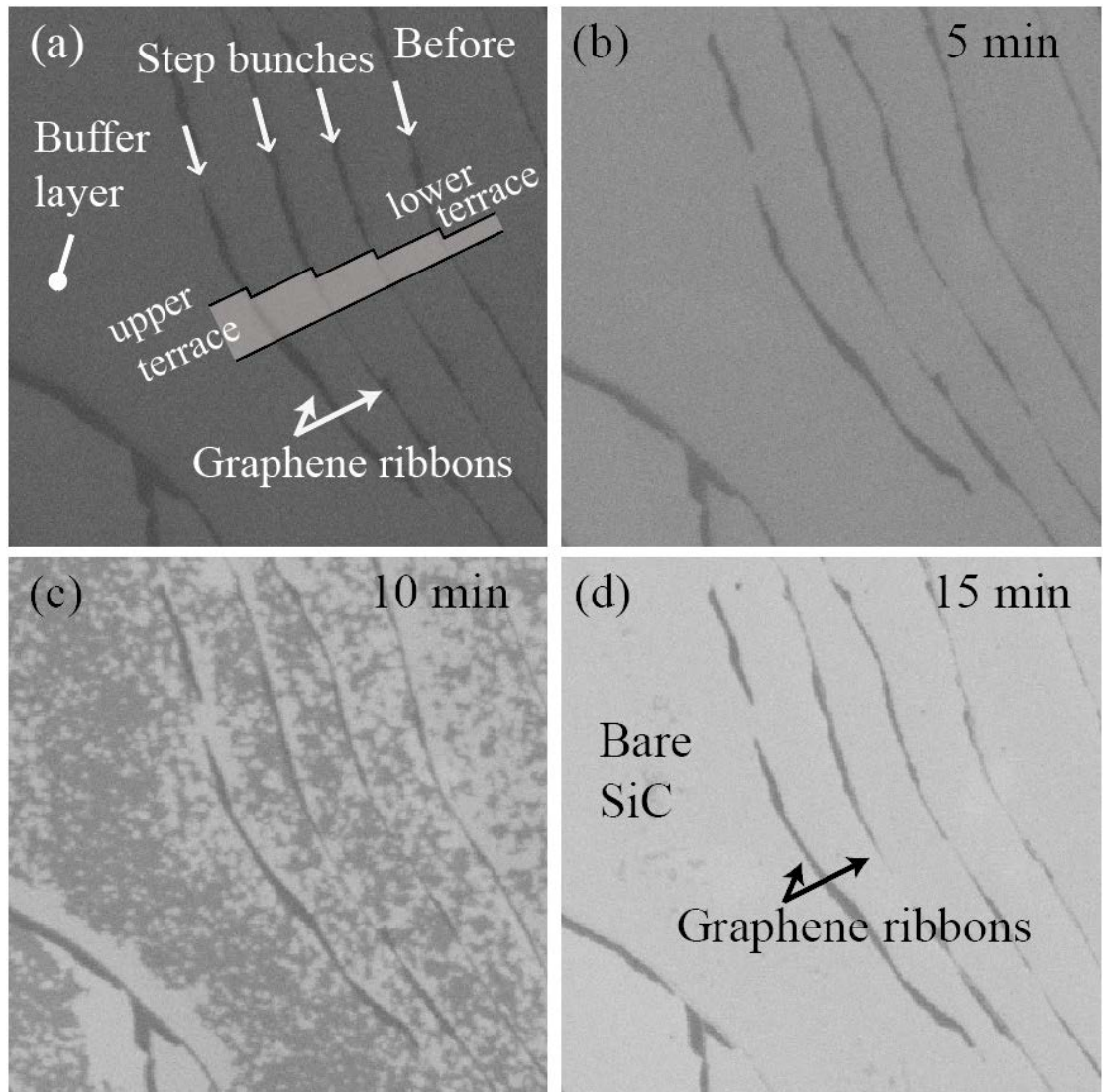


Figure 5.5: Series of SEM images ( $10 \times 10 \mu\text{m}$ ) of surface changes with time during the selective oxygen etching at a graphene nanoribbon formed region.

## 5.3 Discussions

### 5.3.1 Formation processes of graphene nanoribbons

Figures 5.3 and 5.4 show that during the annealing progress, surface buffer layers firstly grow from step bunches, and graphene nanoribbons start forming after the whole terrace surface is covered with buffer layer. In the previous studies [25, 77, 78], the side-wall graphene nanoribbons formed before the surface buffer layer formation, which does not agree with our observations of the growth processes. Although it is difficult to recognize side-wall graphene nanoribbons (about 20 nm in width) in our SEM images directly, our observations can be supported by following points. Firstly, we always observe the bright contrast at step bunches after buffer layers cover the whole wide terraces (Figure 5.3(c), Figures 5.4(a) and (c)), which may indicate the remaining of bare SiC side walls. Although such bright contrast could be caused by the slope at the step bunches, the contrast is absent after the formation of monolayer graphene nanoribbons on the terraces, as shown in Figures 5.4(b) and (d). Secondly, we have observed the etching of buffer layer edges near the step bunches in Figure 4.11, which also indicates the absence of side-wall graphene nanoribbons. Otherwise, the connection of side-wall graphene nanoribbons will protect the buffer layer edges from the etching (discussed below). Besides, previous AFM and electrostatic force microscopy (EFM) studies also show the absence of side-wall graphene nanoribbon at step edges for a surface on which the buffer layer covers the whole terraces [68]. Thus, we consider that the surface buffer layer grows over the whole terraces before the side-wall graphene nanoribbon formation, as illustrated in Figure 5.6.

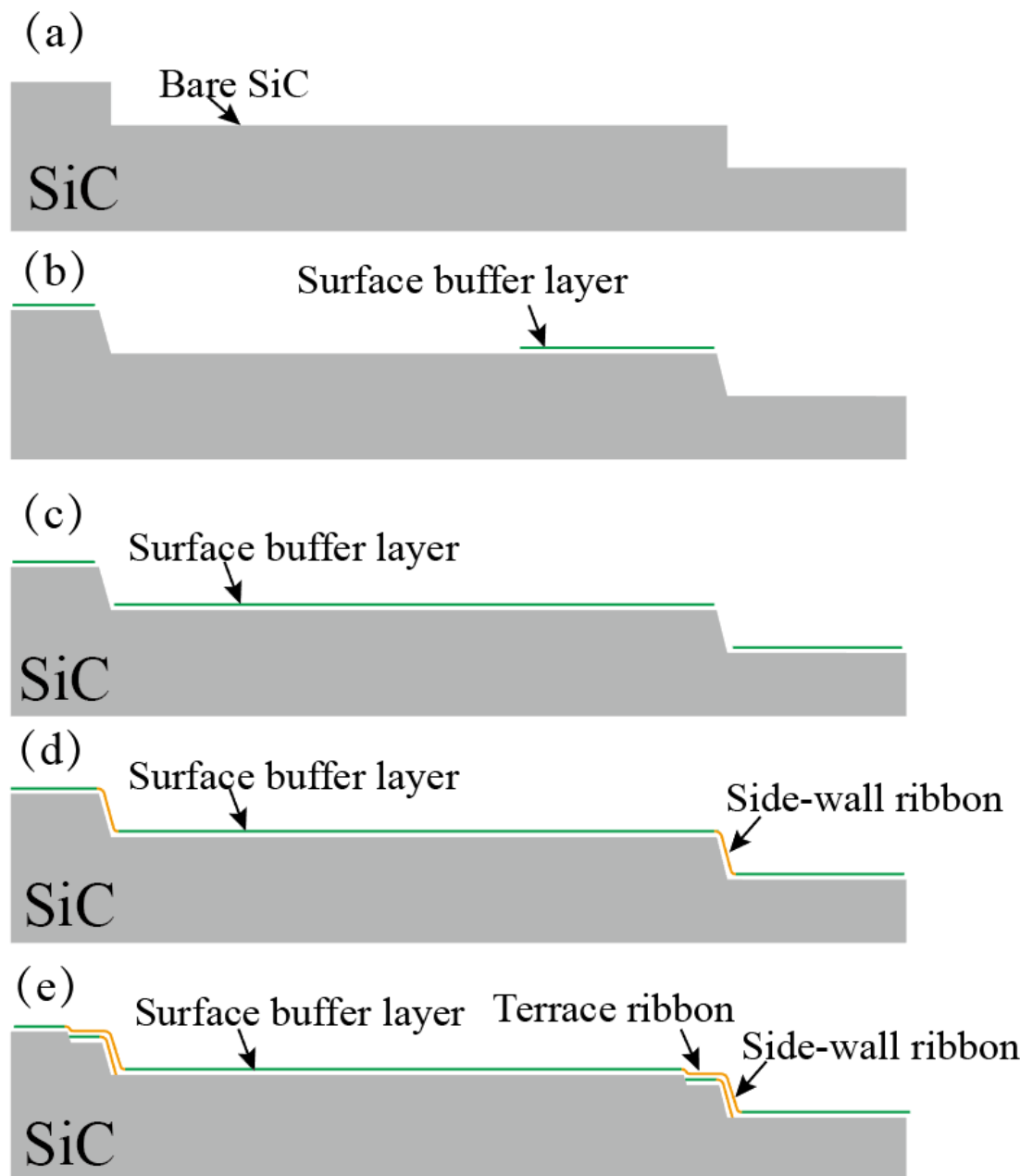


Figure 5.6: Schematic section view of the growth processes of graphene nanoribbon at the step bunches on SiC (0001). (a) A bare SiC surface is shown before the formation. (b) Surface buffer layers start to grow from the step bunch. (c) Surface buffer layer covers the whole terrace without graphene nanoribbon formation. (d) Ribbons start to form at the side-wall of the step bunch. (e) Ribbons grow and extend on the terrace from the step bunch.

### 5.3.2 Etching of surface buffer layer

As shown in the etching processes of surface buffer layer in Figure 5.5, surface buffer layer is removed away and remain the 200-nm-width ribbons at step bunches. In Chapter 4, we have observed the selective oxygen etching process at buffer layer regions, where buffer layer edges are firstly etched from step bunches and at defects after oxygen etching for 5 min (Figure 4.11(b)). However, such etching of buffer layers did not occur for the present case which graphene nanoribbon formed at the step edges (Figure 5.5(b)). When graphene nanoribbons formed at step edges, ribbons are connected to the surface buffer layer at both the upper and lower sides of step edges [25], which prevents the buffer layer from etching at the step bunches. And also, the surface buffer layer formed in graphene nanoribbon areas at the higher temperature (compared to the case of buffer layer region discussed in Chapter 4 in Figure 4.11(b)) has a better crystallinity, which avoids the etching at defects.

It should also be noted that the non-uniform etching (the case in Figure 4.11(c)) on terraces did not occur after the oxygen etching for 10 min, as shown in Figure 5.5(c). It means a faster Si sublimation on the higher temperature surface supplies sufficient C atoms to facilitate the formation of the high-quality surface buffer layer, which also corresponds to the absence of defects mentioned above. Such investigation also agrees with the report in the previous study [68].

## 5.4 Summary

In this chapter, the study on the growth processes of graphene nanoribbon on SiC (0001) under Ar atmosphere demonstrated that ribbons on the terraces form after the surface buffer layer covered on the whole terrace. Side-wall graphene also grew after the finish of the covering surface buffer layer on terraces.

Etching in an O<sub>2</sub>-Ar atmosphere also brought about the selectively removing of

surface buffer layer and the formation of free edge monolayer graphene nanoribbons (side-wall and terrace ribbons) along the step bunches, which must be significant for the fabrication of monolayer graphene nanoribbon and its applications in graphene electronic/spintronic devices.

# Chapter 6 Conclusion and Perspective

## 6.1 Conclusion

In this study, utilizing the *in situ* UHV-SEM/STM, the surface changes during the annealing of SiC (0001) substrates in Ar atmosphere and oxygen were investigated. In chapter 1 the background and current situations about epitaxial graphene growth on SiC by thermal decomposition were shown. We realized that such method is very appropriate to the applications of graphene/SiC electronic devices, but further understandings of its growth processes and mechanism are necessary for an accurate control of graphene formation technology at wafer-scale. In chapter 2, the methods of sample preparations and characterizations were explained. By utilizing the UHV-SEM/STM system in this research, preparations and SEM/STM observations of samples can be carried out in the same vacuum system. In chapter 3, the effects of SiC (0001) surface morphology, annealing temperature and Ar pressures on the graphene growth and their mechanisms were discussed. A monolayer graphene layer with domain size about 10  $\mu\text{m}$  was produced on a step-free SiC substrate. We also found that 1400°C is the most appropriate temperature for SiC step bunching. By the long-time annealing at relatively low temperature (under 1550°C), monolayer graphene grew only from step edges which covered on the  $4 \times 100\mu\text{m}$  terraces without pit formation. During the monolayer graphene forming from step edges, striped buffer layer morphology is always present because of the diffusion of decomposed atoms. In Chapter 4, the selective etching of surface buffer layer in the atmosphere of  $\text{O}_2$  ( $10^{-3}$  Pa)/Ar (1 atm) was revealed and free edge monolayer graphene were formed on SiC substrates. We also found surface buffer layer is formed with various crystallinity on a terrace. Finally, in chapter 5, the growth processes of graphene nanoribbon are discussed. We found graphene nanoribbons only begin to grow after surface buffer layer covered on the whole terraces and free edge monolayer graphene nanoribbons (about 200 nm in width) were fabricated by the selective buffer

layer etching.

## 6.2 Perspective

The above knowledge may bring about new possibilities for the application of graphene/SiC (0001) wafer to semiconductor processes. For example, by utilizing low temperature graphene growth in the Ar atmosphere on a SiC wafer with step edges of designed pattern, a uniform monolayer graphene surface at wafer-scale can be fabricated. The planar structure of graphene on SiC will also bring about great advantages of high-resolution lithography for graphene electronic manufacturing. Then, notably, free edge monolayer graphene nanoribbons were formed along the step edges on SiC substrates by the selective etching of surface buffer layers, which may reveal the original band structures and transport properties of the ribbons. In addition, the band gap can be varied by edge type (i.e. armchair and zigzag edge) and width of the ribbons. Fortunately, for the case of thermal decomposition of SiC, the edge type is easily determined by coordinate of patterned step edges and the widths can be controlled by annealing conditions. Thus, this method will contribute to the applications of graphene nanoribbon on SiC wafers in integrated circuit. By introducing the nanoribbons as on-chip wiring and active device such as transistors, the extreme high mobility and low resistance will further evolve the electronics with higher speed, lower energy consumption and smaller size.

During the past half a century, the whole semiconductor industry developed rapidly by following Moore's law [79]. In recent years, it seems the Moore's law does not work anymore, after the transistor size has reached the order of tens nanometers [80]. Although people have stated the development of 3-dimensional (3D) structure in chips, such as 3D flash memories [81], the key problem of excessive reliance on Si is not solved yet. Carbon nanomaterials, including fullerene (0D), nanotubes (1D), and graphene (2D), are acknowledged as ideal alternate of Si for the next generation of electronic devices. Due to the various properties, many parts from transistors to wires

can be replaced by carbon nanomaterials, which will in the meantime bring about a dramatical evolution of the device performance. To realize the carbon nanomaterials based devices, we are still facing thousands of challenges at device design, process technology, device reliability and so on. Maybe there is another half a century to go with the hard work of research and development, which requires our patience, and someday people will be rewarded for their hard work.

## References

- [1] H. Jussila, H. Yang, N. Granqvist and Z. Sun, Surface plasmon resonance for characterization of large area atomic-layer graphene film, *Optica*, **3** (2016) 151-158.
- [2] J. Hass, W. A. Heer and E. H. Conrad, *J.Phys.Condens. Matter*, **20** (2008) 323202.
- [3] A.H. Castro Neto, F Guinea, N. M. R. Peres, K. S. Novoselov and A. K. Geim, the electronic properties of graphene, *Rev. Mod. Phys.*, **81** (2009) 109-162.
- [4] K. I. Bolotin, K. J. Sikes, Z. Jiang, M. Klima, G. Fudenberg, J. Hone, P. Kim and H. L. Stormer, ultrahigh electron mobility in suspended graphene, *Solid State Commun*, **146** (2008) 351–355.
- [5] A. A. Balandin, S. Ghosh and W. Z. Bao, superior thermal conductive of single-layer graphene, *Nano Lett.*, **8** (2008) 902–907.
- [6] H. K. Chae, D. Y. Siberio-Pérez and J. Kim, a route to high surface area, porosity and inclusion of large molecules in crystals, *Nature*, **427** (2004) 523–527.
- [7] C. Lee, X. Wei, J. W. Kysar, J. Hone, measurement of the elastic properties and intrinsic strength of monolayer graphene, *Science*, **321** (2009) 385-388.
- [8] R. R. Nair, P. Blake, A. N. Grigorenko, K. S. Novoselov, T. J. Booth, T. Stauber, N. M. T. Peres, A. K. Geim, fine structure constant defines visual transparency of graphene, *Science*, **320** (2008) 1308.
- [9] K. S. Novoselov, A. K. Geim and S. V. Morozov, electric field effect in atomically thin carbon films, *Science* **306** (2004) 666–669.
- [10] Y.M. Lin, C. Dimitrakopoulos, K. A. Jenkins, D. B. Farmer, H.Y. Chiu, A. Grill, and Ph. Avouris, 100-GHz transistors from wafer-scale epitaxial graphene, *Science*, **5** (2010) 662.
- [11] C. Xu, H. Li, K. Banerjee, modeling, analysis, and design of graphene nano-ribbon interconnects, *IEEE Trans. Electron Devices*, **56** (2009) 1567.
- [12] Y. Ohno, K. Maehashi, Y. Yamashiro and K. Matsumoto, electrolyte-gated graphene field-effect transistors for detecting pH and protein adsorption,

- Nano Lett., **9** (2009) 3318.
- [13] X. Wang, L. Zhi, K. Mullen, transparent, conductive graphene electrodes for dye-sensitized solar cells. Nano Lett., **8** (2008) 323-327.
- [14] J. Hassoun, F. Bonaccorso, M. Agostini, M. Angelucci, M. G. Betti, T. Cingolani, et al., an advanced lithium-ion battery based on a graphene anode and a lithium iron phosphate cathode, Nano Lett., **14** (2014) 4901-4906.
- [15] K. Nakada, M. Fujita, G. Dresselhaus and M. S. Dresselhaus, edge state in graphene ribbon: nanometer size effect and edge shape dependence, Phys. Rev. B, **54** (1996) 17954.
- [16] H. Mohamadpour and A. Asgari, graphene nanoribbon tunneling field effect transistors, Physica E, **46** (2012) 270-273.
- [17] Y. W. Son, M. L. Cohen, S. G. Louie, half-metallic graphene nanoribbons, Nature, **444** (2006) 347.
- [18] W. Y. Kim and K. S. Kim, prediction of very large values of magnetoresistance in a graphene nanoribbon device, Nat. Nanotechnol., **3** (2008) 408-412.
- [19] C. Mattevi, H. Kim, M. Chhowalla, a review of chemical vapor deposition of graphene on copper, J. Mater. Chem., **21** (2011) 3324-3334.
- [20] X. Li, W. Cai, J. An, S. Kim, J. Nah, D. Yang, R. Piner, A. Velamakanni, large-area synthesis of high-quality and uniform graphene films on copper foils, Science, **324** (2009) 1312-1314.
- [21] X. Li, W. Cai, L. Colombo and R. S. Ruoff, evolution of graphene growth on Ni and Cu by carbon isotope labeling, Nano Lett., **9** (2009) 4268-4272.
- [22] S. Bae, H. Kim, Y. Lee, X. Xu, J. S. Park, Y. Zheng, J. Balakrishnan, T. Lei, et al., roll-to-roll production of 30-inch graphene films for transparent electrodes, Nat. Nanotechnol., **5** (2010) 574-578.
- [23] Y. Wang, S. W. Tong, X. F. Xu, B. Özyilmaz, K. P. Loh, interface engineering of layer-by-layer stacked graphene anodes for high-performance organic solar cells, Adv. Mater, **23** (2011) 1514-1518.
- [24] A. J. Van Bommel, J. E. Crombeen, A. Van Tooren, LEED and Auger

- electron observations of the SiC (0001) surface, *Surf. Sci.*, **48** (1975) 463-472.
- [25] W. Norimatsu and M. Kusunoki, growth of graphene from SiC (0001) surfaces and its mechanisms, *Semicond. Sci. Technol.*, **29** (2014) 064009.
- [26] W. Norimatsu, and M. Kusunoki, transitional structures of the interface between graphene and 6H-SiC (0001), *Chem. Phys. Lett.*, **468** (2009) 52.
- [27] W. Norimatsu, J. Takada, and M. Kusunoki, formation mechanism of graphene layer on SiC (000-1) in a high-pressure argon atmosphere, *Phys. Rev. B*, **84** (2011) 035424.
- [28] J. Hass, C. A. Jeffrey, R. Feng, T. Li, X. Li, C. Berger, W. A. de Heer, P. N. First and E. H. Conrad, highly-ordered graphene for two dimensional electronics, *Appl. Phys. Lett.*, **89** (2006) 143106.
- [29] T. Ohta, A. Bostwick, J. L. McChesney, T. Seyller, K. Horn, and E. Rotenberg, interlayer and electronic screening in multilayer graphene, *Phys. Rev. Lett.*, **98** (2007) 206802.
- [30] K. V. Emtsev, F. Speck, Th. Seyller and L. Ley, interaction, growth, and ordering of epitaxial graphene on SiC {0001} surface: a comparative photoelectron spectroscopy study, *Phys. Rev. B*, **77** (2008) 155303.
- [31] H. Huang, W. Chen, S. Chen and A. T. S. Wee, bottom-up growth of epitaxial graphene on 6H-SiC (0001), *ACS Nano.*, **2** (2008) 2513.
- [32] H. Hibino, H. Kageshima, F. Maeda, M. Nagase, Y. Kobayashi, and H. Yamaguchi, microscopic thickness determination of thin graphite films formed on SiC from quantized oscillation in reflectivity of low-energy electrons, *Phys. Rev. B*, **77** (2008) 075413.
- [33] C. Virojanadara, M. Syväjarvi, R. Yakimova, and L. I. Johansson, homogeneous large-area graphene layer growth on 6H-SiC (0001), *Phys. Rev. B*, **78** (2008) 245403.
- [34] A. Ruammitree, H. Hakahara, K. Akimoto, K. Soda, Y. Saito, determination of non-uniform graphene thickness on SiC (0001) by X-ray diffraction, *Appl. Surf. Sci.*, **282** (2013) 297.

- [35] L. M. Malard, M. A. Pimenta, G. Dresselhaus, M. S. Dresselhaus, Raman spectroscopy in graphene, *Phys. Rep.*, **473** (2009) 51.
- [36] G. Gu, S. Nie, R. M. Feenstra, R. P. Devaty, and W. J. Choyke, field effect in epitaxial graphene on a silicon carbide substrate, *Appl. Phys. Lett.*, **90** (2007) 253507.
- [37] W. A. Heer, C. Berger, M. Ruan, M. Sprinkle, X. Li, Y. Hu, et al., Large area and structured epitaxial graphene produced by confinement controlled sublimation of silicon carbide, *PNAS.*, **108** (2011) 16900.
- [38] K. V. Emtsev, A. Bostwick, K. Horn, J. Jobst, G. L. Kellogg, L. Let, et al., towards wafer-size graphene layers by atmospheric pressure graphitization of silicon carbide, *Nat. Mater.*, **8** (2009) 3318.
- [39] P. Sutter, epitaxial graphene: how silicon leaves the scene, *Nat. Mater.*, **8** (2009) 171.
- [40] C. Held, T. Seyller, and R. Bennewitz, quantitative multichannel NC-AFM data analysis of graphene growth on SiC (0001), *Beilstein J. Nanotechnol.*, **3** (2012) 179.
- [41] Y. Yamamoto, S. Harada, K. Seki, A. Horio, T. Mitsuhashi and T. Ujihara, High-Efficiency Conversion of Threading Screw Dislocations in 4H-SiC by Solution Growth, *Appl. Phys Express*, **5** (2012) 115501.
- [42] M. Hupalo, E. H. Conrad, and M. C. Tringides, growth mechanism for epitaxial graphene on vicinal 6H-SiC (0001) surface: A scanning tunneling microscopy study, *Phys. Rev. B*, **80** (2009) 041401(R).
- [43] W. Norimatsu, M. Kusunoki, transitional structures of the interface between graphene and 6H-SiC (0001), *Chem. Phys. Lett.*, **468** (2009) 52-56.
- [44] W. Zhu, C. Dimitrakopoulos, M. Freitag, P. Avouris, layer number determination and thickness-dependent properties of graphene grown on SiC, *IEEE Trans. Nanotechnol.*, **10** (2011) 1196.
- [45] K. Grodecki, I. Jozwik, J. M. Baranowski D. Teklinska, W. Strupinski, SEM and Raman analysis of graphene on SiC (0001), *Micron*, **80** (2016) 20.
- [46] P. Mallet, F. Varchon, C. Naud, L. Magaud, C. Berger, and J. T. Vuillen,

- electron states of mono and bilayer graphene on SiC probed by scanning tunneling microscopy, *Phys. Rev. B*, **76** (2007) 041403.
- [47] C. Riedl, U. Starke, J. Bernhardt, M. Franke, and K. Heinz, structural properties of the graphene-SiC (0001) interface as a key for the preparation of homogeneous large-terrace graphene surface, *Phys. Rev. B*, **76** (2007) 245406.
- [48] X. N. Xie, H. Q. Wang, A. T. S. Wee and K. P. Loh, the evolution of  $3 \times 3$ ,  $6 \times 6$ ,  $\sqrt{3} \times \sqrt{3}R30^\circ$  and  $6\sqrt{3} \times 6\sqrt{3}R30^\circ$  superstructures on 6H-SiC (0001) surfaces studied by reflection high energy electron diffraction, *Surf. Sci.*, **478** (2001) 57-71.
- [49] M. S. Dresselhaus, G. Dresselhaus, A. Jorio, A. G. Souza Fiho, R. Saito, Raman spectroscopy on isolated single wall carbon nanotubes, *Carbon*, **40** (2002) 2043-2061.
- [50] L. M. Malard, M. A. Pimenta, G. Dresselhaus, M. S. Dresselhaus, Raman spectroscopy in graphene, *Phys. Rep.*, **473** (2009) 51-87.
- [51] G. F. Sun, Y. Liu, S. H. Rhim, J. F. Jia, Q. K. Xue, M. Weinert, and L. Li, Si diffusion path for pit-free graphene growth on SiC (0001), *Phys. Rev. B*, **84** (2011) 195455.
- [52] Y. Ishida and S. Yoshida, investigation of giant step bunching in 4H-SiC homoepitaxial growth: proposal of cluster effect, *Jpn. J. Appl. Phys.*, **54** (2015) 061301.
- [53] V. Borovikov and A. Zangwill, step bunching of vicinal 6H-SiC (0001) surface, *Phys. Rev. B*, **79** (2009) 245413.
- [54] H. Nakagawa, S. Tanaka and I. Suemune, self-ordering of nanofacets on vicinal SiC Surfaces, *Phys. Rev. Lett.*, **91** (2003) 226107.
- [55] V. Borovikov, A. Zangwill, step-edge instability during epitaxial growth of graphene from SiC (0001), *Phys. Rev. B*, **80** (2009) 121406.
- [56] M. Ridene, J. C. Girard, L. David, A. Ouerghi, STM/STS investigation of edge structure in epitaxial graphene, *Surf. Sci.*, **606** (2012) 1289.
- [57] S. W. Poon, W. Chen, A. T. S. Wee and E. S. Tok, growth dynamics and

- kinetics of monolayer and multilayer graphene on a 6H-SiC (0001) substrate, *Phys. Chem. Chem. Phys.*, **12** (2010) 13522-13533.
- [58] D. A. Schmit, T. Ohta and T. E. Beechem, strain and charge carrier coupling in epitaxial graphene, *Phys. Rev. B*, **84** (2011) 235422.
- [59] F. Ming and A. Zangwill, model for the epitaxial growth of graphene on 6H-(0001), *Phys. Rev. B*, **84** (2011) 115459.
- [60] C. Riedl, C. Coletti, T. Iwasaki, A.A. Zakharov, U. Starke, quasi-free-standing epitaxial graphene on SiC obtained by hydrogen intercalation, *Phys. Rev. Lett.*, **103**, (2009) 246804.
- [61] F. Speck, J. Jobst, F. Fromm, M. Ostler, D. Waldmann, M. Hundhausen, H.B. Weber, T. Seyller, the quasi-free-standing nature of graphene on H-saturated SiC (0001), *Appl. Phys. Lett.*, **99** (2011) 122106.
- [62] S. Forti, K.V. Emtsev, C. Coletti, A.A. Zakharov, C. Riedl, U. Starke, large-area homogeneous quasi-free standing epitaxial graphene on SiC (0001): electronic and structural characterization, *Phys. Rev. B*, **84** (2011) 125449.
- [63] S. Oida, F. R. Mcfeely, J.B. Hannon, R.M. Tromp, M. Copel, Z. Chen, Y. Sun, D. B. Farmer, decoupling graphene from SiC (0001) via oxidation *Phys. Rev. B*, **82** (2010) 041411(R).
- [64] M. Ostler, M. Fromm, R.J. Koch, P. Wehrfritz, F. Speck, H. Vita, S. Bottcher, K. Horn, T. Seyller, buffer layer free graphene on SiC (0001) via interface oxidation in water vapor, *Carbon*, **77** (2014) 258-265.
- [65] M.H. Oliveira, T. Schumann, F. Fromm, R. Koch, M. Ostler, T. Seyller, J.M.J. Lopes, H. Riechert, Formation of high-quality quasi-free-standing bilayer graphene on SiC (0001) by oxygen intercalation upon annealing in air, *Carbon*, **52** (2013) 83.
- [66] M.H. Oliveira, J.M.J. Lopes, T. Schumann, L.A. Galves, M. Ramstieiner, K. Berlin, A. Trampert, H. Riechert, synthesis of quasi-free-standing bilayer graphene nanoribbons on SiC surfaces, *Nat. Commun.*, **6** (2015) 7632.
- [67] G. Sclauzero and A. Pasquarello, carbon rehybridization at the graphene/SiC

- (0001) interface: effect on stability and atomic-scale corrugation, *Phys. Rev. B*, **85** (2012) 161405(R).
- [68] W. Strupinski, K. Grodecki, P. Caban, P. Ciepielewski, I. Jozwik-biala, J.M. Baranowski, formation mechanism of graphene buffer layer on SiC (0001) *Carbon*, **81** (2015) 63.
- [69] F. Fromm, M.H. Oliveira, A. Molina-Sanchez, M. Hundhausen, J.M.J. Lopes, H. Riechert, L. Wirtz, T. Seyller, contribution of the buffer layer to the Raman spectrum of epitaxial graphene on SiC (0001), *New J. Phys.*, **15** (2013) 043031.
- [70] X. Wang and H. Dai, etching and narrowing of graphene from the edges, *Nat. Chem.*, **2** (2010) 661.
- [71] J. Bai, X. Duan, Y. Huang, rational fabrication of graphene nanoribbons using a nanowire etch mask, *Nano. Lett.*, **9** (2009) 2083.
- [72] K. Wakabayashi, Y. Takane, M. Sigrisy, perfectly conducting channel and universality crossover in disordered graphene nanoribbons, *Phys. Rev. Lett.*, **99** (2007) 036601.
- [73] K. Todd, H. T. Chou, S. Amasha, D. Goldhaber-Gordon, quantum dot behavior in graphene nanoconstrictions, *Nano. Lett.* **9** (2009) 416-421.,
- [74] M. Sprinkle, M. Ruan, Y. Hu, J. Hankinson, M. Rubio-Roy, B. Zhang, X. Wu, C. Berger, W. A. de Heer, scalable templated growth of graphene nanoribbons on SiC, *Nat. Nanotechnol.*, **5** (2010) 727.
- [75] I. Palacio, A. Celis, M. N. Nair, A. Gloter, A. Zobelli, M. Sicot, D. Malterre, M. S. Nevius, et al., atomic structure of epitaxial graphene sidewall nanoribbons: flat graphene, miniribbons, and the confinement gap, *Nano. Lett.*, **15** (2014) 182.
- [76] J. Baringhaus, M. Ruan, F. Edler, A. Tejada, M. Sicot, A. Ibrahimi, A. Li, Z. Jiang, et al. exceptional ballistic transport in epitaxial graphene nanoribbons, *Nature*, **506** (2014) 394.
- [77] W. Norimatsu, M. Kusunoki, formation process of graphene on SiC (0001), *Physica E*, **42** (2010) 691.

- [78]M. Morita, W. Norimatsu, H. J. Qian, S. Irle, M. Kusunoki, atom-by-atom simulations of graphene growth by decomposition of SiC (0001): impact of the substrate steps, *Appl. Phys. Lett.*, **103** (2013) 141602.
- [79]G. E. Moore, cramming more components onto integrated circuits, *Electronics*, **38** (1965) 114-117.
- [80]M. Mitchel Waldrop, the chips are down for Moore's law, *Nature*, **530** (2016) 144-147.
- [81]H. T. Lue, T. H. Hsu, Y. H. Hsiao, S. P. Hong, M. T. Wu, F. H. Hsu, et al., a highly scalable 8-layer 3D vertical-gate TFT NAND Flash using junction-free buried channel BE-SONOS device, *VLSI Symposia.*, (2010) 131-132.

## **Acknowledgements**

It was my most precious experience to study in Saito Lab, Department of Quantum Engineering, Graduate School of Engineering, Nagoya University. I would like to express the deepest appreciation to Prof. Yahachi Saito for his patient instruction and guidance. I am very grateful to Assistant Prof. Hitoshi Nakahara for the generous support of experiment and discussions. I also would like to thank Lecturer Koji Asaka for many sincere advices. Without their persistent help, this thesis would not have been possible.

I gratefully acknowledge the help of past and present students in Saito Lab. Dr. Akkawat Ruammaitree supported me a lot on the experiments. Mr. Tomohiro Terada was my tutor in the lab, who helped me very much on study and life during my first year in Japan. I also want to thank Mr. Keita Yamaguchi, Mr. Kenichi Ootsuka, Mr. Masashi Horibe, who used to work with me and brought me many good times in the lab.

I would like to express my gratitude to Prof. Toru Ujihara and Mr. Takuya Muto, Center for Integrated Research of Future Electronics, Institute of Materials and Systems for Sustainability, Nagoya University, for their support and work about graphene formation on step-free SiC substrates in this thesis. I also would to thank Prof. Kazuo Soda, Department of Quantum Engineering, Graduate School of Engineering, Nagoya University, for his kind advices.

Finally, I would like to offer my special thanks to my parents and my wife for the support and encouragement, which help me through every difficult time.